Department of
Industry and Resources

RECORD
2007/10

NEOPROTEROZOIC REWORKING IN THE PALEOPROTEROZOIC CAPRICORN OROGEN: EVIDENCE FROM $^{40}Ar/^{39}Ar$ AGES

by S. A. Occhipinti

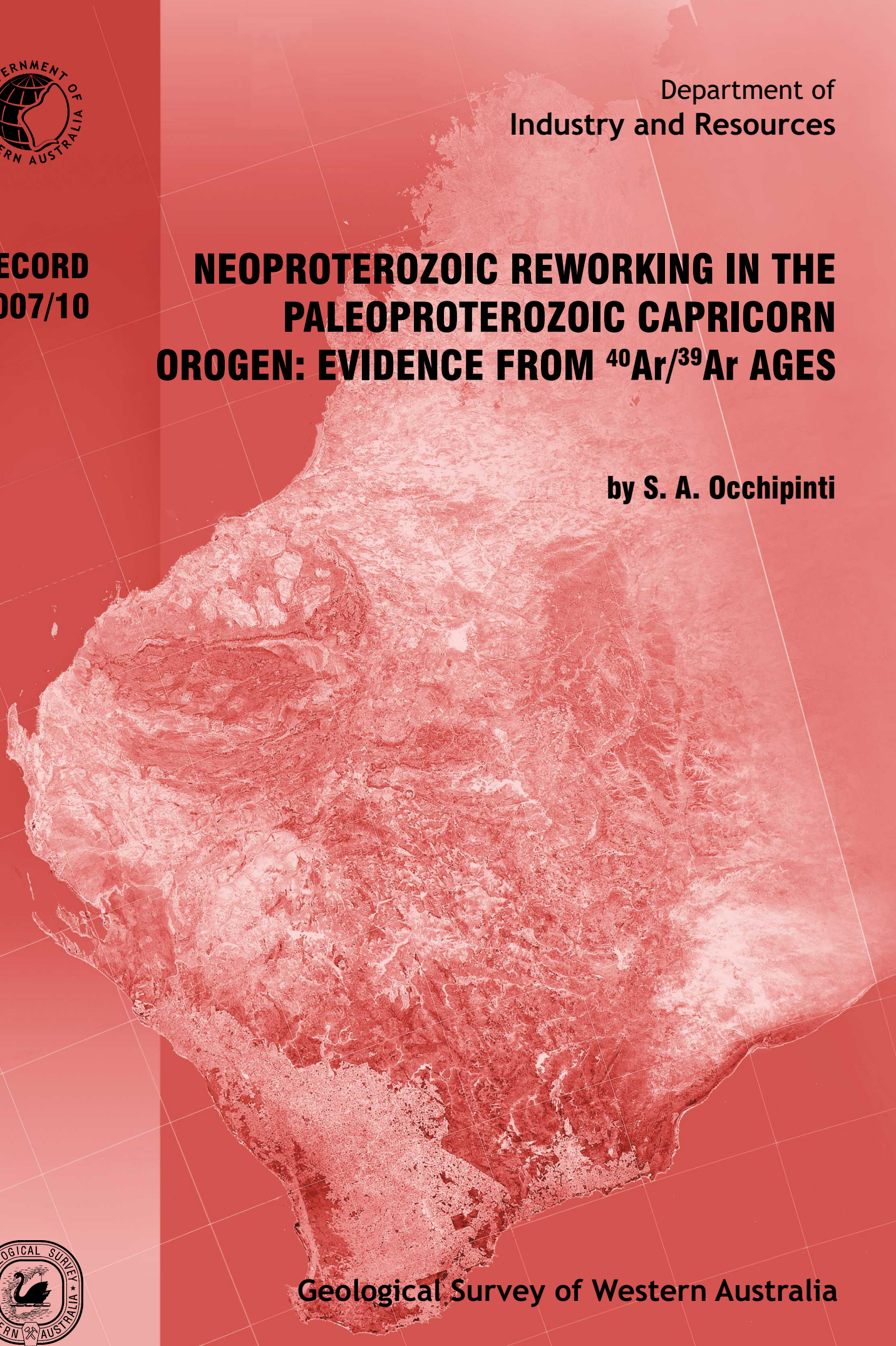

Geological Survey of Western Australia

GEOLOGICAL SURVEY OF WESTERN AUSTRALIA

Record 2007/10

NEOPROTEROZOIC REWORKING IN THE PALEOPROTEROZOIC CAPRICORN OROGEN: EVIDENCE FROM $^{40}Ar/^{39}Ar$ AGES

by
S. A. Occhipinti[1]

[1] Current address: Fugro Airborne Surveys Pty Ltd, 65 Brockway Road, Floreat, W.A. 6014

Perth 2007

REFERENCE
The recommended reference for this publication is:
OCCHIPINTI, S. A., 2007, Neoproterozoic reworking in the Paleoproterozoic Capricorn Orogen: evidence from $^{40}Ar/^{39}Ar$ ages: Western Australia Geological Survey, Record 2007/10, 41p.

National Library of Australia Card Number and ISBN 978-1-74168-115-4

Grid references in this publication refer to the Geocentric Datum of Australia 1994 (GDA94). Locations mentioned in the text are referenced using Map Grid Australia (MGA) coordinates, Zone 50. All locations are quoted to at least the nearest 100 m.

Cover image modified from Landsat data, courtesy of ACRES

Published 2007 by Geological Survey of Western Australia
This Record is published in digital format (PDF) and is available online at www.doir.wa.gov.au/GSWA/publications.
Laser-printed copies can be ordered from the Information Centre for the cost of printing and binding.

Further details of geological publications and maps produced by the Geological Survey of Western Australia are available from:
Information Centre
Department of Industry and Resources
100 Plain Street
EAST PERTH, WESTERN AUSTRALIA 6004
Telephone: +61 8 9222 3459 Facsimile: +61 8 9222 3444
www.doir.wa.gov.au/GSWA/publications

Contents

Appendices

Figures

Tables

Neoproterozoic reworking in the Paleoproterozoic Capricorn Orogen: evidence from $^{40}Ar/^{39}Ar$ ages

by

S. A. Occhipinti[1]

Abstract

An $^{40}Ar/^{39}Ar$ mica thermochronology study in the southern Capricorn Orogen of Western Australia confirms that the region has a complex and prolonged geological history between the Paleoproterozoic and Neoproterozoic, and indicates that a regionally extensive exhumation event took place between 960 and 820 Ma. The 960–820 Ma thermal event was associated with the Edmundian and Pinjarra Orogenies and was likely the result of the collision of a continent with southwestern Australia during assembly of the Rodinian supercontinent. Exhumation of the southern Capricorn Orogen resulted in the initial formation of early Neoproterozoic basins, including at least the lowermost part of the Officer Basin (Centralian Superbasin). Three analytical methods were used: infrared laser single- and multiple-grain fusion, infrared laser step-heating of single and multiple grains, and ultraviolet laser spots and traverses within single grains. The results show that these three analytical methods are complementary and can be readily integrated to provide meaningful and interpretable results.

KEYWORDS: geochronology, $^{40}Ar/^{39}Ar$, Neoproterozoic, Capricorn Orogen, Gascoyne Complex, Edmundian Orogeny, Pinjarra Orogeny

Introduction

In this study, rocks from the southwestern Capricorn Orogen in Western Australia were analysed using the $^{40}Ar/^{39}Ar$ dating technique on muscovite and biotite, in an attempt to constrain the lower greenschist facies history, and therefore part of the exhumation history of the region. Regional and detailed studies of the Capricorn Orogen have previously been undertaken and the deformation and metamorphic history is well known (Occhipinti et al., 2001). In addition, the timing of deformation events that took place under high-grade metamorphic conditions (amphibolite to granulite facies) have been determined from both direct U–Pb zircon dating of metamorphic rocks using the sensitive high-resolution ion microprobe (SHRIMP) (Occhipinti and Reddy, 2004; Occhipinti et al., 2004), and indirect U–Pb SHRIMP dating where igneous crystallization ages of cross-cutting granites bracketed the ages of deformation events (Occhipinti et al., 2001; Sheppard et al., 2004). The timing of lower grade (greenschist facies) deformation events in some parts of the region has also been previously determined using igneous cross-cutting relationships (Occhipinti et al., 1998, 2001, 2003).

This study follows on from regional and detailed geological studies of the southwestern Capricorn Orogen, which showed that all rocks in the region have been metamorphosed to greenschist or sub-greenschist facies (Culver, 2001; Occhipinti and Reddy, 2004; Occhipinti and Sheppard, 2001; Occhipinti et al., 2004; Reddy and Occhipinti, 2004; Sheppard and Occhipinti, 2000; Varvell, 2001). In addition, micas are commonly the foliation-forming minerals and therefore can be related to the structural history. The pervasive greenschist facies metamorphic event has commonly been attributed to the Capricorn Orogeny, but has not been adequately dated (Occhipinti et al., 1998; Occhipinti and Sheppard, 2001; Varvell, 2001; Occhipinti et al., 2003; Occhipinti and Reddy, 2004; Reddy and Occhipinti, 2004). To determine absolute ages for the greenschist or sub-greenschist facies mineral assemblages in rocks throughout the southern Capricorn Orogen, this study applied the $^{40}Ar/^{39}Ar$ dating technique to 28 samples of muscovite or biotite from the Capricorn Orogen (Fig. 1).

Geological background and geochronological constraints

The Capricorn Orogen (Fig. 1) contains early to late Archean granite and granitic gneiss, Paleoproterozoic metasedimentary and mafic meta-igneous rocks, granite

[1] Current address: Fugro Airborne Surveys Pty Ltd, 65 Brockway Road, Floreat, W.A. 6014

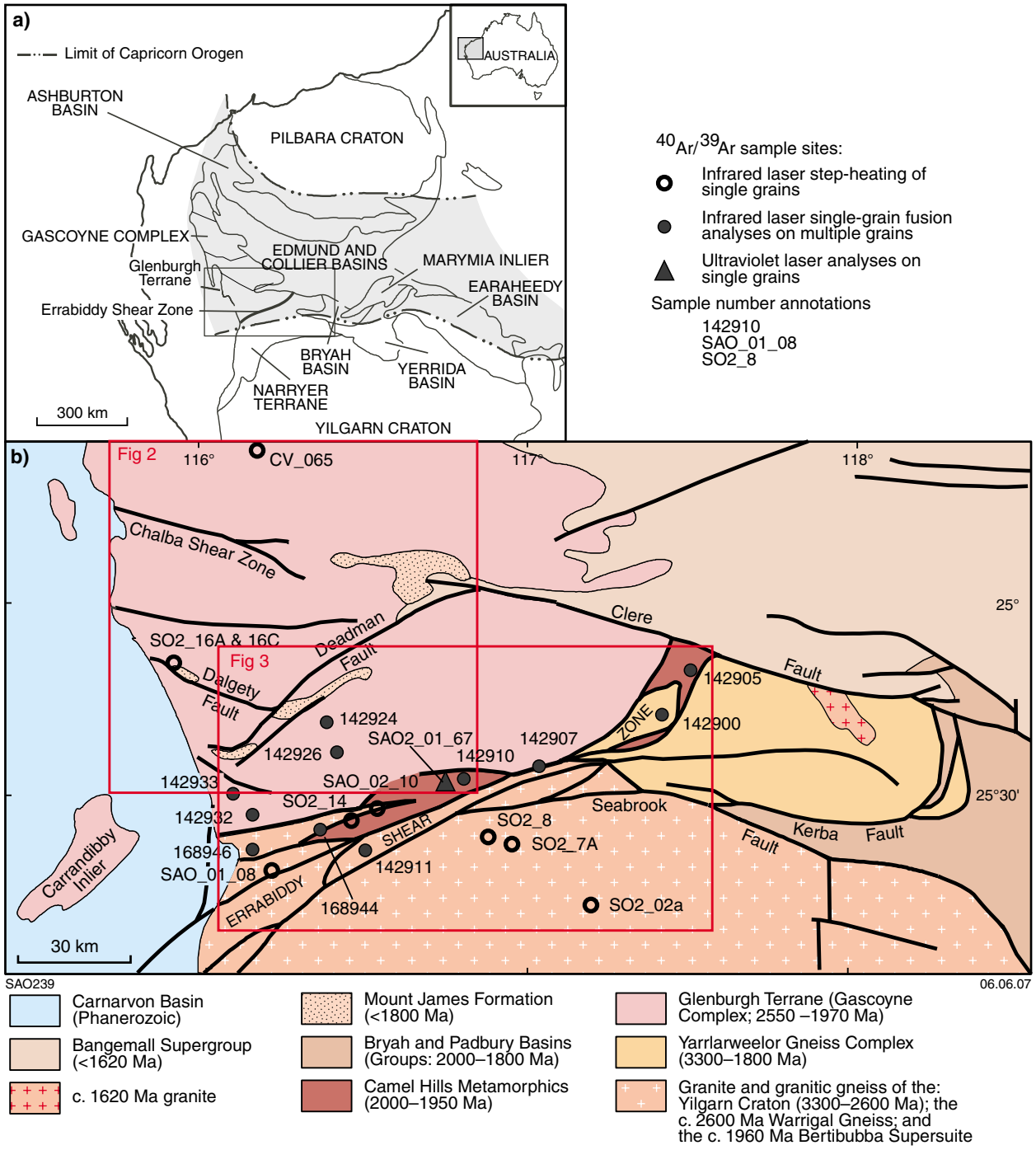

Figure 1. a) Location of the Capricorn Orogen within the West Australian Craton; b) simplified regional geology, sample locations, and sample analysis types

and granitic gneiss, as well as Paleoproterozoic to Mesoproterozoic sedimentary rocks. Rocks of the orogen are overlain unconformably by Neoproterozoic and Permian sedimentary rocks. Different tectonic units in the southwestern part of the Capricorn Orogen include: the Gascoyne Complex, the Errabiddy Shear Zone, the Narryer Terrane and Yarlarweelor Gneiss Complex (Yilgarn Craton), the Bryah and Padbury Basins, the Edmund and Collier Basins (Bangemall Supergroup), and the Carnarvon Basin (Fig. 1).

Paleoproterozoic deformation and metamorphism in the southwestern Capricorn Orogen was heterogeneous and took place during the 2005–1950 Ma Glenburgh Orogeny and 1830–1780 Ma Capricorn Orogeny (Occhipinti et al., 1998; Occhipinti et al., 2004; Sheppard et al., 2004; Sheppard et al., 2005), and possibly during the 1680–1620 Ma Mangaroon Orogeny (Sheppard et al., 2005).

Evidence of post-Paleoproterozoic tectonism in the southern Capricorn Orogen comes not only from the

presence of Mesoproterozoic sedimentary basins, but also from Rb–Sr mineral and whole-rock data from the Gascoyne Complex, which yield Neoproterozoic Rb–Sr biotite ages between 920 and 630 Ma (de Laeter, 1976; Libby et al., 1999). An $^{40}Ar/^{39}Ar$ study on K-feldspars from the Glenburgh Terrane and Errabiddy Shear Zone yielded ages in the range 3060–466 Ma (Weber, 2002). However, these data cannot easily be interpreted when integrated with field mapping data and U–Pb SHRIMP ages from the region. For example, some of the $^{40}Ar/^{39}Ar$ K-feldspar ages calculated for Moorarie Supersuite granites in the Errabiddy Shear Zone and Glenburgh Terrane are older than U–Pb zircon crystallization ages of the granites, indicating the heterogeneous presence of excess ^{40}Ar in K-feldspar. These Rb–Sr or $^{40}Ar/^{39}Ar$ studies (de Laeter, 1976; Libby et al., 1999; Weber, 2002) did not integrate age data with regional or detailed structural or thermal histories; this issue is addressed in this Record.

Yilgarn Craton

At the southern limit of the Capricorn Orogen, the Narryer Terrane is part of the Archean Yilgarn Craton and comprises granitic gneiss interleaved with subordinate metasedimentary and mafic meta-igneous rocks (Nutman et al., 1991; Williams and Myers, 1987). Granitic gneisses from the Narryer Terrane are mostly derived from c. 3700–3300 Ma granites, which are intruded by 2750–2600 Ma granite and minor amounts of gabbro (Kinny et al., 1988; Nutman et al., 1991; summarized in Occhipinti et al., 2001). Metasedimentary rocks with detrital zircons of ages ranging from 4400 to 3100 Ma are tectonically interleaved with mafic and ultramafic rocks, forming discontinuous elongate belts within the largely granitic terrane.

The Yarlarweelor Gneiss Complex (Fig. 1) comprises 3300–2600 Ma granites, granitic gneiss, and supracrustal rocks of the Narryer Terrane (Yilgarn Craton) that were locally deformed and intruded by biotite monzogranite of the 1965–1945 Ma Bertibubba Supersuite, and then metamorphosed, deformed, and intruded by granite between 1820 and 1780 Ma (Occhipinti et al., 1998; Sheppard et al., 2003). The Yarlarweelor Gneiss Complex is tectonically juxtaposed against the greenschist to locally amphibolite facies 2000–1800 Ma sedimentary and mafic igneous rocks of the Bryah and Padbury Basins in the south and east, which were deposited along the northern margin of the Yilgarn Craton at c. 2000 Ma (Occhipinti et al., 2004; Pirajno and Adamides, 2000). Regional and detailed studies found that greenschist facies high-strain zones in the Yarlarweelor Gneiss Complex, and between the Yarlarweelor Gneiss Complex and the Bryah and Padbury basins, contain indications of dextral strike-slip shear (Occhipinti et al., 1998; Reddy and Occhipinti, 2004).

Gascoyne Complex

The Gascoyne Complex (Fig. 1) consists of the Glenburgh Terrane at its southern end, in addition to several east-southeast trending structural and metamorphic zones in the centre and north (Sheppard et al., 2005). The Glenburgh Terrane is unique in the Gascoyne Complex in that it consists of variably metamorphosed and deformed c. 2000 Ma tonalite, trondhjemite, monzogranite, and granodiorite of the Dalgaringa Supersuite, which intruded into a basement of c. 2500 Ma granodiorite, tonalite, and monzogranite (Nelson, 2000; Occhipinti et al., 2001). In parts of the Glenburgh Terrane, the Dalgaringa Supersuite and c. 2500 Ma granites were deformed and metamorphosed to form gneisses that are collectively called the Halfway Gneiss (Occhipinti and Sheppard, 2001; Occhipinti et al., 2004).

Elsewhere in the Glenburgh Terrane, the Dalgaringa Supersuite consists of 2005–1970 Ma granites that have been metamorphosed and heterogeneously deformed such that they only locally form well-banded granitic gneiss. The older parts of the Dalgaringa Supersuite were deformed and metamorphosed to upper amphibolite or granulite facies by c. 1989 Ma, and intruded by mesocratic and leucocratic tonalite at c. 1975 Ma (Occhipinti and Sheppard, 2001; Occhipinti et al., 2004). All these rocks were subsequently metamorphosed and deformed at medium grades. Supracrustal rocks, including mafic schist and gneiss, pelitic schist, calc-silicate gneiss, and dolomitic marble, form distinct bands within the granitic gneiss units and are called the Moogie Metamorphics (Occhipinti and Sheppard, 2001).

The zones that comprise the central and northern parts of the Gascoyne Complex are separated from the Glenburgh Terrane by the Chalba Shear Zone (Fig. 2) and from each other by large-scale faults or shear zones. Granites of the 1830–1780 Ma Moorarie Supersuite intruded all domains in the complex, as well as adjacent tectonic units, and were metamorphosed at high grade within the Yarlarweelor Gneiss Complex (Occhipinti et al., 1998; Sheppard et al., 2003). Elsewhere in the southern Capricorn Orogen, where the Moorarie Supersuite rocks contain metamorphic mineral assemblages, it is apparent that they were metamorphosed to greenschist facies. These granites are heterogeneously deformed, and are locally well foliated or folded. Each domain is characterized by varying degrees of 1680–1620 Ma magmatism, metamorphism, and deformation (Sheppard et al., 2005).

Most of the northern and central part of the Gascoyne Complex was deformed and metamorphosed at medium to high grade during the Mangaroon Orogeny, and intruded by granites until at least c. 1630 Ma. This orogenic event may have also affected parts of the Capricorn Orogen farther south, as indicated by the presence of three volumetrically significant granites that range in age from c. 1645 to 1620 Ma (Sheppard and Swager, 1999; Nelson, 2002; Sheppard et al., 2005). However, the extent and effect of this event, south of the central Gascoyne Complex, are not completely understood.

Errabiddy Shear Zone

The Errabiddy Shear Zone separates the Yilgarn Craton from the Gascoyne Complex (Fig. 1) and contains tectonic slices of both the Narryer Terrane and Yarlarweelor Gneiss Complex of the Yilgarn Craton. The shear zone initially formed between 2000 and 1950 Ma, when the Glenburgh Terrane accreted onto the Yilgarn Craton (Occhipinti and Reddy, 2004; Occhipinti et al., 2004). The Errabiddy

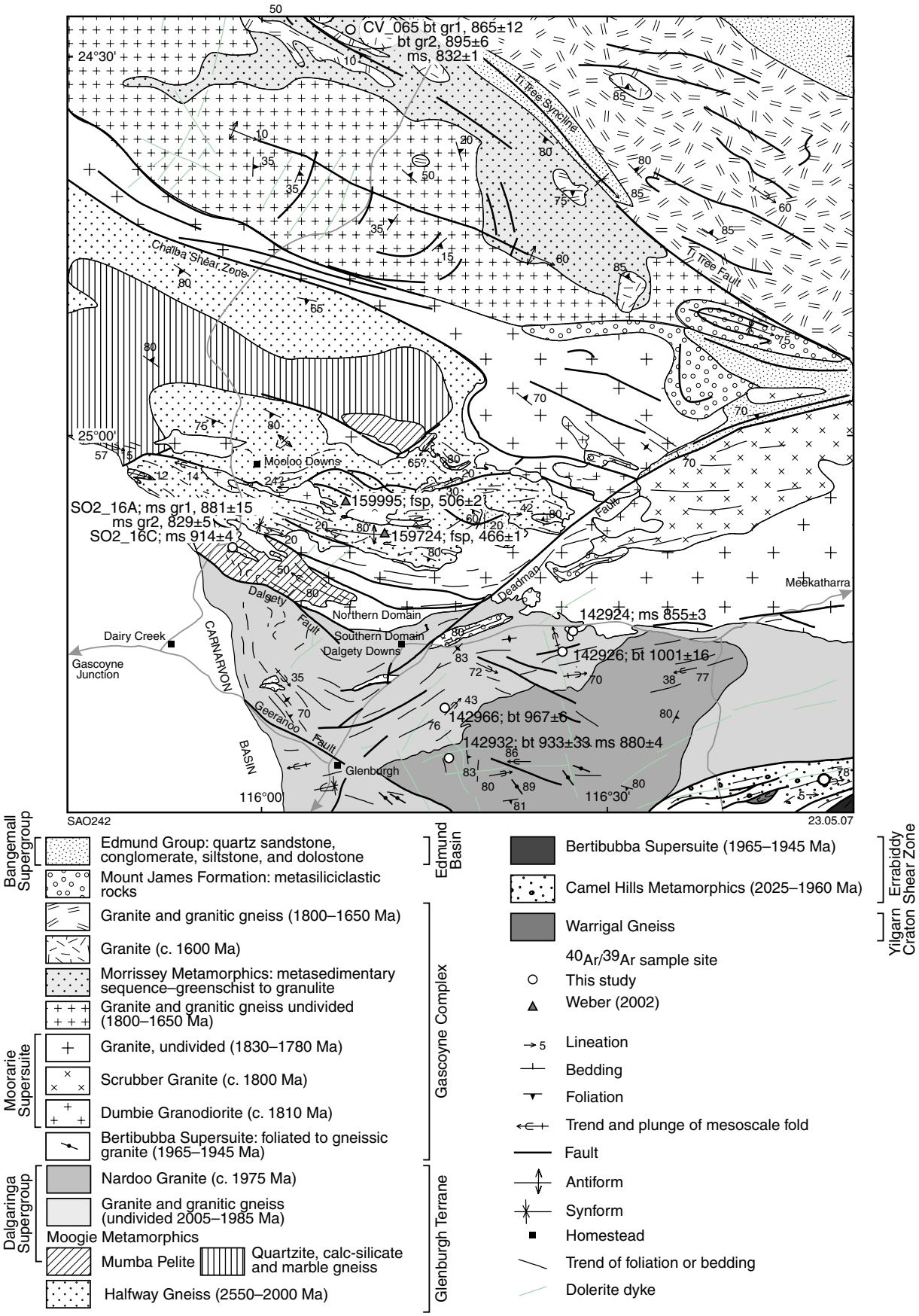

Figure 2. Simplified geology of the Glenburgh Terrane and part of the Errabiddy Shear Zone showing the distribution of $^{40}Ar/^{39}Ar$ ages. Feldspar ages are from Weber (2002). All other data are from this study. fsp = feldspar, ms = muscovite, bt = biotite, gr = grain

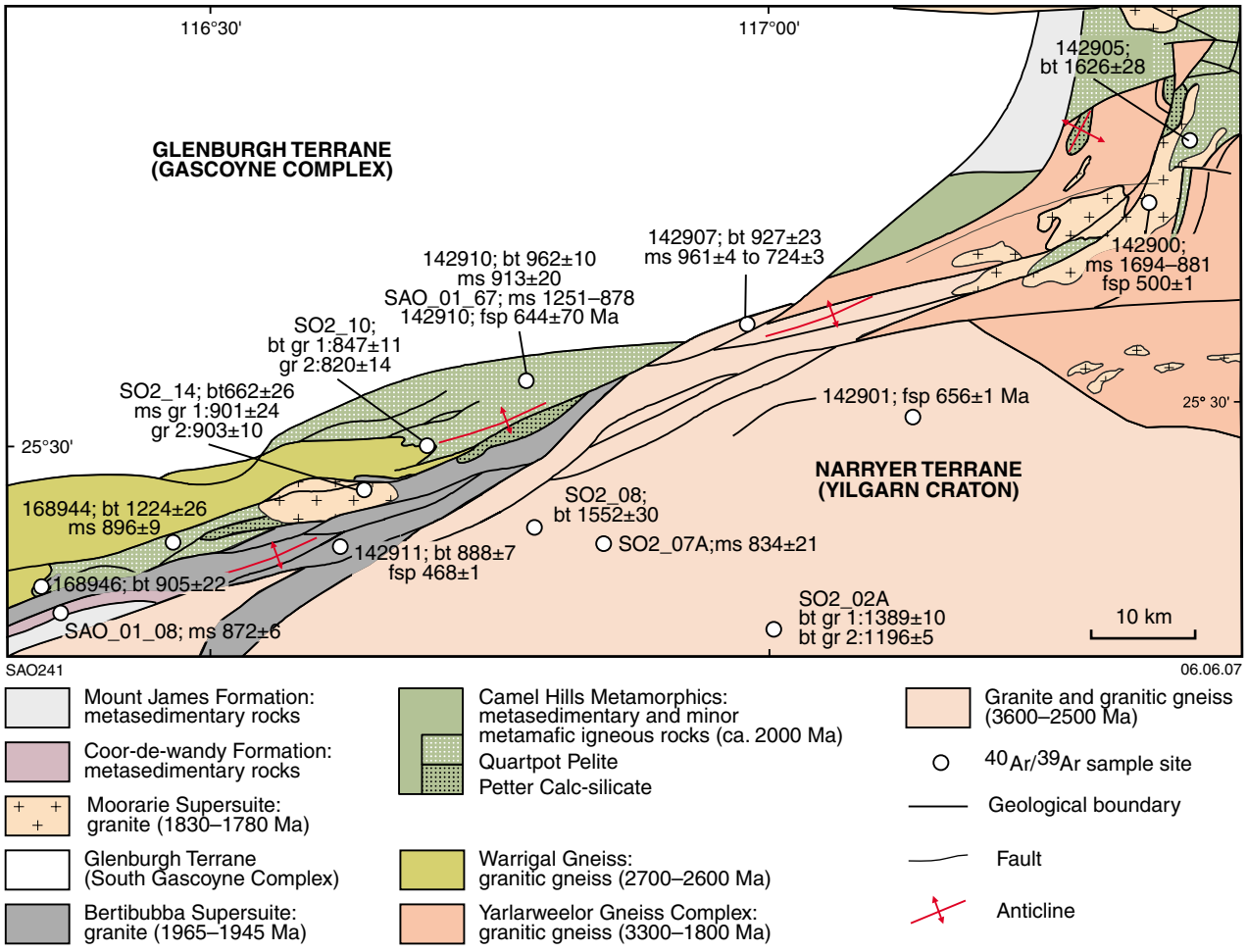

Figure 3. Simplified geology of the Errabiddy Shear Zone and the northwestern Yilgarn Craton (southern Capricorn Orogen) showing the distribution of $^{40}Ar/^{39}Ar$ ages. Feldspar ages are from Weber (2002). All other data are from this study. fsp = feldspar, ms = muscovite, bt = biotite, gr = grain

Shear Zone also contains the Camel Hills Metamorphics and the Warrigal Gneiss, which are confined to the shear zone (Fig. 3). Well-foliated granite and pegmatite-banded granitic gneiss of the Warrigal Gneiss are fault bounded, and the protoliths have been dated at 2700–2600 Ma (Nelson et al., 2000; Occhipinti et al., 2001), which is similar to the age of the late Archean granites of the Narryer Terrane (Yilgarn Craton). The Camel Hills Metamorphics consist of pelitic schists and gneisses, and calc-silicate gneiss.

SHRIMP U–Pb zircon ages of c. 1950 Ma (Occhipinti et al., 2004) from the migmatized pelitic schists of the Camel Hills Metamorphics are interpreted to represent the time of upper amphibolite to granulite facies metamorphism and migmatization of the pelites (Occhipinti et al., 2004), which is inferred to be the time of peak metamorphism associated with a major foliation-forming event in the shear zone (Occhipinti and Reddy, 2004). Pervasive easterly to northerly trending folds and shear zones that developed during greenschist facies metamorphism have deformed the medium- to high-grade foliation (Occhipinti and Reddy, 2004). This event was associated with simple shear and dextral strike-slip movement at, and close to, shear zone boundaries, whereas pure shear (coaxial) took place within the shear zone. This suggests that the deformation and accompanying metamorphism were the result of dextral transpression (Occhipinti and Reddy, 2004).

Paleoproterozoic to Mesoproterozoic sedimentary rocks

Paleoproterozoic to Mesoproterozoic sedimentary rocks outcrop in the southwestern Capricorn Orogen. The precise ages of these units are unknown; however, their relative ages are inferred from observed unconformities between them. These sedimentary units include, from oldest to youngest, the Coor-de-wandy and Mount James Formations, and the Edmund and Collier Groups (Bangemall Supergroup). The Coor-de-wandy Formation is only present in fault-bounded lenses of the Errabiddy Shear Zone, and includes low-grade micaceous schist. The low metamorphic grade and simple deformation history of the formation (Drew, 1999a,b) indicates that these metasedimentary rocks are significantly younger than the Camel Hills Metamorphics and the other

rocks that form part of the Errabiddy Shear Zone. The Coor-de-wandy Formation is unconformably overlain by low-grade siliciclastic rocks of the Mount James Formation in the Errabiddy Shear Zone (Drew, 1999a,b; Williams et al., 1983). The Mount James Formation also commonly outcrops as discrete fault-bounded lenses throughout the Glenburgh Terrane. In the central part of the Glenburgh Terrane, the Mount James Formation unconformably overlies the Moogie Metamorphics, and is unconformably overlain by the Mesoproterozoic Edmund Group (Bangemall Supergroup).

Scattered outcrops of the basal siliciclastic and carbonate units of the Edmund Group either unconformably overlie, or are faulted against, older units in the Capricorn Orogen. In the central and eastern parts of the Capricorn Orogen, siliciclastic rocks of the Collier Group unconformably overly the Edmund Group and older rocks. Baddeleyite and zircon from dolerite sills that intrude the Edmund Group yielded U–Pb SHRIMP ages of 1465 ± 3 Ma and 1070 ± 6 Ma (Nelson, 2002; Wingate, 2002; Wingate et al., 2004). The c. 1465 Ma and c. 1070 Ma sills are indistinguishable in the field. However, the c. 1070 Ma sills also intrude the Collier Group, which does not contain the c. 1465 Ma sills (Wingate, 2002; Wingate et al., 2004). Extensional faults related to sedimentation in the Edmund and Collier Basins have not been unequivocally identified in the basement rocks in the region (e.g. Gascoyne Complex and Yilgarn Craton).

The dolerite sills that intruded both the Edmund and Collier Groups were deformed and metamorphosed along with the sediments and the underlying basement at low metamorphic grades during the Edmundian Orogeny, before being cut by northerly trending dolerite dykes of the 755 Ma Mundine Well Dolerite Suite (Wingate and Giddings, 2000; Martin and Thorne, 2004).

Sample descriptions

A summary of the samples used in this study, describing sample localities and petrography, and providing U–Pb SHRIMP zircon ages (where available) is given in Appendix 1. The following sample descriptions include some inferred metamorphic grades. However, accurate determination of metamorphic temperature and pressure conditions is problematic because many of the rocks are either granitic or have been affected by pervasive retrogression of prograde metamorphic assemblages. Despite this, all samples included minerals that crystallized during the final stage of metamorphism and are indicative of greenschist facies metamorphism. This greenschist component affected all rocks, regardless of their prograde metamorphic mineral assemblages (Occhipinti and Reddy, 2004; Occhipinti et al., 2004).

Narryer Terrane (Yilgarn Craton)

Three samples were collected from the Narryer Terrane. A granitic gneiss sample (SO2_7a) consists largely of quartz, feldspar, biotite, and muscovite. Quartz and feldspar domains define a gneissosity, and the rarer biotite and muscovite are roughly aligned parallel to the fabric. A sample of a lens of pelitic schist (SO2_8) that outcrops within granitic gneiss of the Narryer Terrane contains one foliation that consists of biotite with minor amounts of feldspar and quartz. Biotite wraps around porphyroblasts interpreted to be andalusite pseudomorphed by very fine-grained mats of sericite and quartz (Fig. 4a). If the andalusite crystallized in the amphibolite facies, then the biotite foliation may have formed in either the amphibolite or greenschist facies (i.e. on the prograde or retrograde path), given that the andalusite porphyroblasts are relatively undeformed but are wrapped by the biotite foliation. Sample SO2_2a is from an even-grained, undeformed biotite granite that intruded surrounding Archean granitic gneiss, and consists mainly of quartz, feldspar, muscovite, and biotite.

Foliations in samples SO2_7a and SO2_8 are thought to have formed during an Archean deformation and high-grade metamorphic event (Occhipinti et al., 2001), on the basis of regional structural and metamorphic correlations, and the presence of unfoliated c. 2600 Ma granite sheets and plutons that cut these fabrics in the region. However, the retrograde unfoliated sericite present in sample SO2_8 might have formed at any time after this Archean deformation and metamorphic event.

Errabiddy Shear Zone

A granitic gneiss sample (SO2_10) from the Warrigal Gneiss consists of feldspar and quartz, with subordinate biotite, garnet, epidote, and sericite. The rock has a gneissosity largely defined by alternating bands of randomly orientated biotite and recrystallized quartz ribbons. Mainly on the basis of regional structural and geochronological correlations, this foliation is believed to have formed during the c. 2005–1950 Ma Glenburgh Orogeny (Occhipinti and Reddy, 2004; Occhipinti et al., 2004). However, the presence of randomly orientated biotite clusters suggests that the biotite may have crystallized or recrystallized after the foliation-forming event.

Metasedimentary rocks from the Camel Hills Metamorphics include diatexite melt from migmatized pelite (GSWA samples 142905 and 142910), and psammite (GSWA 168944). The diatexite melt consists of quartz, plagioclase, K-feldspar, biotite, muscovite, sericite, sillimanite, garnet, and chlorite. A weak gneissosity in sample 142905 is defined by the alignment of biotite and flattened garnet. In sample 142910, a more pervasive foliation of the same generation is largely defined by the alignment of sillimanite (pseudomorphed by randomly oriented sericite) and biotite (Fig. 4b). The presence of prograde biotite, K-feldspar, plagioclase, sillimanite, garnet, and quartz in samples 142905 and 142910 is indicative of upper amphibolite to granulite facies metamorphism concomitant with the main Glenburgh Orogeny foliation-forming event (Sheppard and Occhipinti, 2000; Occhipinti and Reddy, 2004; Occhipinti et al., 2004). Conversely, the mats of unfoliated sericite and muscovite are interpreted to have formed during a

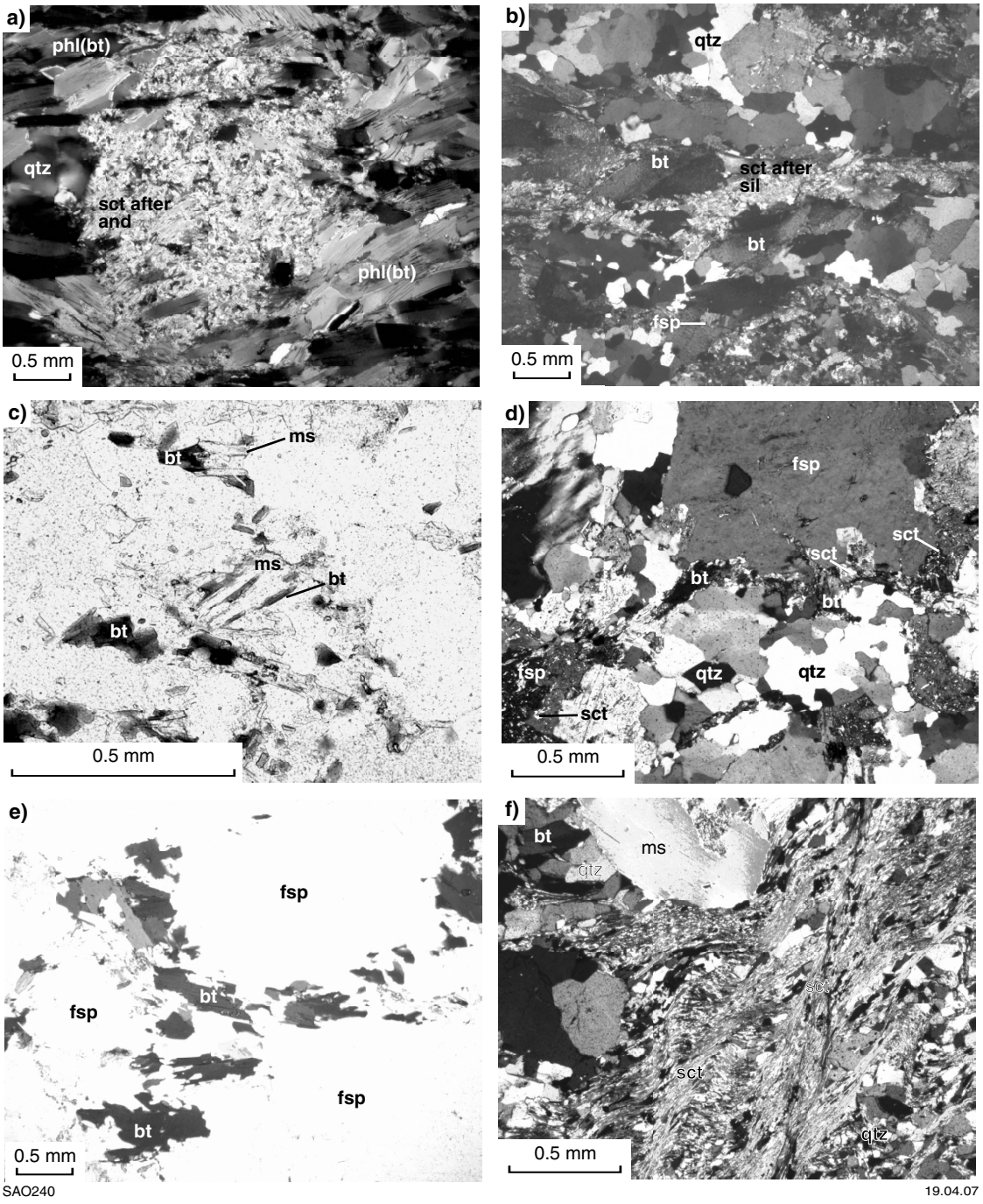

Figure 4. Photomicrographs of six samples used in this study showing the textural relationships of muscovite, sericite, and biotite to other minerals in the rocks, and tectonic foliations. a) Sample SO2_8, cross-polarized light; b) Sample 142910, cross-polarized light; c) Sample 168944, plane-polarized light; d) Sample 142900, cross-polarized light; e) Sample 142932, plane-polarized light; f) Sample SO2_16C, cross-polarized light. qtz = quartz, fsp = feldspar, bt = biotite, phl = phlogopite, sct = sericite, ms = muscovite, and = andalusite, sil = sillimanite

retrograde greenschist-facies metamorphic event related to the Capricorn Orogeny. The psammite sample (168944; Fig. 4c) shows a gneissosity consisting mainly of quartz, plagioclase, biotite, muscovite, and with minor amounts of myrmekite and epidote. The gneissosity is defined by modal variations of biotite and muscovite. Muscovite locally replaces biotite. Regional correlations with nearby pelitic assemblages suggest that this foliation developed in the amphibolite facies (Occhipinti and Reddy, 2004; Occhipinti et al., 2004).

Samples 142911 and 168946, which are from granites of the 1965–1945 Ma Bertibubba Supersuite (Occhipinti et al., 2004), contain biotite, muscovite, sericite, and minor amounts of epidote. The foliation in these rocks is defined by roughly aligned biotite. Metamorphic grade is

difficult to ascertain because of the granitic assemblage. The granites were intruded into the Errabiddy Shear Zone during the Glenburgh Orogeny, and their foliation might have formed either at this time (Occhipinti et al., 2004; Occhipinti and Reddy, 2004), or later during the Capricorn Orogeny. Randomly oriented greenschist-facies minerals, including sericite or muscovite and epidote, locally replace plagioclase feldspar. Muscovite is interpreted to have crystallized during a retrograde metamorphic event that post-dated deformation.

Two samples of granite (GSWA 142900 and SO2_14) and one of pegmatite (SAO_01_67), which are from the Moorarie Supersuite (Sheppard and Occhipinti, 2000; Occhipinti and Reddy, 2004), were collected from the Errabiddy Shear Zone. Sample 142900 is unfoliated granite containing variable amounts of feldspar, quartz, biotite, muscovite, sericite, chlorite, and minor amounts of garnet and epidote (Fig. 4d). Most of the minerals in the granite samples appear to be of primary igneous composition, although sericite partially replaces feldspar and biotite, and chlorite replaces garnet and biotite. A sample from the Erong Granite (SO2_14) contains an unfoliated mineral assemblage of plagioclase, quartz, and K-feldspar, with minor amounts of biotite, muscovite, and epidote. Rare aggregates of fine-grained garnet were observed in hand specimens, but were not present in thin section. Sample SAO_01_67 was taken from an unfoliated muscovite pegmatite that cuts all structural fabrics present in the pelites of the Camel Hills Metamorphics, near the sample 142910 location. The pegmatite is quartz rich (>60% quartz) and also contains feldspar and distinctive books of muscovite.

Sample SAO_08 was taken from the sandy matrix of a poorly sorted, metamorphosed conglomeratic sandstone of the Coor-de-wandy Formation. The matrix contains an undifferentiated foliation defined by aligned muscovite and quartz (Drew, 1999a,b) and may have formed in the greenschist facies, though the exact pressure and temperature conditions could not be derived from the mineral assemblage.

Gascoyne Complex

GSWA samples 142926, 142932, and 142933 are from granites of the 2005–1970 Ma Dalgaringa Supersuite (Sheppard et al., 2004). Samples 142926 and 142932 contain variable amounts of feldspar (locally sericitized), quartz, biotite, and minor amounts of epidote and sericite (Fig. 4e). Sample 142926 is a fine- to medium-grained, foliated biotite tonalite, which was metamorphosed to amphibolite facies during the Glenburgh Orogeny (Occhipinti and Sheppard, 2001; Occhipinti et al., 2001). The foliation is defined by the rough alignment of biotite. Sample 142932 also contains some muscovite. The foliation in sample 142932 is largely defined by aligned biotite, which forms discontinuous clumps throughout the rock (Occhipinti et al., 2004). This foliation is interpreted to have formed in the epidote-amphibolite zone (transitional between amphibolite and greenschist facies) because of the presence of oligoclase–andesine, epidote, and biotite in apparent equilibrium (Miyashiro, 1994; Occhipinti et al., 2004). Subordinate muscovite and sericite are also locally aligned in the foliation. Sample 142933 is a granulite facies metadiorite (Occhipinti et al., 2004) containing plagioclase, clinopyroxene, biotite, and orthopyroxene. Coarse biotite grains are randomly orientated throughout the rock, whereas finer grained biotite is aligned in a weak foliation not defined by any other minerals.

A granite sample (GSWA 142924) from the Moorarie Supersuite (Occhipinti et al., 1998; Sheppard and Occhipinti, 2000; Sheppard et al., 2003) of the Gascoyne Complex contains muscovite and biotite, which are randomly orientated throughout the rock, and fine-grained sericite that locally replaces feldspar. This granite appears massive and undeformed in hand specimen, but elongate quartz domains define a foliation in thin section.

Two samples (SO2_16A and SO2_16C) were collected from low-grade metaconglomerate of the Mount James Formation (Fig. 4f). The metaconglomerate contains deformed quartz clasts in a matrix of metasandstone consisting of quartz, sericite, and muscovite. Sericite or fine-grained muscovite defines a foliation that is approximately parallel to bedding. These grains are crenulated and a crenulation cleavage is well developed in some parts of the rock. Coarser grained muscovite is not aligned in any fabric, but appears to be deformed and may be of detrital origin.

Sample CV_065 was collected from metasedimentary rocks of the Morrissey Metamorphics, and is a quartz–biotite–muscovite–feldspar schist. Quartz is strongly recrystallized to strain-free polygonal grains, and aligned biotite grains define a pervasive foliation. Muscovite is locally aligned in, and pre-dates, the foliation.

$^{40}Ar/^{39}Ar$ dating

Sample preparation

All analyses presented here were of muscovite or biotite grains. Most analyses were undertaken with the high-resolution infrared (IR) laser probe either by single- or multiple-grain total fusion (on small grains, usually <500 μm), or by step-heating of single or multiple grains. One sample of muscovite (SAO_01_67) was analysed by high-resolution ultraviolet (UV) laser probe of spots and traverses.

Details of sample preparation and analytical procedure are presented in Appendix 2. For single-grain fusion IR laser-probe analyses, samples were crushed, the light fractions were extracted, and inclusion-free micas were chosen for analysis. Samples for step-heating analysis were carefully crushed with a hammer, or picked directly from fractured rock particles. All samples were first cleaned in methanol, then in de-ionized water in an ultrasonic bath. Once dry, each sample was packed in aluminium foil and loaded into an aluminium package with other samples. The package was then Cd-shielded and irradiated in the H5 position of the McMaster University Reactor (Hamilton, Canada) for 90 hours, together with biotite age standard

Tinto B (K–Ar age of 409.25 ± 0.71 Ma; Rex and Guise (1995)) placed at 5 mm intervals throughout the aluminium package to monitor the neutron flux gradient. Extraction of argon following irradiation from selected spots and traverses on each sample was done using a CW–Nd–YAG laser, fired through a Merchantek computer-controlled X–Y–Z sample chamber stage and microscope system.

The high spatial resolution of the UV-laser probe allowed analyses of spots and traverses within four muscovite grains from sample SAO_01_67. The spots are between 30 and 90 µm diameter, and include small damage haloes (Kelley, 1995). Care was taken to ensure spots did not overlap so that pits that had been previously de-gassed were not re-analysed.

Technical background

Interpretation of $^{40}Ar/^{39}Ar$ data is complex, owing to a number of problems that may arise when studying minerals in metamorphic rocks. These include within-grain variations of $^{40}Ar/^{39}Ar$ ages due to volume diffusion through the mineral lattice, along grain boundaries, or at microstructural sites such as kinks or fractures. Further complexities can arise either with the presence of excess ^{40}Ar, or the loss of radiogenic ^{40}Ar from a sample if the grains are heated to temperatures near the closure temperature of radiogenic ^{40}Ar, allowing diffusion of argon into and out of the grains.

The effective grain size or domain size of minerals analysed can affect their $^{40}Ar/^{39}Ar$ ages. For example, bell-shaped age profiles within undeformed grains that contain younger $^{40}Ar/^{39}Ar$ ages close to grain boundaries, or at microstructurally favourable sites, may reflect lattice-dominated volume diffusion, or diffusion along fast-diffusion pathways, respectively (Kelley and Turner, 1991). In the former case, the effective grain size of a mineral is its true grain size, but if there is microstructure, such as kinks or fractures, the effective grain size is the size of the domain formed by the presence of the microstructures within the mineral (Kelley and Turner, 1991). When grains are crushed in preparation for analysis, the measured grain size might be less than the effective grain size of the mineral.

Excess or 'inherited' ^{40}Ar is defined as parentless radiogenic argon added to a mineral during crystallization of fluid or melt inclusions contained within the mineral, or incorporated into the mineral lattice by subsequent diffusion (McDougall and Harrison, 1999; Kelley, 2002). Determination of the excess ^{40}Ar component within a mineral is sometimes possible by plotting inverse isochron correlation diagrams of $^{36}Ar/^{40}Ar$ (y-axis; parentless radiogenic component) against $^{39}Ar/^{40}Ar$ (x-axis; age) (Roddick et al., 1980; Kelley, 1995). Alternatively, the spatial distribution of apparent ages in grains in which excess argon is heterogeneously distributed can be determined by in situ laser-microprobe analyses (Reddy et al., 1996; Kramer et al., 2001). The amounts of atmospheric argon (^{36}Ar) in all samples analysed in this study are small and do not allow the amount of contaminating non-radiogenic ^{40}Ar to be determined. Therefore, the age data are reported as either an unweighted mean age or the youngest apparent age measured. It is sometimes more appropriate to use the youngest age, especially where there is a large difference between the youngest and oldest ages within a single sample. The youngest age usually correlates with the maximum time of isotopic closure. In both situations the reported age is considered to be the 'best age', but might still contain an excess ^{40}Ar component.

Isotope correlation diagrams for these samples have been analysed and the 'best' age for each sample quoted. The results of IR-laser step-heating analyses are plotted with respect to cumulative $^{39}Ar\%$. The ages (calculated from $^{40}Ar/^{39}Ar$), $^{37}Ar/^{39}Ar$, $^{38}Ar/^{39}Ar$, and $^{36}Ar/^{39}Ar$ are shown for step-heated samples, where $^{37}Ar/^{39}Ar$ and $^{38}Ar/^{39}Ar$ are indicators of Ca/K and Cl/K ratios, respectively (McDougall and Harrison, 1999), whereas ^{36}Ar is the assumed atmospheric component (McDougall and Harrison, 1999).

Results

The results for IR total-fusion and step-heating experiments are summarized in Table 1, where the 'best' apparent ages for the samples analysed are quoted. These apparent $^{40}Ar/^{39}Ar$ ages are also summarized on simplified geological maps (Figs 2 and 3). Data from spots and traverses analysed by high-resolution single-grain UV-laser analyses are presented in Table 2. All other isotopic data are included in supplementary data tables (Appendix 3) and are discussed below. All $^{40}Ar/^{39}Ar$ ages are quoted with 1σ uncertainties.

Results of IR-laser step-heating analyses plotted with respect to cumulative $^{39}Ar\%$ are illustrated in Figures 5–9. The results of $^{40}Ar/^{39}Ar$ dating are first described in terms of their geographical locations in the Narryer Terrane, Errabiddy Shear Zone, and Gascoyne Complex, prior to integrating the data in the discussion section of this Record.

Narryer Terrane

Samples SO2_2a, SO2_7a, and SO2_8 were analysed using the IR-laser step-heating method. Age and isotopic spectra show significant heterogeneity, both between and within samples (Fig. 5). This heterogeneity precludes the calculation of step-heating plateaus for the age spectra.

Heterogeneity in the age spectra for biotite grains from samples SO2_8 and grains 1 and 2 of SO2_2a qualitatively relate to variations in chlorine, calcium, and atmospheric argon content in the first seven steps of the spectra, where commonly higher and sometimes lower apparent ages qualitatively correspond to higher amounts of chlorine, calcium, and sometimes atmospheric argon in the analyses.

In sample SO2_2a, because of the large difference between apparent biotite $^{40}Ar/^{39}Ar$ ages of 1389 ± 10 Ma for grain 1, and 1196 ± 5 Ma for grain 2, these are considered to be the maximum $^{40}Ar/^{39}Ar$ ages of the biotite grains. The difference in the apparent ages for

Table 1. Summary of $^{40}Ar/^{39}Ar$ results

Area	*Sample name*	*Mineral*	*Analytical method*	*Details*	*% Atmospheric (range)*	*Weighted mean age (Ma)*	*Unweighted mean age (Ma)*	*Plateau ages, unweighted mean ages using select data (Ma)*	*Maximum age (Ma)*	*Minimum age (Ma)*	*Grain size/s (μm)*
Narryer Terrane (Yilgarn Craton)	SO2_2a	B GR1	IRSH	SGA	0 – 1.60	1434 ± 2	1440 ± 38	–	1591 ± 20	**1389 ± 10**	313
		GR2	IRSH	SGA	0 – 1.0	1249 ± 2	1255 ± 44	–	1341 ± 6	**1196 ± 5**	262
	SO2_7a	WM				834 ± 2	834 ± 21	–	874 ± 5	773 ± 15	332
	SO2_08	B	IRSH	MGA (2)	0 – 1.8	1532 ± 2	1536 ± 49	**1552 ± 30 (93.3% ^{39}Ar)**	1604 ± 25	1452 ± 6	578, 260
Errabiddy Shear Zone											
East	142900	WM	IRF		0.03 – 6.53	na	na	–	1694 ± 16	**881 ± 4**	050–200
	142905	B	IRF		0 – 5.01	1623 ± 2	1626 ± 28	–	1690 ± 13	1582 ± 5	050–150
West	142907	B	IRF		1.47 – 14.01	927 ± 1	927 ± 23	–	994 ± 6	893 ± 10	050–125
	142907	WM	IRF		0 – 1.51	826 ± 1	837 ± 70	–	961 ± 4	**724 ± 3**	100–200
	142910	B	IRF		1.78 – 9.11	961 ± 1	962 ± 10	–	984 ± 6	973 ± 5	075–145
	142910	WM	IRF		0 – 5.81	912 ± 1	913 ± 20	–	959 ± 4	888 ± 5	050–200
	142911	B	IRF		0 – 12.22	921 ± 1	921 ± 20	–	964 ± 8	**888 ± 7**	050–115
	168944	B	IRF		1.72 – 7.09	1220 ± 2	1224 ± 26	–	1263 ± 30	1178 ± 5	050–110
	168944	WM	IRF		0 – 2.43	941 ± 2	931 ± 44	–	1021 ± 4	**896 ± 9**	050–200
	168946	B	IRF		2.56 – 10.87	902 ± 2	905 ± 22	–	935 ± 4	877 ± 4	030–150
	SAO_01_67	WM									
	SO2_10	B GR1	IRSH		0 – 40.08	828 ± 2	843 ± 61	**874 ± 11 (65.6% ^{39}Ar)**	882 ± 7	722 ± 4	410
		GR2			2.90 – 23.9	789 ± 1	794 ± 46	**820 ± 14 (52.5% ^{39}Ar)**	701 ± 3	844 ± 4	650
	SO2_14	WM GR1	IRSH	SGA	0 – 13.56	884 ± 2	866 ± 43	**901 ± 24 (91.7%^{39}Ar)**	942 ± 4	801 ± 7	260
		GR2		SGA	0 – 5.92	902 ± 2	896 ± 15	**903 ± 10 (91.59%^{39}Ar)**	915 ± 4	875 ± 13	260
		B	IRSH	SGA	4.67 – 10.924	662 ± 1	662 ± 26	–	696 ± 3	627 ± 3	650
	SAO_01_08	WM	IRSH	SGA	0 – 2.16	873 ± 1	872 ± 6	–	881 ± 5	861 ± 5	740
Gascoyne Complex	142924	WM	IRF		0.09 – 1.70	911 ± 1	914 ± 43	–	999 ± 4	855 ± 3	050–350
	142926	B	IRF		3.56 – 12.04	1001 ± 1	1001 ± 16	–	1032 ± 4	964 ± 4	075–175
	142932	B	IRF		0 – 8.68	936 ± 2	933 ± 33	–	999 ± 6	889 ± 21	100–200
	142932	WM	IRF		0 – 2.61	898 ± 2	906 ± 30	–	963 ± 7	**880 ± 4**	150–200
	142933	B	IRF		0.10 – 4.24	1102 ± 1	1106 ± 105	–	1176 ± 5	**967 ± 6**	60–290
	SO2_16A	WM GR1	IRSH	SGA	0.13 – 13.29	886 ± 2	940 ± 137	**895 ± 7 (98.4% ^{39}Ar)**	1269 ± 16	932 ± 3	480
		GR2			0 – 1.04	950 ± 2	966 ± 93	**925 ± 10 (95.5% ^{39}Ar)**	1174 ± 5	906 ± 4	400
	SO2_16C	WM	IRSH	MGA (2)	0 – 9.05	1045 ± 1	1061 ± 76	–	1182 ± 17	914 ± 4	890
											620
	CV_065	WM	IRSH	SGA	0 – 15.97	834 ± 2	845 ± 85	**832 ± 1** (plateau age)	1071 ± 60	750 ± 8	Not measured
		B GR1	IRSH	SGA	0 – 26.97	836 ± 2	781 ± 140	**865 ± 12 (61.9%^{39}Ar)**	881 ± 4	506 ± 12	Not measured
		GR2	IRSH	SGA	0 – 19.32	852 ± 2	850 ± 87	**895 ± 6 (61.1%^{39}Ar)**	903 ± 4	831 ± 4	Not measured

NOTES: **Bold ages** are those selected as 'best estimates for isotopic closure'. All ages are quoted to within 1σ.

WM white mica (muscovite)
B biotite
IRF infrared fusion
IRSH infrared step heated
SGA single grain analyses
MGA multiple grain analyses (number of grains indicated in parentheses)
na mean ages were not calculated for sample 142900 because the age range was considered too large

Table 2. Summary of UV-laser argon isotope analyses on individual spots from grains 1–4 of sample SAO_01_67

J value	±	*Analysis number*	$^{40}Ar/^{39}Ar$	±	$^{38}Ar/^{39}Ar$	±	$^{37}Ar/^{39}Ar$	±	$^{36}Ar/^{39}Ar$	±	$^{39}Ar^{*}(cm^{3})$	±	*%atm Ar*	*Age (Ma)*	±	$^{40}Ar^{*}/^{39}Ar$	±
0.020804	0.000104	1.1	42.50	0.08	0.01179	0.00036	0.00000	0.00000	0.00000	0.00000	7.36E-12	6.06E-15	0.000	1142.91	5.16	42.50	0.15
		1.2	31.73	0.09	0.01167	0.00048	0.00452	0.04626	0.00000	0.00000	7.92E-12	1.65E-14	0.000	914.55	4.92	31.73	0.15
		1.3	33.99	0.08	0.01323	0.00039	0.05224	0.02210	0.00259	0.00026	1.04E-11	8.24E-15	2.253	947.84	4.41	33.22	0.11
		1.4	47.74	0.09	0.01291	0.00057	0.00000	0.00000	0.00000	0.00000	8.50E-12	5.59E-15	0.000	1244.29	5.15	47.74	0.13
		1.5	34.08	0.11	0.01122	0.00016	0.00000	0.00000	0.00000	0.00000	8.55E-12	1.09E-14	0.000	966.90	4.61	34.08	0.12
		1.6	31.00	0.11	0.01054	0.00016	0.00000	0.00000	0.00000	0.00000	8.31E-12	8.24E-15	0.000	897.94	4.48	31.00	0.12
		1.7	48.10	0.47	0.00956	0.00072	0.00000	0.00000	0.00000	0.00000	1.89E-12	3.03E-15	0.000	1251.06	10.73	48.10	0.52
		1.8	41.40	0.20	0.01197	0.00030	0.00000	0.00000	0.00000	0.00000	4.53E-12	5.59E-15	0.000	1120.77	6.10	41.40	0.22
		1.9	33.47	0.11	0.00970	0.00064	0.06586	0.06502	0.00000	0.00000	4.73E-12	8.24E-15	0.000	953.45	4.76	33.47	0.13
		1.10	41.39	0.12	0.01283	0.00031	0.03509	0.06929	0.00000	0.00000	4.44E-12	8.24E-15	0.000	1120.56	5.18	41.39	0.15
		1.11	46.72	0.14	0.00958	0.00002	0.00000	0.00000	0.00029	0.00029	4.64E-12	8.57E-15	0.185	1223.30	5.47	46.63	0.17
		1.2.1	32.05	0.11	0.01112	0.00003	0.05378	0.03186	0.00000	0.00000	7.25E-12	1.92E-14	0.000	921.65	4.59	32.05	0.13
		1.2.2	30.91	0.02	0.01222	0.00001	0.04464	0.00881	0.00000	0.00000	8.87E-12	5.42E-15	0.000	895.87	3.71	30.91	0.05
		1.3.1	31.83	0.32	0.00910	0.00003	0.00000	0.00000	0.00000	0.00296	9.16E-13	3.03E-15	0.000	916.80	21.35	31.83	0.93
		1.3.2	30.16	0.26	0.00972	0.00003	0.00000	0.00000	0.00000	0.00000	1.14E-12	3.03E-15	0.000	878.55	17.55	30.16	0.75
		1.4.1	31.27	0.02	0.01255	0.00001	0.10931	0.00981	0.00000	0.00000	7.97E-12	5.42E-15	0.000	904.09	3.77	31.27	0.06
		2.1.1	30.98	0.02	0.01305	0.00045	0.15951	0.02625	0.00000	0.00000	5.97E-12	3.03E-15	0.000	897.52	5.82	30.98	0.20
		2.1.2	30.15	0.04	0.01101	0.00020	0.00000	0.00000	0.00000	0.00000	6.69E-12	8.57E-15	0.000	878.34	4.53	30.15	0.13
		3.1.1	35.77	0.02	0.01253	0.00043	0.12511	0.02495	0.00000	0.00000	8.88E-12	3.03E-15	0.000	1003.52	4.84	35.77	0.14
		3.1.2	30.57	0.04	0.01061	0.00029	0.11780	0.01662	0.00000	0.00000	9.43E-12	1.09E-14	0.000	887.97	3.74	30.57	0.06
		3.1.3	31.47	0.07	0.01270	0.00046	0.11458	0.01885	0.00013	0.00016	8.32E-12	1.90E-14	0.126	907.62	4.08	31.43	0.09
		3.1.4	31.48	0.05	0.01195	0.00016	0.16850	0.03697	0.00091	0.00000	8.49E-12	1.41E-14	0.858	902.78	3.76	31.21	0.05
		3.1.5	31.28	0.06	0.01282	0.00015	0.13813	0.01705	0.00055	0.00029	9.21E-12	1.65E-14	0.523	900.44	4.28	31.11	0.10
		4.1.1	32.20	0.09	0.01398	0.00023	0.36692	0.05176	0.00169	0.00000	6.06E-12	1.68E-14	1.555	913.88	4.12	31.70	0.09

NOTE: J value = 0.020804 ± 0.000104 for all analyses

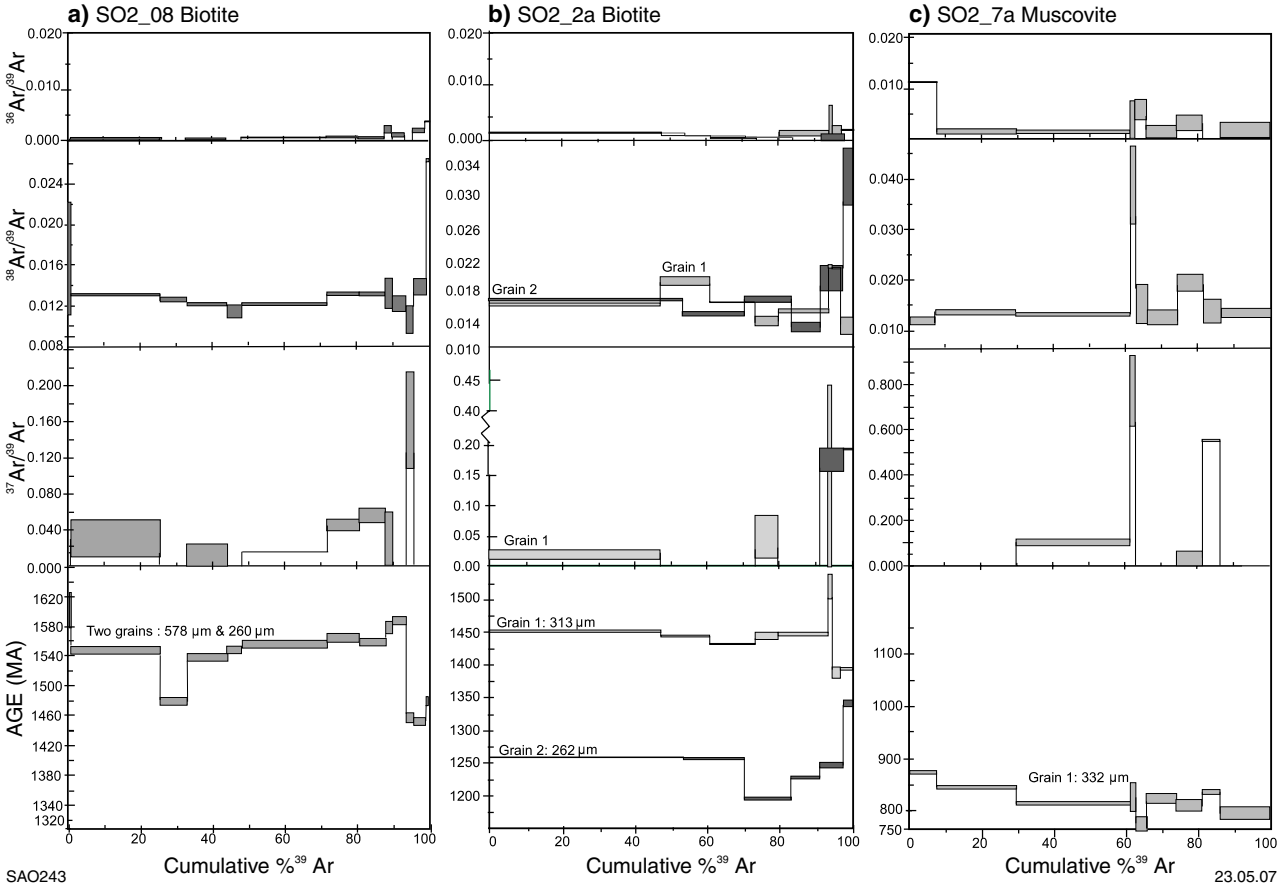

Figure 5. Single- and multiple-grain IR-laser step-heating data for micas from the Narryer Terrane, Yilgarn Craton. Plots of apparent age and isotope variations vs cumulative %^{39}Ar

grains 1 and 2 reflects the difference in grain size, with the smaller biotite grain yielding a younger apparent age. For sample SO2_8, higher amounts of chlorine, calcium, or atmospheric argon in the first and last three steps of the analyses suggest sample contamination. Consequently, the unweighted mean age of the remaining seven steps of the analyses (1552 ± 30 Ma) is taken as the maximum time of ^{40}Ar/^{39}Ar isotopic closure.

Analyses of muscovite grains from sample SO2_7a did not yield a plateau, and variations in apparent ages within the spectra for SO2_7a correspond to complex fluctuations in the amounts of ^{37}Ar and ^{38}Ar. Minor changes in the amount of atmospheric argon during analysis may correspond with variations in the apparent ages. For example, the oldest apparent ^{40}Ar/^{39}Ar age (874 ± 5 Ma) was measured in the first step, which also contained 10% atmospheric argon. Given that the age spectrum for this sample does not show much variance, the 'best' apparent age for this sample is probably the unweighted mean age of 834 ± 21 Ma.

Errabiddy Shear Zone

Fifteen samples of mica were analysed from the Errabiddy Shear Zone (Fig. 3). The eastern and western parts of the Errabiddy Shear Zone are discussed separately.

Eastern part of the Errabiddy Shear Zone

Two samples (142900 and 142905; Figs 3, 10a, and 10b) were analysed from the eastern part of the Errabiddy Shear Zone. Biotite from migmatized pelite of the Camel Hills Metamorphics (142905) gave single-grain total-fusion ages from 1690 to 1582 Ma, with an unweighted mean age of 1626 ± 28 Ma (1σ error; Table 1). The age variation in this sample does not correlate systematically with the grain size of individual micas (Fig. 10a) or any compositional variation within the sample (Table 1; Appendix 3).

Muscovite from granite of the Moorarie Supersuite (sample 142900) yielded ages between 1690 and 881 Ma (Fig. 10b). There is no systematic correlation between grain size and age (Fig. 10b). Given the high variation of apparent ages within the sample, and the possibility of inclusion of excess argon contributing to the older apparent ages, the minimum age of 881 ± 4 Ma represents the maximum age for ^{40}Ar/^{39}Ar closure of the 110 µm grain analysed (Appendix 3, supplementary data table; Table 1).

Western part of the Errabiddy Shear Zone

Nine samples were analysed from the western part of the Errabiddy Shear Zone. Of these, three were analysed using IR-laser step-heating analyses on single grains (samples

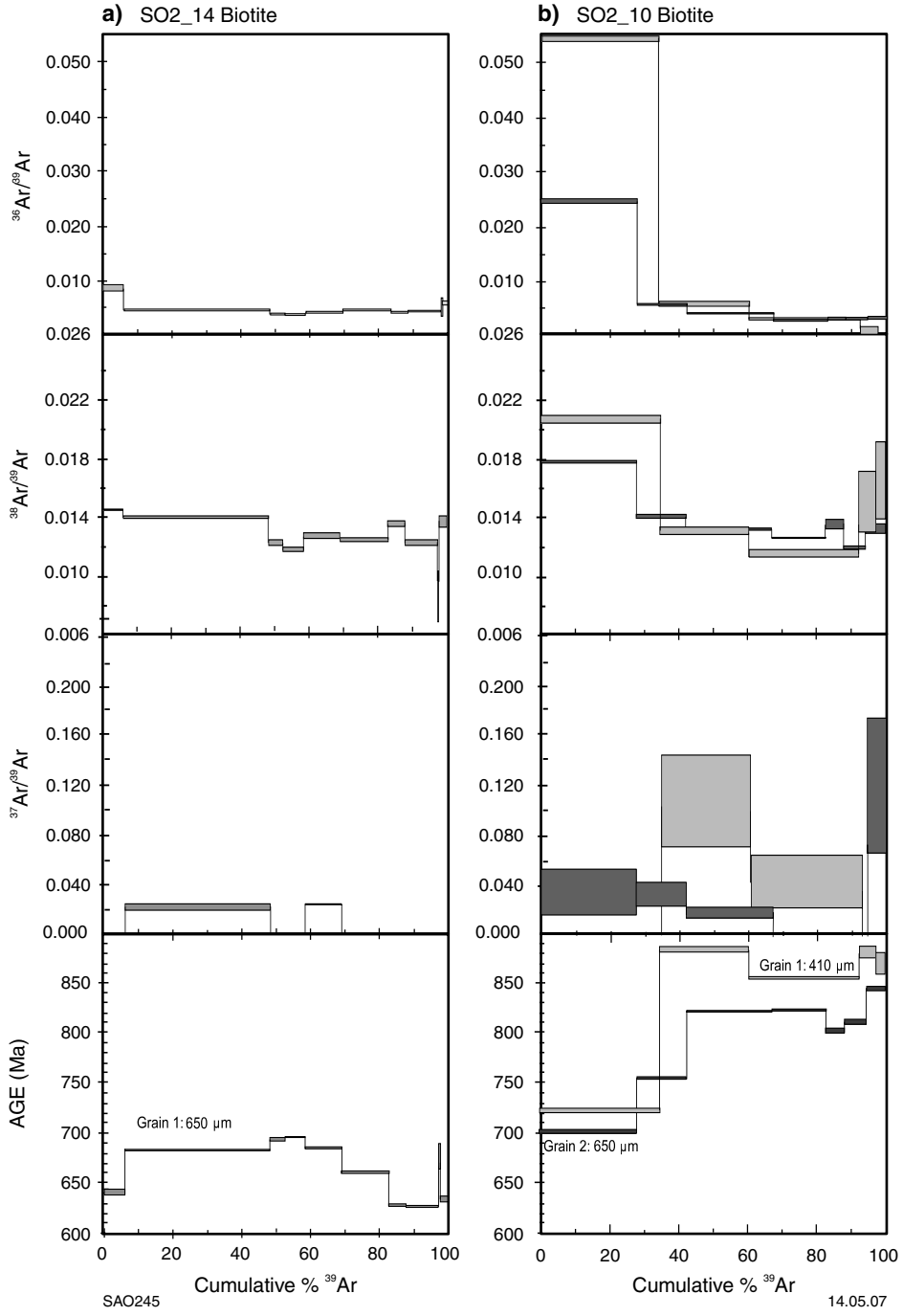

Figure 6. Single- and multiple-grain IR-laser step-heating data for biotite from the Errabiddy Shear Zone. Plots of apparent age and isotope variations vs cumulative %^{39}Ar

SO2_10, S02_14, SAO_01_08; Figs 6 and 7), five samples were analysed using IR-laser total-fusion analyses on single and multiple grains (142907, 142910, 142911, 168944, and 168946; Fig. 10; Table 1), and one sample was analysed using UV-laser probe analyses on spots and traverses on grains from a single sample (SAO_01_67; Fig. 11).

IR-laser step-heating data

For biotite from samples SO2_14 and SO2_10, plateaus could not be calculated for the age spectra (Fig. 6). Apparent ages for sample SO2_14 biotite range between 696 and 627 Ma. Variation in the age spectra for biotite from this sample is inversely correlated with $^{37}Ar/^{39}Ar$ and $^{36}Ar/^{39}Ar$, indicating that these parts of the analyses are compositionally distinct (Appendix 3; Fig. 6). Therefore, the unweighted mean age of 662 ± 26 Ma is interpreted as the best estimate for the time of $^{40}Ar/^{39}Ar$ closure for the sample. Age spectra for grains 1 and 2 from sample SO2_10 biotite show ranges of 722–885 and 701–844 Ma, respectively (Fig. 6). Age spectra for both grains are inversely correlated with $^{37}Ar/^{39}Ar$ and $^{36}Ar/^{39}Ar$, with the lower apparent ages, in the first step for grain 1 and

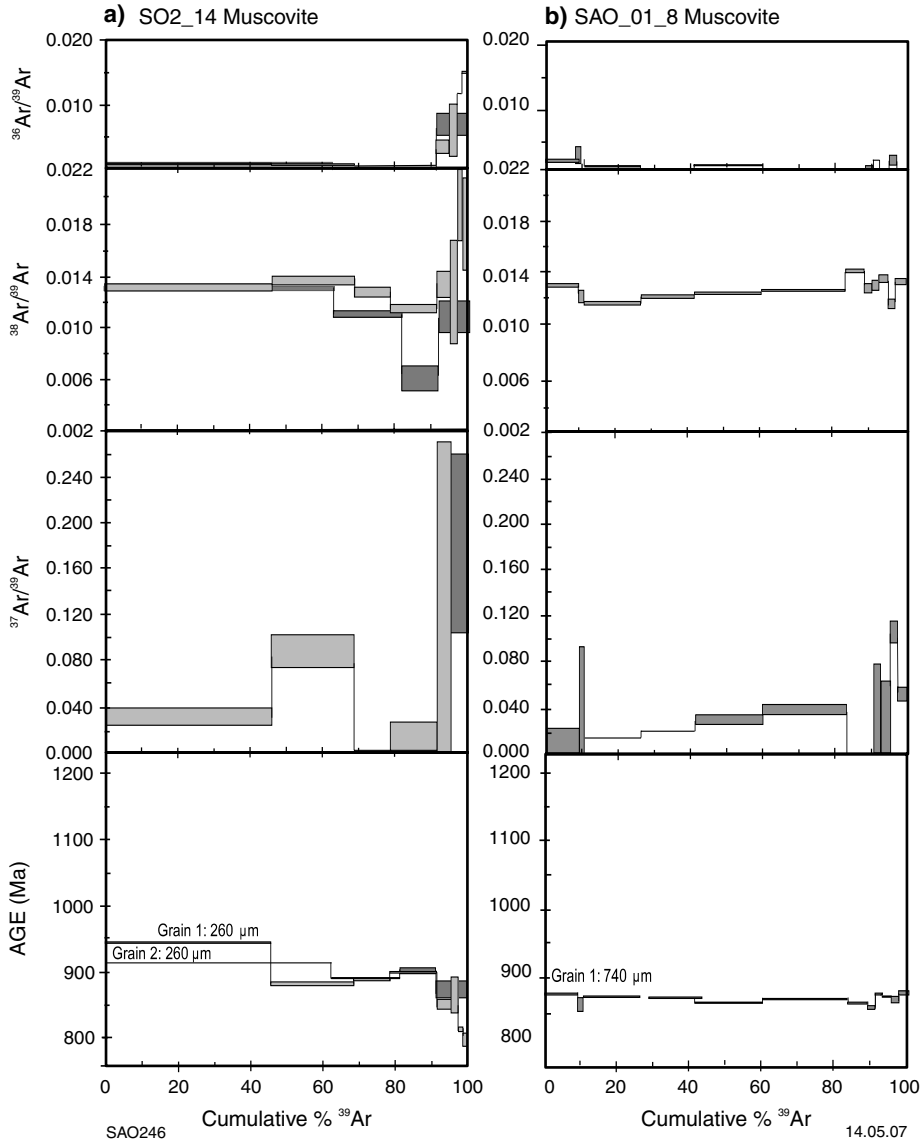

Figure 7. Single- and multiple-grain IR-laser step-heating data for muscovite from the Errabiddy Shear Zone. Plots of apparent age and isotope variations vs cumulative %Ar

the first two steps for grain 2, correlating with higher levels of $^{37}Ar/^{39}Ar$ and $^{36}Ar/^{39}Ar$. Given this correlation between calcium and atmospheric variations and apparent age, where $^{37}Ar/^{39}Ar$ is an indicator of Ca/K and ^{36}Ar is the assumed atmospheric component (McDougall and Harrison, 1999), the best estimate for the closure of both grains is taken as the unweighted mean ages of the last four steps of the analyses for grain 1, and steps 3–6 for grain 2, which are 874 ± 11 and 820 ± 14 Ma, respectively. The difference in ages corresponds to differences in grain size, with the larger grain (grain 2) yielding a younger apparent age.

Two samples of muscovite (of the same grain size) from sample SO2_14 produced age ranges of 942–801 Ma for grain 1, and 915–875 Ma for grain 2 (Table 1; Fig. 7a). Fluctuations in apparent age were partly coincident with changes in $^{38}Ar/^{39}Ar$ and $^{36}Ar/^{39}Ar$ for grain 1, with lower apparent ages measured in the last four steps correlating with higher proportions of chlorine and atmospheric argon. Given the possible compositional control on the youngest measured apparent ages, the presence of inclusions in the sample cannot be excluded. Therefore, unweighted mean ages, which do not take the youngest measured ages into account, are considered to be the most appropriate ages for grains 1 and 2 of sample SO2_14; these are 901 ± 24 and 903 ± 10 Ma, respectively.

Apparent ages from sample SAO_01_08 show a narrow age range of 881–864 Ma, with age fluctuations reflecting minor variations in calcium, chlorine, and $^{36}Ar/^{39}Ar$, and yielded an unweighted mean age of 872 ± 6 Ma (Fig. 7b; Table 1).

IR-laser total-fusion analyses

Single muscovite grains in sample 142907 show a significant age variation of 961–724 Ma for 110–40 µm grains (Table 1; Fig. 10c). This variation correlates broadly with grain size, with larger grains yielding older apparent

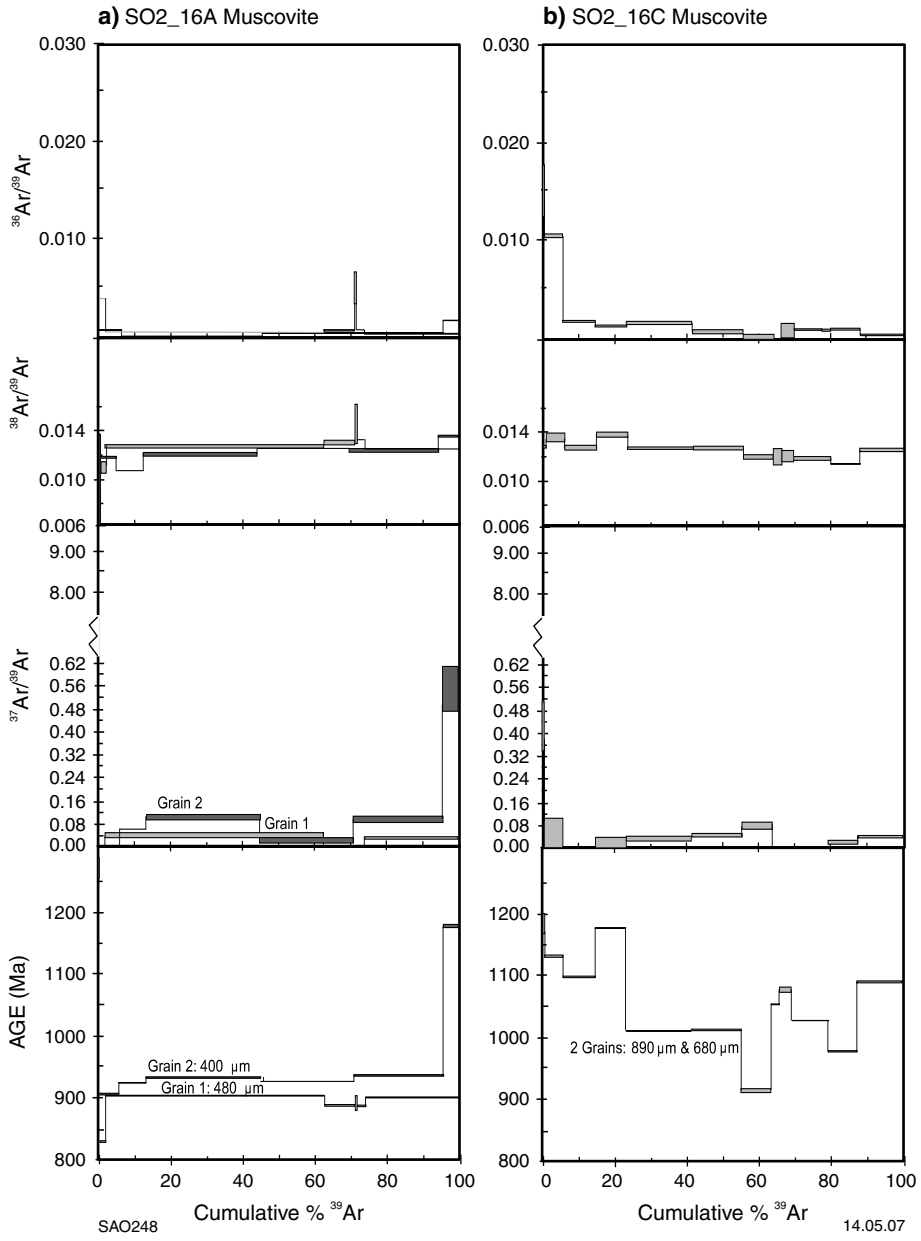

Figure 8. Single-grain IR-laser step-heating data for muscovite from the Glenburgh Terrane. Plots of apparent age and isotope variations vs cumulative %Ar

ages (Fig. 10c). Given the apparent correlation of age with grain size, the time of isotopic closure for grains of 70–220 µm size in this sample is taken to be between 724 ± 3 and 961 ± 4 Ma (Table 1).

Muscovite grains in sample 142910 produced a limited age range of 959–888 Ma and an unweighted mean age of 913 ± 20 Ma. The range of ages does not correlate with compositional differences, grain size, or atmospheric argon (Fig. 10d; Appendix 3). The broadly constant age versus grain size profiles (Fig. 10d) might have been caused by sample preparation; the grains may have been crushed to a smaller size than their true grain size. Alternatively, the presence of smaller domains within the individual grains (e.g. caused by the presence of fractures or kinks) may have resulted in destruction of the age profiles (cf. Kelley and Turner, 1991). Similarly, an age range of 1021–896 Ma from muscovite grains in sample 168944 is independent of grain size. However, two older grains dated at 1021 and 1012 Ma contain small amounts of calcium and are therefore compositionally different from other grains within the sample, which suggests that they may be contaminated with epidote or plagioclase inclusions (see Appendix 3). Apart from this anomaly, the apparent ages cannot be related to grain size or composition. The minimum age of 896 ± 9 Ma is interpreted as the time of isotopic closure for c. 100-µm muscovite grains in this sample (Table 1).

Individual biotite grains from sample 142907 gave an age range of 994–893 Ma, with an unweighted mean age of 927 ± 23 Ma. The age variation is not related to

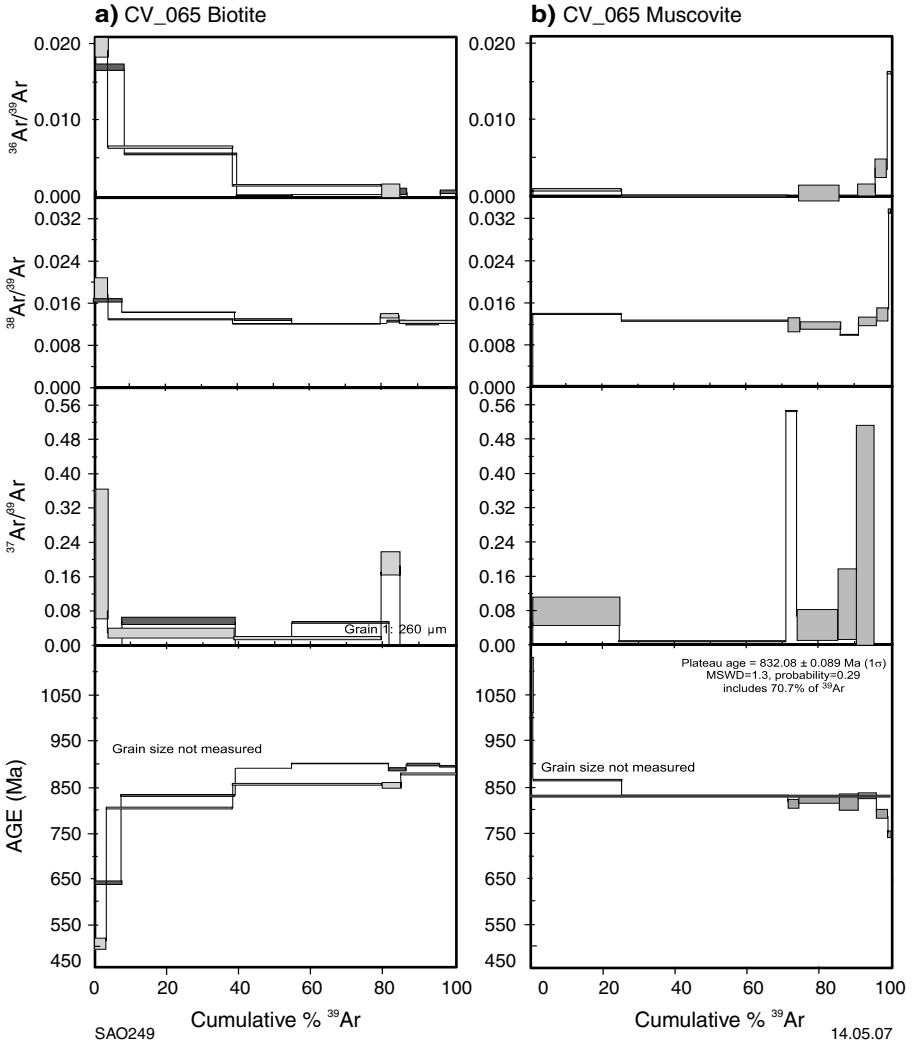

Figure 9. Single-grain IR-laser step-heating data for micas from the central Gascoyne Complex. Plots of apparent age and isotope variations vs cumulative %Ar

isotope distinctions (Fig. 10f); however, some of the coarsest grains yield the youngest apparent $^{40}Ar/^{39}Ar$ ages, suggesting contamination by excess argon. Biotite in sample 142911 exhibits a narrow range of ages between 964 and 888 Ma. However, the best estimate for the time of closure is the minimum age of 888 ± 7 Ma (measured on the largest grain). The oldest grain (dated at 964 ± 8 Ma) showed relatively higher $^{38}Ar/^{39}Ar$ and $^{37}Ar/^{39}Ar$ (see Appendix 3) than the other grains, indicating that it may contain small fluid inclusions, or has been contaminated with epidote or plagioclase.

Biotite sample 142910 shows a limited age range of 984–948 Ma and an unweighted mean age of 962 ± 10 Ma (Table 1; Fig. 10g). Biotite grains from sample 168944 yielded ages in the range 1263–1178 Ma, with an unweighted mean age of 1224 ± 26 Ma (Table 1). Biotite grains in sample 168946 yielded variable ages in the range 935–877 Ma, with an unweighted mean age of 905 ± 22 Ma. The apparent age variations in biotite grains from these three samples do not correlate with composition, atmospheric argon content, or grain size (Fig. 10g–i).

UV laser-probe analyses of sample SAO_01_67

Muscovite from sample SAO_01_67 was analysed using UV laser-probe analyses of individual spots and traverses (Fig. 11; Table 2). The data are complex, with variable ages within and between grains. The most common apparent ages measured are between 920 and 890 Ma (n = 10; Table 2). The oldest apparent age measured is 1251 ± 11 Ma and is 681 µm from the right-hand edge of grain 1. It is significantly older than the oldest age measured in grain 3 (1004 ± 5 Ma) at the grain centre. The distribution of ages with respect to the grain boundaries for grains 1 (diameter 1820 µm) and 3 (diameter 1000 µm) lie within two bell-shaped curves, and show apparent ages that mostly decrease from the centre towards the edge of the grains (Fig. 11). The distribution of ages with respect to grain-centre geometry is symmetric for grain 3, but asymmetric for grain 1. The decrease in ages towards the grain boundary indicates argon loss and is not consistent with diffusion of excess ^{40}Ar into the grain. This suggests that the ages within the grain centre represent incomplete loss of argon accumulated before the thermal event that led to

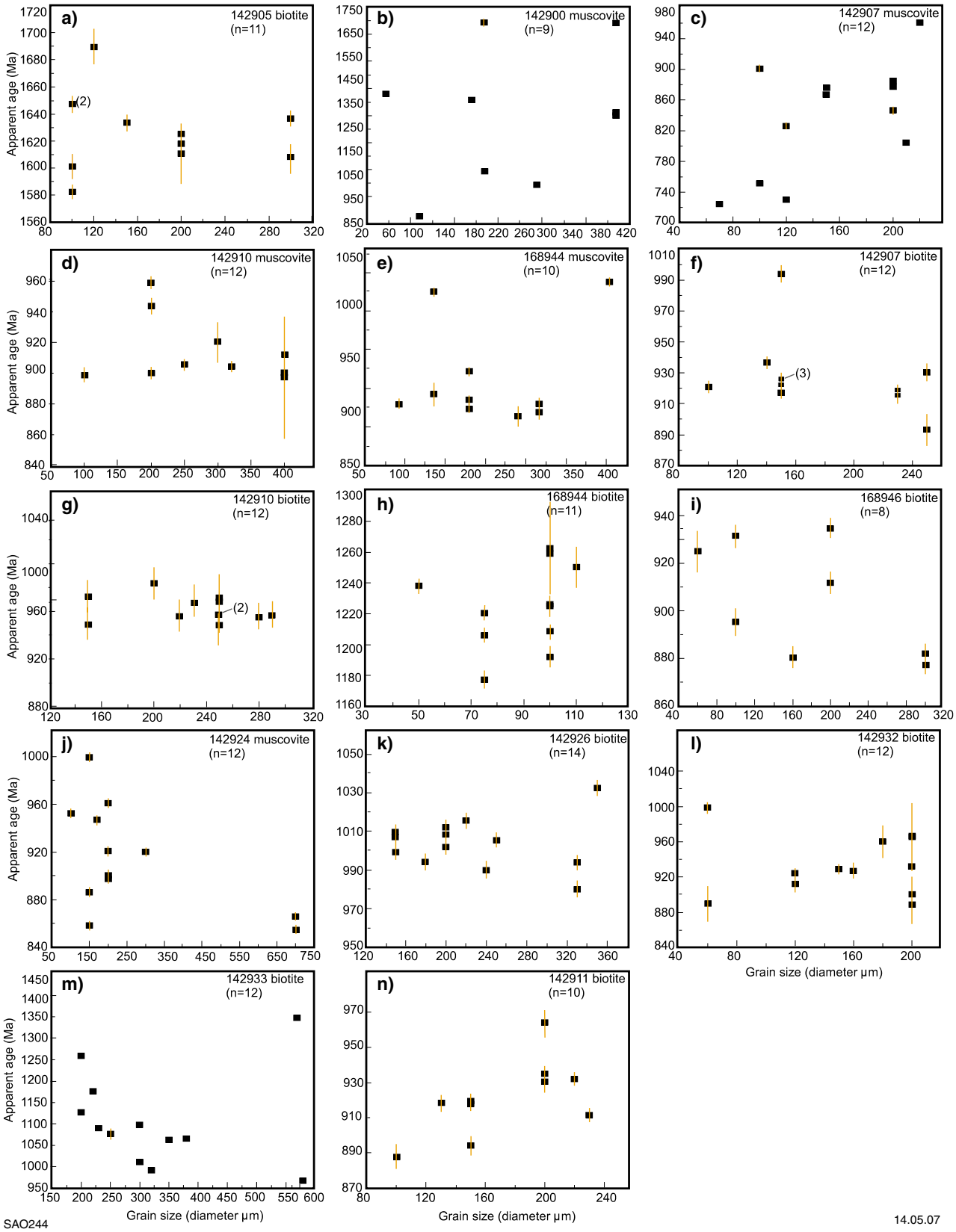

Figure 10. Relationships between grain size and age for muscovite and biotite analysed by IR-laser total-grain fusion on mostly single and rarely multiple grains, except muscovite from 142932. Analyses of sample 142932 were all on multiple grains of different sizes, and are not included. Note that error bars are small and thus in places fall within the limits of the symbol. The number of analyses per sample is noted; however, some symbols overlap, in which case the number of analyses is noted in parentheses beside the symbol

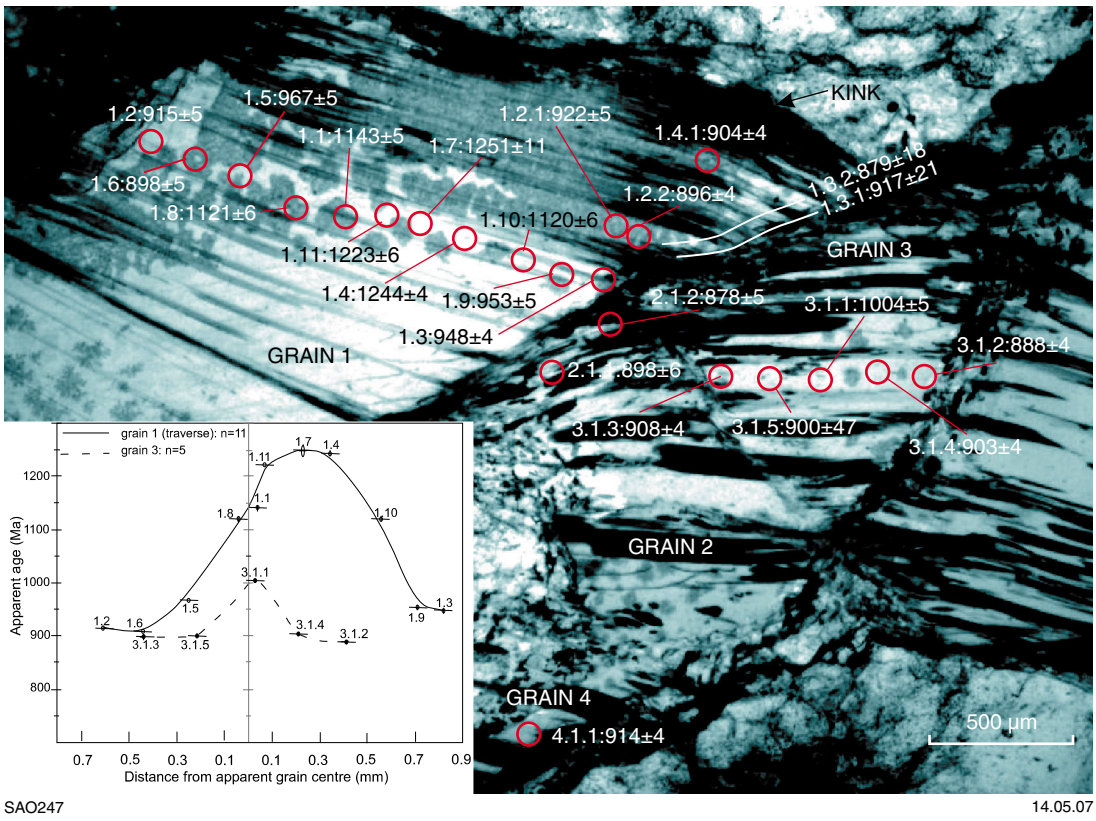

Figure 11. Photograph (plane-polarized light) of muscovite grains 1–4 from sample SAO_01_67, analysed by UV laser. Circles represent analysis spots (including damage haloes) and lines represent traverses. Ages (Ma) for spots and traverses are shown; uncertainties are ±1 . Inset: Distributions of UV-laser Ar–Ar ages relative to distance from apparent grain centres, for grains 1 and 3. Analysis numbers shown for spots and traverses, and analytical results are provided in Table 2

incomplete resetting. Therefore the youngest measured apparent age of 878 ± 5 Ma (analysis 2.1.2; Fig. 11) provides a minimum age for the last thermal event.

Gascoyne Complex

IR-laser step-heating data

Samples from the Gascoyne Complex analysed by the IR-laser step-heating method included muscovite from samples SO2_16A and SO2_16C, and muscovite and biotite from sample CV_065 (Figs 8 and 9; Table1).

Samples SO2_16A and SO2_16C were taken from the same locality and formation (Mount James Formation). For sample SO2_16A, grains 1 and 2 were individually analysed, and have diameters of 480 and 400 µm, respectively. For sample SO2_16C two grains with diameters of 890 and 680 µm were analysed in the same step-heating experiment. These two samples came from the same locality and were analysed to explore the variation of age with grain size, or among multiple grains. The age spectra show a correlation with grain size, with older apparent ages recorded from larger grains in sample SO2_16C (Fig. 8). Muscovite from grain 1 of sample SO2_16A yielded apparent ages between 1269 and 832 Ma. The first step yielded the oldest apparent age of 1269 ± 16 Ma and was the smallest step of the experiment (Appendix 3). This age also corresponds with the highest amount of atmospheric argon (13%; Table 1, Appendix 3). The remaining steps yielded apparent ages between 902 and 832 Ma. Muscovite grain 2 of sample SO2_16A yielded an age range of 1174–906 Ma, with the oldest apparent ages measured in the last steps, and corresponding with slightly higher $^{37}Ar/^{39}Ar$, $^{38}Ar/^{39}Ar$, and $^{36}Ar/^{39}Ar$ (Fig. 8a), which indicates compositional variation due to inclusion of more retentive minerals (e.g. plagioclase or epidote).

Although grains 1 and 2 in sample SO2_16A yielded generally flat apparent age spectra, they did not yield statistically valid plateaus. However, if J-value errors (Appendix 3) are included in the plateaus, then grains 1 and 2 yield plateau ages of 881 ± 15 and 929 ± 5 Ma, respectively. These plateaus include all but step 1 of ^{39}Ar (MSWD 0.78) for grain 1, and all but steps 1 and 6 of ^{39}Ar (MSWD 2.4) for grain 2.

Sample SO2_16C yielded apparent ages between 1182 and 914 Ma. Older ages in the first two steps correspond with higher levels of atmospheric argon (Fig. 8b). Given the irregularity in the data, the minimum measured age of 914 ± 4 Ma is considered to be the maximum age of $^{40}Ar/^{39}Ar$ isotopic closure of the sample.

Both muscovite and biotite were analysed from sample CV_065 (Fig. 9). Two grains of biotite gave similar

age spectra, with apparent ages increasing in a staircase pattern from the first step. Grains 1 and 2 yielded age ranges of 881–506 and 903–643 Ma, respectively. No statistically valid plateaus could be calculated from these data. The lower apparent ages in the first three steps of the analyses of grains 1 and 2 correlate with higher $^{37}Ar/^{39}Ar$, $^{38}Ar/^{39}Ar$, and $^{36}Ar/^{39}Ar$, indicating the possible presence of fluid inclusions, or the possibility of sample contamination.

Muscovite from sample CV_065 yielded an age spectrum with a plateau of 832 ± 1 Ma (1σ) (Table 1; Fig. 9b). The plateau includes 70.7% of the data (MSWD 1.3), excluding the first and last 2 steps. The last two steps gave lower apparent ages, corresponding with higher $^{38}Ar/^{39}Ar$ and $^{36}Ar/^{39}Ar$, indicating the possibility of sample contamination (e.g. the presence of plagioclase).

IR-laser total-fusion analyses

Muscovite from sample 142924 yielded single-grain total-fusion ages of 999–855 Ma, with an unweighted mean age of 914 ± 43 Ma (Table 1). There is no correlation between age and grain size or chlorine or calcium content (Appendix 3; Fig. 10j). However, the youngest apparent $^{40}Ar/^{39}Ar$ ages were measured on the largest grains (700 μm diameter), which suggests the presence of excess argon in the grains (Fig. 10j). Thus, the minimum $^{40}Ar/^{39}Ar$ age of 855 ± 3 Ma is interpreted to be a maximum age for isotopic closure for a 700 μm grain.

Muscovite grains from sample 142932 showed variable ages ranging from 963 to 880 Ma, with a minimum age of 880 ± 4 Ma. Most analyses from this sample were on two or more partly fused small grains (40–60 μm); therefore, the relationship between grain size and the age of individual grains could not be determined. In addition, there was no correlation between composition and measured apparent ages. Therefore, the minimum age is considered to be a maximum for isotopic closure.

Biotite grains from sample 142926 have an age range of 1032–964 Ma, and an unweighted mean age of 1001 ± 16 Ma (Table 1; Fig. 10k). The oldest ages mostly correspond to analyses that have relatively higher percentages of atmospheric argon. An exception is the youngest grain of biotite, which contains the highest percentage of atmospheric argon (12%) and more chlorine than the other grains, and is thus compositionally distinct (Appendix 3). It is therefore unlikely that either the oldest or the youngest age measured in this sample is representative of the true age of the biotite grains, and the best estimate for $^{40}Ar/^{39}Ar$ closure is taken to be the unweighted mean age of 1001 ± 16 Ma.

Biotite grains from sample 142932 yielded an age range of 966–888 Ma (Table 2), and show a weak correlation between grain size and age, with most of the smaller grains giving younger ages (Fig. 10l). There is also an inverse correlation between both $^{36}Ar/^{39}Ar$ and $^{38}Ar/^{39}Ar$ and age, with younger biotite grains commonly containing more atmospheric argon and chlorine than those with older apparent ages. However, the youngest apparent age of 889 ± 21 Ma was measured on the largest grain (200 μm) and is interpreted as the time of isotopic closure for that grain size.

Biotite grains from sample 142933 show a considerable age variation from 1346 to 967 Ma. For the most part, a broadly linear correlation between grain size and age shows that older ages correspond to smaller grains (Fig. 10m). This also corresponds with relatively higher percentages of atmospheric argon (Appendix 3), even though the atmospheric argon component is low (<5%; Table 1). Owing to the variability in the apparent ages of individual biotite grains within the sample, the minimum age of 967 ± 6 Ma is considered to be that of isotopic closure for a grain size of 580 μm.

Summary of $^{40}Ar/^{39}Ar$ age data

Histograms for single- and multiple-grain IR-laser total-fusion analyses, UV-laser single-point and traverse analyses of sample SAO_01_67, and apparent argon age spectra for step-heated analyses for biotite and muscovite show a wide range of apparent $^{40}Ar/^{39}Ar$ ages. These age ranges show considerable overlap between the different micas and within this range there are a number of well-defined age group peaks (Fig. 12, Table 1). For biotite analysed by IR total fusion, well-defined peaks were present between 1100 and 850 Ma, 1300 and 1200 Ma, and 1650 and 1600 Ma, with the greatest number of analyses (from the greatest number of samples) plotting within the 950–900 Ma peak (29 analyses), and twenty-four analyses plotting within the 1000–950 Ma peak (Fig. 12b). For biotite analysed by IR-laser step-heating experiments, most analyses yielded ages of 920–800 Ma (n = 19), although other groups at 1570–1440 Ma (n = 15), and 720–600 Ma (n = 13) are also significant. Thus, considering the two methods used to analyse biotite in this study, the most prominent $^{40}Ar/^{39}Ar$ ages obtained from biotite were within the range of 1000–800 Ma.

Argon ages for muscovite analysed by single- and multiple-grain total fusion range from 1750–700 Ma (Fig. 12a), with the most prominent argon ages in the 920–860 Ma range (28 analyses), slightly younger than that observed for biotite dated using the same technique. Single- and multiple-grain IR step-heating data for muscovite show a broad age range of c. 1290–730 Ma, which is a much smaller age range than for the data collected by the same method from biotite. The youngest ages have isotopic compositions indicating incorporation of inclusions or alteration. If these analyses are not included, then the youngest $^{40}Ar/^{39}Ar$ muscovite age is c. 780 Ma. The greatest number of analyses are dated between 925 and 800 Ma (n = 46), with the highest peak at 895–865 Ma (n = 21). Argon age data from muscovite from sample SAO_01_67 yielded an age range of 1250–860 Ma, similar to that reported in the step-heating data. Considering all of the biotite and muscovite $^{40}Ar/^{39}Ar$ data, the most prominent group of reliable ages is between 950 and 850 Ma.

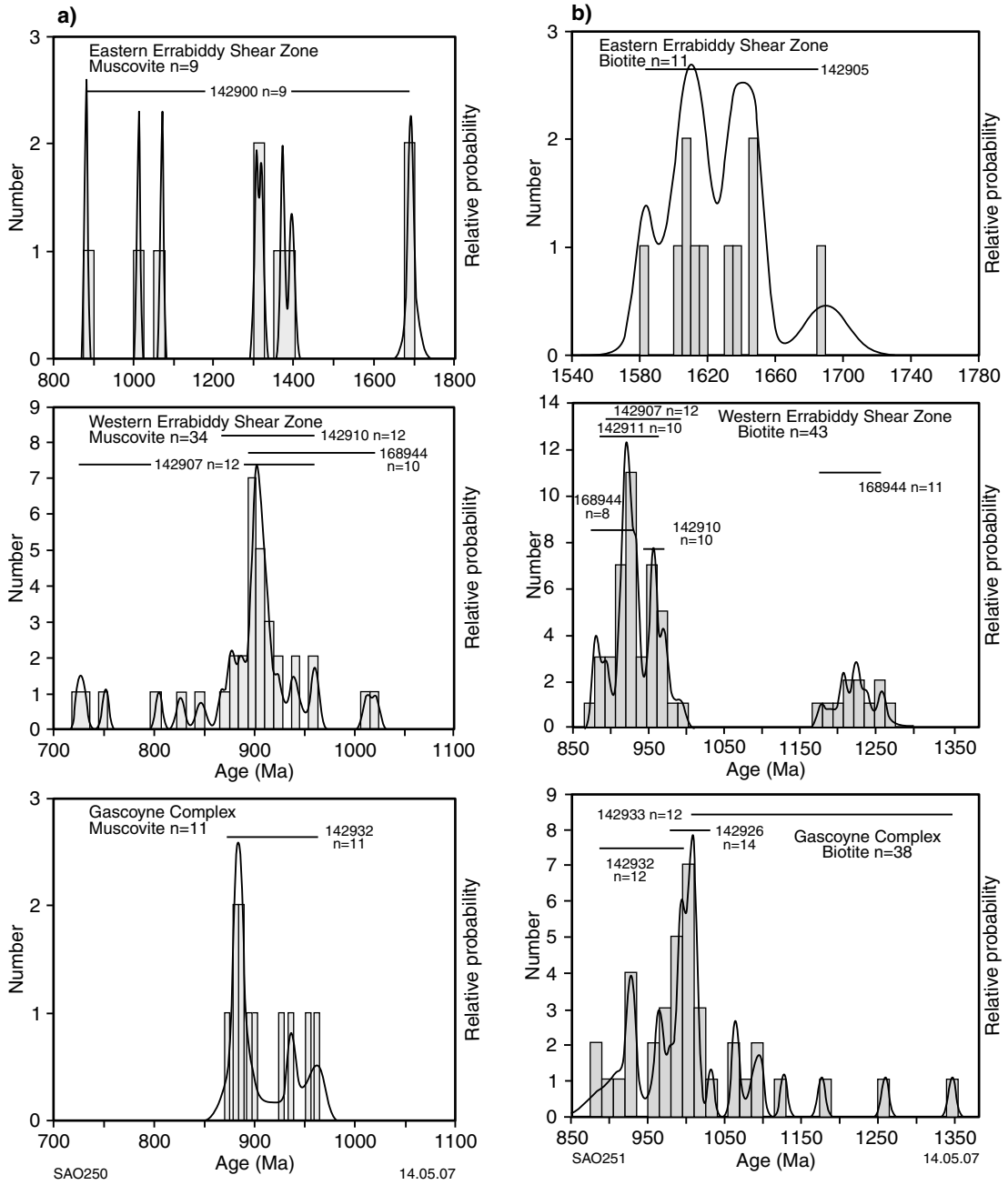

Figure 12. Combined probability density plots and histograms of ages measured in: a) muscovite, and b) biotite, by single-grain total fusion and some multiple-grain fusion of small grains (mainly <200 μm). Histogram bin width was 20 Ma. Horizontal lines annotated with sample numbers indicate the range of apparent ages (including 1σ uncertainties) obtained for individual samples. Histograms plotted using Isoplot (Ludwig, 2003)

Discussion

Isotopic diffusion, compositional variations, and excess argon

Complexities in $^{40}Ar/^{39}Ar$ age data can occur related to the concepts of 'closure temperature' or 'closure profiles' (Dodson, 1973), excess argon (Kelley, 2002; Kuiper, 2002), or compositional variations within the sample (Harrison et al., 1994; Kelley et al., 1986). $^{40}Ar/^{39}Ar$ ages can be interpreted as either crystallization ages or cooling ages, depending on the relationship of mineral growth or recrystallization to the thermal history of the rock (Dodson 1973). However, the thermal history of a mineral leads to the formation of closure profiles, even in the simple case of volume diffusion (Dodson, 1986). Closure profiles relate to diffusion in minerals, reflecting the necessity for material to diffuse from the centre to the edge of a grain before that material can be lost across a grain boundary. This can lead to intragranular age variations in mineral grains where only volume diffusion has occurred.

Not all apparent age heterogeneities for micas in this study can be explained in terms of grain-size variations or volume-diffusion parameters. For example, the step-heating analyses of two micas from sample SO2_16A from the Gascoyne Complex (Fig. 8) show that the smaller grain yielded the oldest apparent age. Such an anticorrelation between grain size and age cannot be explained in terms of simple diffusion and the closure temperature or closure profiles models. This suggests that heterogeneous excess argon, or compositional variations, may account for some of the age variations within the samples. For individual grains that were step-heated, variations in their apparent ages that are not related to compositional variation might be further complicated by phase changes that occur within the grain during step heating (Kuiper, 2002). Such phase changes can affect argon release from lattice sites by either homogenizing argon isotopes within a mineral, or releasing argon from areas within a grain in which the phase changes have taken place preferentially (Kuiper, 2002).

Grain-scale heterogeneity in argon-isotope systematics probably accounts for the variations in measured apparent ages. In all instances where $^{38}Ar/^{39}Ar$ was relatively high in the first low-temperature step or steps, $^{36}Ar/^{39}Ar$ was correspondingly high. In fact, the spectra for the $^{36}Ar/^{39}Ar$ versus cumulative percent ^{39}Ar, and $^{38}Ar/^{39}Ar$ versus cumulative percent ^{39}Ar for biotite samples CV_065, SO2_14, and SO2_10 are remarkably similar (Figs 6 and 9a). In addition, the last few steps of age spectra measured for muscovite grain 1 of SO2_14 and muscovite from CV_065 contain the same similarities. This increase (although typically only a small one) in $^{38}Ar/^{39}Ar$ and $^{36}Ar/^{39}Ar$ corresponds to apparent ages that are substantially younger than those calculated from subsequent analyses. Biotite from sample 142932, analysed by single-grain total fusion, also yielded younger apparent $^{40}Ar/^{39}Ar$ ages in grains with higher $^{36}Ar/^{39}Ar$ and $^{38}Ar/^{39}Ar$. For step-heated biotite samples, the release of ^{38}Ar may have been from near-surface cracks and partially opened inclusions (Kelley et al., 1986). Low temperatures may have caused thermal rupturing (decrepitation) of inclusions, especially those that were close to microfractures within the sample (Kelley et al., 1986). The qualitative correlation between chlorine and atmospheric argon in this study suggests that they are intrinsically associated, implying the interaction of hydrothermal fluids (brines) within the samples. These brines, possibly associated with formation of epidote, might have caused some alteration of the samples or may have been incorporated as fluid inclusions. Alternatively, the younger ages might represent argon loss from less retentive sites within the biotite.

For grain 1 of muscovite from sample SO2_14 and from CV_065, younger apparent ages were obtained in the higher temperature parts of the experiment, and were associated with higher atmospheric argon, chlorine, and calcium contents (Figs 7a and 9b). Kelley et al. (1986) suggested that in age spectra from chert with high chlorine and atmospheric argon components, in the higher temperature parts of an experiment, atmospheric argon and chlorine species might be contained within the quartz mineral lattice as defects or submicroscopic inclusions. This suggests that there might have been mineral lattice defects in the muscovite to allow for the presence of such submicroscopic inclusions, or that the muscovite contained small inclusions of quartz. Elevated calcium content suggests the presence of plagioclase inclusions in the sample.

The last step of age spectra measured from muscovite grain 2 of sample SO2_16A contains a significantly older apparent age and elevated chlorine, calcium, and atmospheric argon, which suggests that contaminants were possibly included in inclusions analysed in this step (cf. Harrison et al., 1993, 1994). Also, given that the apparent age measured from this step (c. 1174 Ma) is significantly older (by ≥238 Ma) than all other apparent ages measured for grain 2, it is possible that excess argon was included in the analysis. The measured apparent age for grain 2 (929 ± 5 Ma) is higher than that measured for the smaller grain 1 from the same sample. This also supports the conclusion that excess argon may have been incorporated into grain 2.

Apparent $^{40}Ar/^{39}Ar$ ages measured in biotite are older than those measured in muscovite from the same samples and the same range of grain sizes (e.g. Fig. 12; Table 1). In addition, the wide range of biotite $^{40}Ar/^{39}Ar$ ages measured within individual samples also suggests the presence of excess argon. Typically, higher closure temperatures would be expected for argon diffusion in muscovite than in biotite for the similar grain sizes analysed in this study (Villa, 1997). The inclusion of excess argon in biotite is well documented (e.g. Roddick et al., 1980; Dahl, 1996). Biotite is less retentive of ^{40}Ar than muscovite and may record anomalously old apparent ages, despite both minerals being exposed to the same metamorphic conditions. The presence of excess argon is supported by analyses of biotite from samples 142933 and SO2_10, which show an inverse correlation between grain size and age; that is, smaller grains yield older apparent $^{40}Ar/^{39}Ar$ ages (Figs 10m and 6b). In this case, the same amount of excess argon may be present in all of the grains; however, it forms a higher proportion in the smaller grains compared

with the radiogenic argon component. The smaller grains would also be able to equilibrate more quickly than larger grains. Thus if an 'excess argon' event is short lived, or the temperature of the event is low, the effects of that event would be more evident in smaller grains. The only way to evaluate this possibility would be to undertake in situ UV-laser analyses on biotite grains from these samples. If the grains contain excess argon they should yield age profiles with older ages at grain boundaries (or around favourable microstructural sites, such as kinks), and younger ages towards the centre of the grains. The only in situ UV-laser analyses undertaken in this study were on muscovite from sample SAO_01_67, which show increasing apparent $^{40}Ar/^{39}Ar$ ages towards grain centres, indicating that excess ^{40}Ar is unlikely to be present in that sample.

Interpretation of the $^{40}Ar/^{39}Ar$ ages

Taking into account the possibility of diffusion, excess argon, or compositional variations within and between grains, the apparent overlap of 960–820 Ma ages in the IR single-grain fusion, IR step-heating, and UV single-point and grain-traverse analyses cannot be ignored. Given that metamorphic foliations in the samples formed either during Archean or Paleoproterozoic deformation and thermal events, the $^{40}Ar/^{39}Ar$ age results from this study suggest that the rocks were subjected to temperatures that were sufficiently high to enable complete or partial resetting of argon during the Neoproterozoic.

The resulting complex apparent ages, obtained by different analytical methods, either represent the age of the Neoproterozoic thermal event alone (in the case of complete resetting of a grain, or part of a grain), or may reflect an inherited argon component. Differences in the age data suggest that rocks that experienced the same overall geological histories might have undergone thermal resetting at slightly different times, or were heated to different temperatures in the last thermal event, and might thus have had slightly different closure temperatures. In either case the different samples may be recording different parts of the cooling history of the region.

Argon ages of c. 1690–1600 Ma for both biotite and muscovite from the eastern part of the Errabiddy Shear Zone represent the time at which the samples last passed through their closure temperature. This range of cooling ages, although not recorded by other samples analysed in this study, reflects a tectonothermal event that may have affected all of the rocks, but resetting of it during the last thermal pulse may have been less effective in the northern part of the shear zone. This would be the case if the temperature of the thermal event in the north was lower than that in other areas. Other 'old' ages of 1630–1380 Ma for the Yilgarn Craton, and c. 1300–1200 Ma from samples from the Errabiddy Shear Zone, Yilgarn Craton, and Gascoyne Complex (Fig. 3) are also difficult to resolve, and may be attributable to excess argon in the samples, or to partial resetting during the Neoproterozoic. Modelling $^{40}Ar/^{39}Ar$ diffusion of muscovite, and comparison of the results with $^{40}Ar/^{39}Ar$ age profiles from in situ UV laser-probe analyses, shows that the apparent $^{40}Ar/^{39}Ar$ ages from the Capricorn Orogen may have been influenced by argon gas derived from earlier cooling events (Occhipinti and Reddy, 2004). This modelling suggests that the Neoproterozoic thermal event in the Capricorn Orogen could not have been at a temperature above 325°C.

The various methods used in the $^{40}Ar/^{39}Ar$ analyses in this study are all useful for different reasons. Single-grain fusion analyses were mostly completed on small grains. In these cases the argon isotopic compositions should be representative of the last thermal event experienced by the rocks, because volume-diffusion analysis suggests that smaller grains respond to diffusion more significantly than larger grains. For example, over the same period of time, the temperature required to completely reset argon in small grains is lower than that required to completely reset larger grains (McDougall and Harrison, 1999). Complexity in the single-grain fusion data may be partly the result of sample preparation. These samples were crushed and it is possible that some of the dated grains are fragments of coarser grains. This would lead to the lack of correlation between measured sample grain size and apparent age (Fig. 10), which is the case for several samples analysed in this study. Micas analysed by the step-heating method on individual grains were mostly larger than those used for the single-grain total-fusion analyses. Consequently, a complicated apparent age spectra is present, either because the last thermal event was not hot enough to completely reset the grains, or because of sample contamination, or excess argon, or a mixture of these factors.

The most useful method of argon analysis used during this study was the single-point UV analysis of muscovite in sample SAO_01_67. It is only by using this form of argon analysis that the detailed spatial distribution of ages within the grain could be documented. The results show that the youngest parts of the grain are around fast-diffusion pathways at grain boundaries or around kinks. The diffusion profiles measured in this muscovite are not consistent with diffusion of excess argon into the grain, and, therefore, excess argon is probably not the cause of heterogeneity of ages, at least not in this sample.

Rb–Sr ages of mineral separates reported from eleven localities in the Gascoyne Complex by de Laeter (1976) and Libby et al. (1999), and recalculated during this study using the decay constant $\lambda^{87}Rb = 1.42 \times 10^{-11}$, yielded a range between 715 ± 121 and 793 ± 21 Ma (±2σ). These are within the range of $^{40}Ar/^{39}Ar$ ages determined in this study. Of the Rb–Sr ages, five are from samples from the southern Gascoyne Complex (Glenburgh Terrane) and yielded recalculated two-point biotite–whole-rock isochrons ranging from 715 ± 121 to 793 ± 21 Ma. Two samples were from the central Gascoyne Complex (north of sample CV_065, Fig. 1). Multiple mineral separates were only analysed from two samples (20863 and 20872). Of these, one age was recalculated from a three-point biotite–muscovite–whole-rock errorchron at 772 ± 140 Ma (MSWD = 3.3), and one age was calculated from a four-point biotite–muscovite–microcline–whole-rock errorchron at 762 ± 59 Ma (MSWD = 6.5). The Rb–Sr ages are slightly younger than the most prominent group of $^{40}Ar/^{39}Ar$ ages of this study. It is difficult to assess the accuracy of the two-point biotite–whole-rock isochron ages because uncertainties cannot be accurately

determined. Indeed, the scatter in data from three- and four-point errorchrons (indicated by their high MSWD values) suggests that the ages may be unreliable.

Furnace step-heating to obtain $^{40}Ar/^{39}Ar$ ages from K-feldspar from the southern Capricorn Orogen gave total fusion ages (total gas ages) of 3060–466 Ma (Weber, 2002). K-feldspar from samples 142900, 142910, and 142911 (also used in this study) yielded ages of 951 ± 2, 1591 ± 14, and 754 ± 1 Ma, respectively. The K-feldspar argon ages quoted for samples 142900 and 142911 are comparable to ages calculated on micas in this study, with most of the K-feldspar from these samples yielding $^{40}Ar/^{39}Ar$ apparent ages between 1041 and 500 Ma (142900) and between 1103 and 468 Ma (142911). Argon ages for feldspar from sample 142910 ranged between 3232 and 644 Ma. The total fusion age of this sample was calculated at 1591 ± 14 Ma (Weber, 2002), which is significantly older than the argon ages obtained for mica from the same sample in this study (c. 962 Ma for biotite and c. 913 Ma for muscovite; Table 1), suggesting the presence of excess argon in the feldspars. This is also supported by the old ages measured in the initial low-temperature steps (e.g. for 142900 the first step contained an apparent age of c. 6900 Ma). The feldspars are also variably altered to sericite (Weber, 2002). The presence of excess argon and alteration in the feldspars suggests that the minimum argon ages, which range between 656 and 451 Ma, most likely reflect the time at which they cooled through their argon closure temperatures (which could be around 150°C; Figs 2 and 3). These minimum $^{40}Ar/^{39}Ar$ K-feldspar ages are considerably younger than the argon ages determined for biotite and muscovite in this study.

Tectonic implications

Argon ages of 960–820 Ma determined for micas in this study largely reflect cooling through closure temperatures between 350 and 270°C (depending on grain size and cooling histories). It is difficult to identify structures that can be related absolutely to the mica cooling ages in the region; however, the regional significance of the data cannot be ignored. They cover an area of approximately 17 000 km^2 crossing major tectonic boundaries and occur within units with contrasting deformation and metamorphic histories (Figs 1–3). The lack of detailed, coherent structural data attributable to the 960–820 Ma event also makes it difficult to assess the exhumation processes in the region. Thus, the only conclusion that can be drawn is that exhumation occurred on a regional scale between 960–820 Ma throughout the southern Capricorn Orogen.

The mica argon ages cannot be related to pervasive foliations that are present in rocks in the Gascoyne Complex and in the southern and central Capricorn Orogen generally, which are constrained to have formed earlier (Culver, 2001; Occhipinti and Reddy, 2004; Occhipinti et al., 2004). However, late brittle–ductile northerly and easterly trending structures throughout the southern Capricorn Orogen (Occhipinti and Reddy, 2004; Occhipinti et al., 2004), which overprint all tectonic units in the region, may have developed between 960 and 820 Ma. These structures may be temporally associated with open-to-isoclinal, northerly to easterly striking doubly plunging folds and steeply dipping faults, which are prevalent in the Bangemall Supergroup. These brittle and ductile structures might therefore have formed during the Edmundian Orogeny, which has previously been dated at between c. 1070 and c. 755 Ma on the basis of ages of deformed sills and cross-cutting undeformed dolerite dykes in the region (Wingate and Giddings, 2000; Wingate, 2002; Martin and Thorne, 2004; Wingate et al., 2004). The 960–820 Ma mica cooling ages suggest that deformation and metamorphism of the region during the Edmundian Orogeny either took place during this period, or before it, which makes the deformation and metamorphism considerably older than the previously published 755 Ma minimum age of orogenesis. However, there is a lack of structural evidence for a tectonic event younger than c. 1000 Ma in the Capricorn region that would force thermal resetting.

Protoliths of metasedimentary rocks in the Northampton and Mullingarra Complexes were likely sourced from the Albany–Fraser Orogen, which suggests that they were deposited much further south than their current positions (Kriegsman et al., 1999; Fitzsimons, 2003; Fig. 13). These rocks were deformed and metamorphosed in the granulite (Northampton Complex) or amphibolite (Mullingarra Complex) facies by c. 1080 or c. 1060 Ma, respectively (Fitzsimons, 2003), during the Pinjarra Orogeny. These metamorphic and deformation events are not evident in the adjacent Yilgarn Craton, which suggests that these terranes were deformed elsewhere, and brought into their current relative positions during dextral transpression after about 1080 Ma, and before 755 Ma (Fitzsimons, 2003), which corresponds to the age of the Mundine Well Dolerite Suite that cuts across the Northampton Complex and the West Australian Craton (Wingate and Giddings, 2000). This suggests that the major Neoproterozoic thermal event identified in the Gascoyne Complex may have been the result of a tectonic event along the western margin of Western Australia. Therefore, the Pinjarra and Edmundian Orogenies were probably the result of convergence of a continent with southwestern Australia during the early Neoproterozoic assembly of the Rodinian supercontinent (Pisarevsky et al., 2003). However, a model proposed by Fitzsimons (2003) suggests that the Northampton and Mullingarra Complexes were not transported northwards into their current positions until c. 755 Ma, on the basis of their current-day orientation and the brittle–ductile northerly trending dextral shear zones that post-date their emplacement (Byrne and Harris, 1993).

In response to dextral transpressive movements along the proto-Darling Fault, and the ensuing Edmundian and early Pinjarra Orogenies, structures that had previously developed in the Gascoyne Complex, which were largely easterly to northeasterly trending (Occhipinti and Reddy, 2004; Occhipinti et al., 2004) were possibly reactivated, and northerly trending brittle–ductile structures formed throughout the southern Capricorn Orogen (Occhipinti and Reddy, 2004; Occhipinti et al., 2004).

The $^{40}Ar/^{39}Ar$ age data presented here are consistent with a major period of tectonic uplift at c. 960–820 Ma in the Capricorn Orogen. Further evidence that

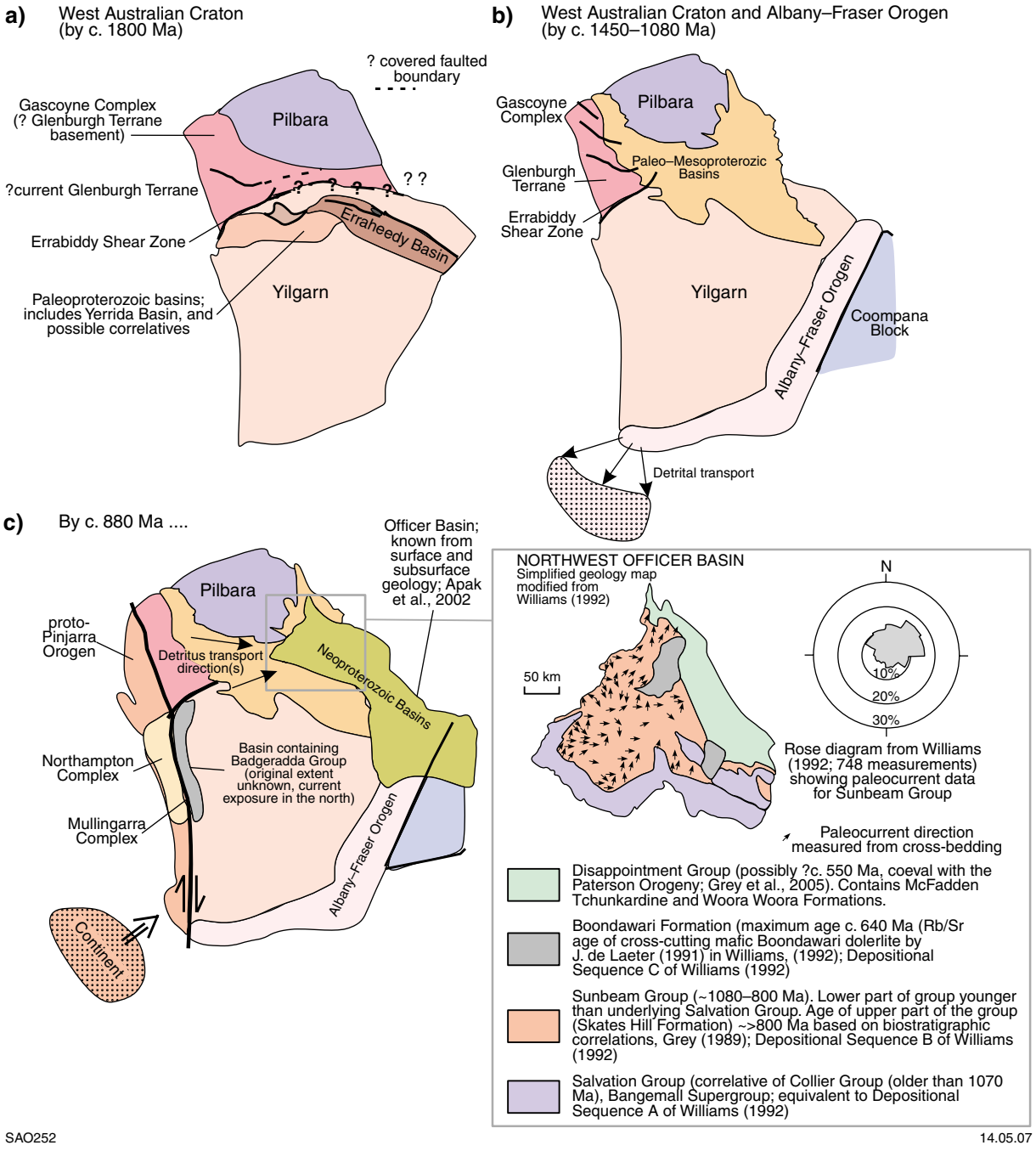

Figure 13. Simplified maps of the West Australian Craton and adjoining terranes: a) c. 1800 Ma, formation of the Western Australian Craton; b) 1450–1080 Ma, deposition of sediments now preserved in the Mullingarra and Northampton Complexes; c) c. 880 Ma, dextral transpressional deformation along the western part of Western Australia and emplacement of the Mullingarra and Northampton Complexes in their current positions. Intracontinental deformation initiated the Edmundian Orogeny in the Capricorn Orogen and uplift of the southern Capricorn Orogen, including the Gascoyne Complex, which led to deposition of detritus into the Neoproterozoic Officer Basin

supports tectonism at this time is the development of Neoproterozoic sedimentary basins in the region. The Neoproterozoic Officer Basin, which formed over central Western Australia, is thought to have developed as a sag basin and forms part of the Centralian Superbasin (Bagas, 2003; Grey et al., 2005). However, sedimentological data collected by Williams (1992) from the Sunbeam Group (which forms the base of the northwestern part of the Officer Basin) suggests that the group could equally have been deposited in a foreland basin setting with a fold-and-thrust belt to the west. Sedimentary rocks of the ?1070–800 Ma Sunbeam Group (Grey et al., 2005) were derived largely from the west (Williams, 1992; Fig. 13). Asymmetric sediment dispersion within the Sunbeam Group, coarsening upward successions, and the lack of any active volcanism associated with its development, together

support the possibility that the sediments were deposited in an intracontinental foreland basin setting (Cloetingh, 1988; Jordan, 1995; Miall, 1995). Intracontinental foreland basins develop where plate margin stresses are transmitted for thousands of kilometres from the plate margin, thereby initiating the formation of hinterland foreland basins a long way from the collision zone (Cloetingh, 1988; Miall, 1995).

Initial sediments in the northwestern Officer Basin were sourced from the Bangemall Supergroup and include fine- to medium-grained siliciclastics deposited in a tidal or intermittently emergent setting (Williams, 1992). A subsequent rapid increase in sediment supply accompanied by greater relief in the source region resulted in the deposition of conglomerates, of which many of the clasts were derived from the adjacent Bangemall Supergroup (Williams, 1992). Deposition of coarse- to medium-grained sandstone, granule and pebbly sandstone, and pebble, cobble, and boulder conglomerate with minor amounts of fine-grained sandstone and sandy siltstone followed (Williams, 1992). The pebble and cobble conglomerates, which are typically clast supported and form as lenses and thin beds, are in some places part of upward-coarsening sequences, and are indicative of non-marine clastic sedimentation (Grey et al., 2005). Interstitial clay (possibly after feldspar), zircon, and tourmaline (also present in the Gascoyne Complex; Occhipinti and Sheppard, 2001; Williams, 1986) are common. These rocks are overlain by dolomitic evaporites (commonly stromatolitic), medium- to fine-grained sandstone, siltstone, and, locally at their base, thick discontinuous conglomerates, all of which were likely deposited in a near-shore marine to coastal setting (Grey et al., 2005; Williams, 1992). Of these, sandy sediments were deposited in the western part of the basin, which is considered to have had a very low paleoslope (Grey et al., 2005).

The presence of abundant zircon and tourmaline indicates that granite may be a major source of sediment for the Sunbeam Group. In particular, abundant tourmaline suggests that Gascoyne Complex basement may have contributed to the sediment source. Detrital zircon populations in sedimentary rocks from the Tarcunyah Group at the base of the Officer Basin to the north of the Sunbeam Group suggest a great proportion of the detritus was also derived directly from the Gascoyne Complex (Bagas, 2003). The presence of dolomitic evaporite and siliciclastic rocks deposited in an environment with a low paleoslope at the end of Sunbeam Group sedimentation suggests that sediment supply from the west had decreased, perhaps indicating the end of active tectonism.

The paleocurrent direction and composition of sediments of the Sunbeam Group are consistent with derivation from the west, and therefore indicate significant topographic relief in the region of the Capricorn Orogen at c. 960–820 Ma. The mica cooling ages are consistent with occurrence of the Edmundian Orogeny at some time between 1070 and 755 Ma, and might represent: (a) a period of exhumation in the southern Capricorn Orogen related to the Edmundian deformation and metamorphic event; or (b) exhumation of rocks in the southern Capricorn Orogen as a result of orogenic collapse after the Edmundian Orogeny. Structures related to uplift of the southern Capricorn Orogen are not easily identifiable at map scale, owing to the paucity of outcrop, the apparent steep to vertically dipping nature of many faulted contacts, the lack of coherent detailed metamorphic data (mainly due to the rock types present), and the lack of direct dating of fabrics developed within high-strain zones (Occhipinti and Reddy, 2004). However, it is possible that the brittle–ductile structures throughout the southern Capricorn Orogen developed during this uplift event.

Conclusions

Dating of micas in the Capricorn Orogen by using $^{40}Ar/^{39}Ar$ laser techniques has shown that apparent ages do not reflect the maximum age of formation of greenschist facies metamorphic mineral assemblages, even though these assemblages are likely to have passed through their closure temperature for argon soon after they crystallized. This is because complicated geological histories in the period following foliation-forming metamorphic events can reset $^{40}Ar/^{39}Ar$ ages. Therefore, an $^{40}Ar/^{39}Ar$ age can be affected by excess argon, isotopic diffusion (with the effects of fast-diffusion pathways), and a convoluted geological history. The data also show that when using lasers to date $^{40}Ar/^{39}Ar$ cooling in micas, any method used will give an interpretable, meaningful result when factors such as grain size, structural modification of grains, compositional variations, and the possibility of analysing excess argon components are taken into account. However, the most robust method, and the one for which the results are easiest to interpret, is the UV laser-probe analysis of in situ grains.

Despite the complexity of the argon age data of this study, the results indicate that a major early Neoproterozoic orogenic event affected Western Australia. Orogenic events, basin formation, and the tectonic interactions of Western Australia with major continents have previously been viewed as separate occurrences that could not be linked. The Neoproterozoic tectonothermal event in the Capricorn Orogen involved the likely collision of a continent (possibly the Kalahari continent; Pisarevsky et al., 2003) during the amalgamation of Rodinia along the Pinjarra Orogen. During this event the Northampton and Mullingarra Complexes were emplaced by dextral transpression, the Mesoproterozoic Bangemall Supergroup was deformed and metamorphosed, the basement of the Gascoyne Complex was exhumed, and intracratonic sedimentary basins were formed.

References

APAK, S. N., GHORI, K. A. R., CARLSEN, G. M., and STEVENS, M. K., 2002, Basin development with implications for petroleum trap styles of the Neoproterozoic Officer Basin, Western Australia, *in* The sedimentary basins of Western Australia, *edited by* M. KEEP and S. J. MOSS: Petroleum Exploration Society of Australia Symposium, Perth, W.A., p. 914–926.

BAGAS, L., 2003, Zircon provenance in the basal part of the northwestern Officer Basin, Western Australia: Western Australia Geological Survey, Annual Review 2002–03, p. 43–52.

BYRNE, D., and HARRIS, L. B., 1993, Structural controls on the base-metal vein deposits of the Northampton Complex, Western Australia: Ore Geology Reviews, v. 8(1–2), p. 89–115.

CLOETINGH, S., 1988, Intraplate stress: a new element in basin analysis, *in* New perspectives in basin analysis *edited by* K. L. KLEINSPEHN and C. PAOLA: Springer-Verlag, New York, p. 205–230.

CULVER, K. E., 2001, Structure, Metamorphism and Geochronology of the Northern Margin of the Gurin Gutta Granite, Central Gascoyne Complex, Western Australia: Curtin University of Technology, Western Australia, BSc Hons thesis (unpublished).

DAHL, P. S., 1996, The crystal-chemical basis for Ar retention in micas: inferences from interlayer partitioning and implications for geochronology: Contributions to Mineralogy and Petrology, v. 123, p. 22–39.

de LAETER, J. R., 1976, Rb–Sr whole-rock and mineral ages from the Gascoyne Province: Western Australia Geological Survey, Annual Report 1975, p. 126–130.

DODSON, M. H., 1973, Closure temperature in cooling geochronological and petrological systems: Contributions to Mineralogy and Petrology, v. 40, p. 259–274.

DODSON, M. H., 1986, Closure profiles in cooling systems: Materials Science Forum, v. 7, p. 145–154.

DREW, B., 1999a, The geology of the Mount James Formation in the Coor-de-Wandy Hill area, Western Australia: Preliminary mapping report: University of Western Australia, Geology Department, Perth (unpublished).

DREW, B., 1999b, The geology of the Mount James Formation in the Coor-de-Wandy Hill study area, Western Australia: Laboratory report: University of Western Australia, Geology Department, Perth (unpublished).

FITZSIMONS, I. C. W., 2003, Proterozoic basement provinces of southern and southwestern Australia, and their correlation with Antarctica, *in* Proterozoic East Gondwana: Supercontinent assembly and breakup *edited by* M. YOSHIDA, B. F. WINDLEY, and S. DASGUPTA: Geological Society, London, Special Publication 206, p. 93–130.

GREY, K., 1989, Stromatolite evidence for the age of the Skates Hills Formation, Savory Basin: Western Australia Geological Survey, Palaeontology Report 16/89 (unpublished).

GREY, K., HOCKING, R. M., STEVENS, M. K., BAGAS, L., CARLSEN, G. M., IRIMIES, F., PIRAJNO, F., HAINES, P., and APAK, S. N., 2005, Lithostratigraphic nomenclature of the Officer Basin and correlative parts of the Paterson Orogen, Western Australia: Western Australia Geological Survey, Report 93, 75p.

HARRISON, T. M., HEIZLER, M. T., and LOVERA, O. M., 1993, In vacuo crushing experiments and K-feldspar thermochronometry: Earth and Planetary Science Letters, v. 117, p. 169–180.

HARRISON, T. M., HEIZLER, M. T., LOVERA, O. M., WENJI, C., and GROVE, M., 1994, A chlorine disinfectant for excess argon released from K-feldspar during step heating: Earth and Planetary Science Letters, v. 123, p. 94–104.

JORDAN, T. E., 1995, Retroarc Foreland and Related Basins, *in* Tectonics of Sedimentary Basins *edited by* C. J. BUSBY and R. V. INGERSOLL: Blackwell Science, p. 331–362.

KELLEY, S. P., 1995, Ar–Ar dating by laser microprobe, *in* Microprobe Techniques in the Earth Sciences *edited by* P. J. POTTS, J. F. BOWLES, S. J. D. REED, and M. R. CAVE: Chapman and Hall, London, p. 327–358.

KELLEY, S. P., 2002, Excess argon in K–Ar and Ar–Ar geochronology: Chemical Geology, v. 188, p. 1–22.

KELLEY, S. P., and TURNER, G., 1991, Laser probe ^{40}Ar–^{39}Ar measurements of loss profiles within individual hornblende grains from the Giants Range Granite, northern Minnesota, USA: Earth and Planetary Science Letters, v. 107, p. 634–648.

KELLEY, S. P., TURNER, G., BUTTERFIELD, A. W., and SHEPHERD, T. J., 1986, The source and significance of argon isotopes in fluid inclusions from areas of mineralization: Earth and Planetary Science Letters, v. 79, p. 303–318.

KINNY, P. D., WILLIAMS, I. S., FROUDE, D. O., IRELAND, T. R., and COMPSTON, W., 1988, Early Archaean zircon ages from orthogneisses and anorthosites at Mount Narryer, Western Australia: Precambrian Research, v. 38, p. 325–341.

KRAMER, N., COSCA, M. A., and HUNZIKER, J. C., 2001, Heterogeneous $^{40}Ar^{*}$ distributions in naturally deformed muscovite: in-situ UV-laser ablation evidence for microstructurally controlled intragrain diffusion: Earth and Planetary Science Letters, v. 192, p. 377–388.

KRIEGSMAN, L. M., MOLLER, A., and NELSON, D. R., 1999, P–T–t path and detrital zircon geochronology of the Northampton Block, Western Australia: a Mesoproterozoic, collisional induced foreland rift: Journal of Conference Abstracts, 4(1), p. 433.

KUIPER, Y. D., 2002, The interpretation of inverse isochron diagrams in $^{40}Ar/^{39}Ar$ geochronology: Earth and Planetary Science Letters, v. 203, p. 499–506.

LIBBY, W. G., de LAETER, J. R., and ARMSTRONG, R. A., 1999, Proterozoic biotite Rb–Sr dates in the northwestern part of the Yilgarn Craton, Western Australia: Australian Journal of Earth Sciences, v. 46, p. 851–860.

LUDWIG, K. R., 2003, Users manual for Isoplot/Ex version 3.0: a geochronological toolkit for Microsoft Excel: Berkeley Geochronology Center, Berkeley, CA, 56p.

McDOUGALL, I., and HARRISON, T. M., 1999, Geochronology and Thermochronology by the $^{40}Ar/^{39}Ar$ Method: Oxford University Press, New York, 269p.

MARTIN, D. McB., and THORNE, A. M., 2004, Tectonic setting and basin evolution of the Bangemall Supergroup in the northwestern Capricorn Orogen: Precambrian Research, v. 128, p. 385–409.

MIALL, A. D., 1995, Collision-Related Foreland Basins, *in* Tectonics of Sedimentary Basins *edited by* C. J. BUSBY and R. V. INGERSOLL: Blackwell Science, p. 393–424.

MIYASHIRO, A., 1994, Metamorphic petrology: UCL Press Ltd, London, 404p.

NELSON, D. R., 2000, Compilation of geochronology data, 1999: Western Australia Geological Survey, Record 2000/2.

NELSON, D. R., 2002, Compilation of geochronology data, 2001: Western Australia Geological Survey, Record 2001/2.

NELSON, D. R., ROBINSON, B. W., and MYERS, J. S., 2000, Complex geological histories extending from >4.0 Ga deciphered from xenocryst zircon microstructures: Earth and Planetary Science Letters, v. 181, p. 89–102.

NUTMAN, A. P., KINNY, P. D., COMPSTON, W., and WILLIAMS, I. S., 1991, SHRIMP U–Pb zircon geochronology of the Narryer Gneiss Complex, Western Australia: Precambrian Research, v. 52, p. 275–300.

OCCHIPINTI, S. A., and REDDY, S. M., 2004, Deformation in a complex crustal-scale shear zone: Errabiddy Shear Zone, Western Australia, *in* Flow Processes in Faults and Shear Zones *edited by* G. I. ALSOP, R. E. HOLDSWORTH, K. J. W. McCAFFREY, and M. HAND: Geological Society of London, Special Publications, London, p. 229–248.

OCCHIPINTI, S. A., and SHEPPARD, S., 2001, Geology of the Glenburgh 1:100 000 sheet: Western Australia Geological Survey, 1:100 000 geological Series Explanatory Notes, 37p.

OCCHIPINTI, S. A., SHEPPARD, S., MYERS, J. S., TYLER, I. M., and NELSON, D. R., 2001, Archaean and Palaeoproterozoic geology of the Narryer Terrane (Yilgarn Craton) and the southern Gascoyne Complex (Capricorn Orogen) — a field guide: Western Australia Geological Survey, 70p.

OCCHIPINTI, S. A., SHEPPARD, S., NELSON, D. R., MYERS, J. S. and TYLER, I. M., 1998, Syntectonic granite in the southern margin of the Palaeoproterozoic Capricorn Orogen, Western Australia: Australian Journal of Earth Sciences, v. 45, p. 509–512.

OCCHIPINTI, S. A., SHEPPARD, S., PASSCHIER, C., TYLER, I. M., and NELSON, D. R., 2004, Palaeoproterozoic crustal accretion and collision in the southern Capricorn Orogen: The Glenburgh Orogeny: Precambrian Research, v. 128, p. 237–255.

OCCHIPINTI, S. A., SHEPPARD, S., TYLER, I. M., SIRCOMBE, K. N., REDDY, S., HOLLINGSWORTH, D., MARTIN, D. McB., and THORNE, A. M., 2003, Proterozoic Geology of the Capricorn Orogen Western Australia — a field guide: Western Australia Geological Survey, Record 2003/16, 64p.

PIRAJNO, F., and ADAMIDES, N. G., 2000, Geology and mineralization of the Palaeoproterozoic Yerrida Basin, Western Australia: Western Australia Geological Survey, Report 60, 43p.

PISAREVSKY, S. A., WINGATE, M. T. D., POWELL, C. M., JOHNSON, S., and EVANS, D. A. D., 2003, Models of Rodinia assembly and fragmentation, *in* Proterozoic East Gondwana: Supercontinent assembly and breakup *edited by* M. YOSHIDA, B. F. WINDLEY, and S. DASGUPTA, Geological Society, London, Special Publication 206, p. 35–55.

REDDY, S. M., KELLEY, S. P., and WHEELER, J., 1996, A $^{40}Ar/^{39}Ar$ laser probe study of micas from the Sesia Zone, Italian Alps: implications for metamorphic and deformation histories: Journal of Metamorphic Geology, v. 14, p. 493–508.

REDDY, S. M., and OCCHIPINTI, S. A., 2004, High-strain zone deformation in the southern Capricorn Orogen, Western Australia: Kinematics and age constraints: Precambrian Research, v. 128, p. 295–314.

REX, D. C., and GUISE, P. G., 1995, Evaluation of argon standards with special emphasis on time scale measurements, *in* Phanerozoic Time Scale *edited by* G. S. ODIN: Bulletin of Liaison and Information, IUGS Subcommission on Geochronology, p. 21–23.

RODDICK, J. C., CLIFF, R. A., and REX, D. C., 1980, The Evolution of Excess Argon in Alpine Biotites — A $^{40}Ar/^{39}Ar$ Analysis: Earth and Planetary Science Letters, v. 48, p. 185–208.

SHEPPARD, S., and OCCHIPINTI, S.A., 2000, Geology of the Errabiddy and Landor 1:100 000 sheets: Western Australia Geological Survey, 1:100 000 Geological Series Explanatory Notes, 37p.

SHEPPARD, S., OCCHIPINTI, S. A., and NELSON, D. R., 2005, Intracontinental reworking in the Capricorn Orogen, Western Australia: the 1680–1620 Ma Mangaroon Orogeny: Australian Journal of Earth Sciences, v. 52, p. 443–460.

SHEPPARD, S., OCCHIPINTI, S.A., and TYLER, I.M., 2003, The relationship between the tectonic setting and composition of granitoid magmas, Yarlarweelor Gneiss Complex, Western Australia: Lithos, v. 66, p. 133–154.

SHEPPARD, S., OCCHIPINTI, S. A., and TYLER, I. M., 2004, A 2005–1970 Ma Andean-type batholith in the southern Gascoyne Complex, Western Australia: Precambrian Research, v. 128, p. 257–277.

SHEPPARD, S., and SWAGER, C. P., 1999, Geology of the Marquis 1:100 000 sheet: Western Australia Geological Survey, 1:100 000 Geological Series Explanatory Notes, 21p.

VARVELL, C. A., 2001, Age, Structure and Metamorphism of a section of the Morrissey Metamorphic Suite, Central Gascoyne Complex, Western Australia: Curtin University of Technology, Western Australia, BSc Hons thesis (unpublished).

VILLA, I. M., 1997, Isotopic closure: Terra Nova, v. 10(1), p. 42–47.

WEBER, U. D., 2002, The thermotectonic evolution of the northern Precambrian Shield, Western Australia. PhD Thesis: Melbourne, The University of Melbourne, (unpublished).

WILLIAMS, I. R., 1992, Geology of the Savory Basin, Western Australia: Western Australia Geological Survey, Bulletin 141, 115p.

WILLIAMS, I. R., and MYERS, J. S., 1987, Archaean geology of the Mount Narryer region, Western Australia: Western Australia Geological Survey, Report 22, 32p.

WILLIAMS, S. J., 1986, Geology of the Gascoyne Province, Western Australia: Western Australia Geological Survey, Report 15, 85p.

WILLIAMS, S. J., WILLIAMS, I. R., and HOCKING, R. M., 1983, Glenburgh, W.A.: Western Australia Geological Survey, 1:250 000 Geological Series Explanatory Notes, 25p.

WINGATE, M. T. D., 2002, Age and palaeomagnetism of dolerite sills of the Bangemall Supergroup on the Edmund 1:250 000 sheet, Western Australia: Western Australia Geological Survey, Record 2002/4, 48p.

WINGATE, M. T. D., and GIDDINGS, J. W., 2000, Age and palaeomagnetism of the Mundine Well dyke swarm, Western Australia: implications for an Australia–Laurentia connection at 755 Ma: Precambrian Research, v. 100, p. 335–357.

WINGATE, M. T. D., PIRAJNO, F., and MORRIS, P. A., 2004, Warakurna large igneous province: A new Mesoproterozoic large igneous province in west-central Australia: Geology, v. 32(2), p. 105–108.

Appendix 1

Sample locations, rock unit, field information, and SHRIMP ages

Area	*Sample # Unit name and location (AMG)[a] Zone 50*	*Field notes Locality information*	*Petrographic summary*	*Interpreted U–Pb SHRIMP age on zircon, or bracketed age*
Narryer Terrane (Yilgarn Craton)	S02_02a ?Archean granite (513940E 7149900N)	Granite dyke intruding surrounding granitic gneiss and quartz mylonite. Granite contains xenoliths of surrounding gneiss, is less deformed than gneiss but contains a weak foliation along its margins, which trend parallel to the foliation in the surrounding gneiss	Unfoliated quartz, feldspar, muscovite, and biotite granite. Contains abundant accessory zircon	Unknown
	SO2_7a Narryer Gneiss Complex (494780E 7169128N)	Granitic gneiss containing muscovite and biotite	Granitic gneiss with gneissocity defined mostly by quartz, biotite, and muscovite. Contains quartz, feldspar, muscovite, and biotite, with accessory epidote and zircon. Quartz displays undulose extinction, minor sub-grain development and brittle fracture	Unknown
	SO2_8 Narryer Gneiss Complex (489082E 7171896N)	Lens of biotite schist in weathered granitic gneiss.	Well-foliated, with the foliation defined by phlogopite (biotite), and feldspar, including K-feldspar, and quartz. Foliation wraps around porphyroblasts of possible sillimanite or andalusite that have been pervasively pseudomorphed by randomly oriented sericite and quartz	Unknown
Errabiddy Shear Zone (ESZ)	142900 Moorarie Supersuite (529856E 7197186N)	Small plug of unfoliated muscovite–biotite granite associated with larger mass of foliated two-mica coarse granite and pegmatite. Intruded late during the Capricorn Orogeny	Microcline (25%), albite–oligoclase (25%), quartz (35%), biotite (5%), muscovite (5%), and garnet (1–3%), sericite and chlorite. Sericite partially replaces feldspar and biotite, and chlorite partially or completely replaces garnet and biotite. Muscovite and biotite range in grain size from 30–300 µm	1802 ± 9 Ma
	142905 Camel Hills Metamorphics — (migmatitic pelitic gneiss) (547712E 7210422N)	A weak gneissocity that is folded about upright, tight-isoclinal folds and retrogressed in the greenschist facies during this folding event. Folds developed during the Capricorn Orogeny	Quartz, plagioclase, K-feldspar, biotite, muscovite, sericite, sillimanite, garnet, and chlorite. Garnet flattened in the foliation. Accessory minerals: zircon and apatite Plagioclase–andesine–oligoclase, locally replaced by sericite. K-feldspar grains pseudomorphed by sericite. Sericite forms mats over sillimanite. Garnet is variably replaced by chlorite and sericite. Biotite 50–600 µm long, commonly 200–300 µm long. Larger biotite grains contain abundant inclusions of opaques and zircon, and smaller grains (50–100 µm) are either inclusion free, or contain fewer inclusions relative to the larger grains. Biotite is often partially replaced by muscovite and/or sericite, and muscovite grains are of a similar size variation to biotite	Migmatite c. 1950 Ma (see text); sedimentary protolith <2052 ± 7 Ma
	142907 Biotite monzogranite dyke (unnamed) (504168E 7181130N	Dyke that intrudes mesocratic porphyritic granite and mesocratic granitic gneiss. Deformed by narrow greenschist facies east-northeast-trending shears	Feldspar, quartz, biotite, epidote, and muscovite. Feldspar (50%) consists of even amounts of plagioclase and K-feldspar Biotite replaced locally by muscovite. Epidote and sericite replace feldspar Biotite is up to 260 µm long but most grains are 50–100 µm long. Only 25% grains in range 200–260 µm long. Foliation is defined by aligned clusters of biotite; whereas fine-grained muscovite/sericite is not aligned in the foliation. Some biotites are oriented perpendicular to the foliation and may have crystallized post-foliation formation	2608 ± 3 Ma

Appendix 1 (continued)

Area	*Sample # Unit name and location (AMG)[a] Zone 50*	*Field notes Locality information*	*Petrographic summary*	*Interpreted U–Pb SHRIMP age on zircon, or bracketed age*
	142910 Camel Hills Metamorphics (477900E 7184200N)	Migmatitic pelitic gneiss. Age of partial melting interpreted from 2 youngest zircons in sample. Intruded by sample 142909 at 1970 ± 15 Ma (Nelson, 1999)[b]	As for 142905 (above), except this sample is foliated. One well-developed foliation is present and is defined by domains of biotite aggregates, with minor muscovite, and mainly ex-sillimanite (now mats of sericite) and separate domains of quartz and plagioclase	Migmatite c. 1950 Ma (see text); sedimentary protolith <2025 ± 8 Ma
	SAO_02_10 Warrigal Gneiss (470815E 7178831N)	Granitic gneiss consisting of quartz, feldspar (K-feldspar), biotite, garnet, muscovite, sericite, ?epidote, apatite, and zircon. Layers consisting mostly of biotite aggregates define a foliation in the gneiss	Feldspar (45%), quartz (45%), biotite (5%), garnet (<1%), epidote, sericite. Accessory minerals: zircon, opaques. Biotite is up to 300 µm long, but commonly 50–100 µm long. Larger grains often contain inclusions of zircon or opaques. Feldspar is deformed, but not recrystallized and is locally replaced by sericite and epidote. Quartz is recrystallized, but may have formed ribbons throughout the gneiss. Garnet is cracked (pulled apart). Within and around the cracks biotite, quartz, and minor epidote have crystallized. Foliation is defined by alignment of biotite clusters and relic quartz ribbons	This locality not dated; however, elsewhere in the ESZ precursor is granite to granitic gneiss dated by SHRIMP at 2700–2600 Ma
	SAO_01_08 Coor-de-wandy Formation (433425E 7162519N)	Low-grade metasedimentary rock	Quartz (50%), white mica (?45%) and accessory zircon, tourmaline, apatite, magnetite, and ilmenite. Muscovite and quartz define an undifferentiated foliation	Unknown
	SO2_14 Erong Granite (465738E 7174602N)	Medium-grained, even-textured to coarse-grained event-textured biotite–muscovite–garnet granodiorite, which intrudes Peter Calcsilicate of the Camel Hills Metamorphics	Plagioclase, quartz, K-feldspar (collectively >93%) with minor biotite, muscovite, and epidote (~5%)	Not dated by SHRIMP; <c. 2000 Ma
	SAO-01_67 ?Bertibubba Supersuite or ?Moorarie Supersuite (477962E 7184265)	Coarse-grained unfoliated muscovite pegmatite dyke. The pegmatite cuts main foliation in migmatized pelite, trending north-northeast	Quartz, feldspar, muscovite. Accessory mineral: zircon. Quartz rich granite. Minor replacement of feldspar by sericite. Muscovite consists of books up to 3 mm long	Unknown
	168944 Camel Hills Metamorphics (449690E 7171338N)	Medium-grade (amphibolite facies) psammite. Age of protolith sedimentary rock and possible youngest protolith age (c. 1985 Ma)	Quartz (50%), plagioclase (andesine 20%), biotite (15–20%), muscovite (10%), minor myrmekite and epidote. Accessory phases: zircon and ?apatite. In places, a possible weak foliation defined by biotite but the rock is mostly recrystallized and unfoliated. Fine-grained muscovite and biotite intergrown in clumps throughout. Muscovite pseudomorphs biotite. Sericite partly replaces muscovite and biotite, as well as plagioclase. Biotite and muscovite have variable grain sizes of 30–250 µm and 50–100 µm, respectively. However, most of the biotite grains are 100–200 µm. Quartz is commonly granoblastic and annealed. Minor sub-grain development has taken place within the larger grains and undulose extinction of grains is common. Small quartz grains have crystallized around larger ones, and around feldspar grains	1985 ± 14 Ma; most protolith 2028 ± 5 Ma
	142911 Bertibubba Supersuite (460034E 7167064N)	Foliated porphyritic biotite monzogranite. This granite contains one pervasive foliation. This phase intrudes sample 142912 (Nelson, 1999)[b]	Feldspar (50–65%), quartz (25–30%), biotite (10%), muscovite (2%), epidote (2%), and myrmekite. Accessory minerals: titanite, minor opaques. Large 5–8 mm-long rectangular feldspar porphyroclasts composed of both K-feldspar and oligoclase–andesine are wrapped by intergrown biotite and muscovite, which are aligned in the foliation. Smaller feldspar grains also present. Biotite grains are	1961 ± 3 Ma

Appendix 1 (continued)

Area	*Sample #* *Unit name and location (AMG)[(a)]* *Zone 50*	*Field notes* *Locality information*	*Petrographic summary*	*Interpreted U–Pb SHRIMP age on zircon, or bracketed age*
			commonly about 300 μm long, with some as long as 600 μm, and some as small as 80 μm long. Small (c. 0.3 mm) quartz grains are flattened in the foliation directly adjacent to the porphyroclasts; however, away from the feldspar porphyroclasts they form larger more equant grains. Epidote forms abundant small euhedral crystals that clump around biotite and small feldspar grains	
	168946 Bertibubba Supersuite (433020E 7165590N)	Medium to coarse-grained, even-textured tonalite (foliated)	Plagioclase (40%), quartz (30%), microcline (20%), biotite (5–10%), muscovite (2–5%), and minor epidote with accessory zircon. Biotite and muscovite grains range in size between 50–600 μm, and 20–10 μm long, respectively. Foliation defined by biotite-richer zones where biotite is roughly aligned alternating with quartz-feldspar rich domains. Feldspar is locally replaced by sericite. Quartz is commonly recrystallized into grain free polygonal grains. Muscovite is not aligned in any foliation, and locally replaces biotite	1961 ± 6 Ma
Glenburgh Terrane	142924 Moorarie Supersuite (443590E 7204385N)	Fine to medium, even-grained monzogranite. Intrudes monzogranite with 5 cm mafic clots	Plagioclase (35%), microcline (20%), quartz (35%), muscovite (5%), and biotite (2–3%) with minor epidote, and sericite. Accessory minerals: zircon and apatite. Fine crystals of epidote and sericite partially replace feldspar. Sericite also partially replaces biotite. Muscovite and biotite are randomly oriented throughout the rock. Muscovite is the most prominent mica in the sample, and is up to 500 μm long; however, most grains are smaller (100–250 μm long). Most biotite grains are 50–200 μm long. In places, quartz forms elongate domains in which some of the quartz grains are flattened, implying that they may represent foliation domains within this otherwise massive, undeformed rock	1827 ± 14 Ma
	142926 Dalgaringa Supersuite (443290E 7199960N)	Biotite tonalite. Veined by fine-grained biotite monzogranite	Feldspar (60%), quartz (30%), biotite (10%), minor epidote and sericite. Accessory minerals: zircon, apatite, and titanate. Biotite roughly aligned, defining foliation. Biotites mostly 50–250 μm long. Larger biotite grains usually riddled with inclusions of zircon and titanite. Feldspar is mainly plagioclase consisting of andesine, and oligoclase–andesine, with minor (<5%) microcline	2002 ± 2 Ma
	142932 Nardoo Granite (Dalgaringa Supersuite) (425750E 7187380N)	Porphyritic granodiorite. Intrudes deformed fine-grained tonalite gneiss and amphibolite of ‘older’ Dalgaringa Supersuite	Feldspar (45%), quartz (30%), biotite (10%), muscovite, sericite, and epidote. Accessory minerals: zircon, titanite, and opaques. Biotite ranges in size from 100 μm – 1 mm, and the larger biotites generally contain abundant small inclusions of opaques and zircon. Biotite occurs as aligned crystals in clumps throughout the rock, defining a foliation. Subordinate muscovite is also aligned in the foliation. Feldspar mostly comprises andesine–oligoclase, with subordinate K-feldspar and is locally sericitized	1977 ± 4 Ma

Appendix 1 (continued)

Area	*Sample # Unit name and location (AMG)[a] Zone 50*	*Field notes Locality information*	*Petrographic summary*	*Interpreted U–Pb SHRIMP age on zircon, or bracketed age*
	142933 Dalgaringa Supersuite (421290E 7189830N)	Biotite–orthopyroxene–clinopyroxene–andesine granulite; meta quartz diorite. Tectonically interleaved with felsic and mafic granodiorite	Plagioclase, clinopyroxene, biotite, and orthopyroxene. Texture of the rock appears to indicate rock was intruded under high-grade metamorphic conditions. Biotite is scattered throughout the sample and ranges 100–600 µm in length. Inclusions of opaques are common within the biotite, mostly aligned within cleavage planes. Small biotite grains appear aligned in a possible foliation, whilst the larger grains are randomly oriented throughout the rock	1989 ± 3Ma
	SO2_16A and SO2_16C Mount James Formation (394252E 7217944N)	Arkosic, matrix-supported pebble to cobble conglomerate. Most of the conglomerate clasts are composed of quartzite; however, locally derived clasts include pelitic rocks of the Moogie Metamorphics and felsic granite, and amphibolite. The Mount James Formation unconformably overlies metasedimentary rocks of the Moogie Metamorphics that have been intruded by c. 1800 Ma granite. To the south and north of this locality Mount James Formation is unconformably overlain by sedimentary rocks of the Edmund Group	Quartz, sericite, muscovite, opaques, and minor titanite and zircon. Large muscovites are of a detrital origin and up to 1 mm long. Sericite or fine-grained muscovite grains are aligned parallel to a fabric that is parallel to bedding. These grains are locally tightly crenulated	Not dated by SHRIMP; <c. 1800 Ma, >c. 1600 Ma
	CV_065 Morrissey Metamorphics (408245E 7292138N)	Metasedimentary schist	Quartz, biotite, muscovite, feldspar, zircon, titanite, and opaques. A quartz–biotite–muscovite schist in which the biotite forms very thin elongate grains and defines the foliation in the rock. All the biotite appears to be oriented in the same way, i.e. they all go to extinction at the same time. Dark pleochroic haloes in biotite have developed around zircon. Biotite ranges 40 µm–1 mm, with most grains around 100 µm long. Muscovite forms grains that are commonly up to 500 µm long, with some only 50 µm long, and are both aligned roughly in the foliation and cross-cut the foliation. However, the grains that are not aligned in the foliation sometimes appear to be broken up, or have been partially replaced by quartz and muscovite. Muscovite that replaces these larger grains are aligned in the foliation. Therefore, there are two generations of muscovite present, one pre-foliation and one syn-foliation. Quartz is mostly recrystallized and polygonal throughout	Unknown

NOTES: (a) Grid references refer to the Geocentric Datum of Australia 1994 (GDA94). Locations mentioned in the text are referenced using Map Grid Australia (MGA) coordinates, Zone 50. All locations are quoted to at least the nearest 100 m
(b) NELSON, D.R., 1999, Compilation of geochronology data, 1998: West Australian Geological Survey, Record, 1999/2

Appendix 2

Sample preparation and analytical procedures

Micas from 20 samples from rocks within the Narryer Terrane, Errabiddy Shear Zone, and Glenburgh Terrane were dated by the $^{40}Ar/^{39}Ar$ technique using infrared (IR) single-grain total fusion, IR step heating (single and multiple grains), and ultraviolet (UV) laser spots and traverses. The petrogenesis of each sample was assessed prior to sample preparation and analysis, and related to the regional structural framework detailed in (Occhipinti and Reddy, 2004; Occhipinti et al., 2004). Samples chosen for the study contained little evidence of weathering and contained suitable phases for $^{40}Ar/^{39}Ar$ dating. To test the robustness and reproducibility of the data collected, the dating was carried out in three stages using the three techniques outlined above.

Firstly, reconnaissance analyses on mineral separates from samples from throughout the region that had previously been prepared for SHRIMP U–Pb zircon dating were completed using high spatial-resolution IR laser probe single-grain total fusion analyses, or multiple-grain aliquots (usually only two grains) from individual samples. Of these samples (142900–142933 and 168944–168946), the light fractions were initially examined for the presence of pure biotite and white mica grains for $^{40}Ar/^{39}Ar$ analysis. Micas from the heavy fractions were not used, to avoid contamination due to the presence of inclusions such as opaques.

Samples 142900 and 142905 were analysed using laser-probe IR analyses on small grains. Most analyses were completed on single grains. Of these, some analyses involved total fusion of the grains, whereas some grains were only partly degassed. A few analyses involved partial or complete degassing of two to three small grains. However, there was no correlation between determined ages and the method used.

More samples were collected after the reconnaissance analyses were completed. These samples were collected from a traverse across the northern Yilgarn Craton, Errabiddy Shear Zone, and southern and central Gascoyne Complex (including the Glenburgh Terrane). The samples were analysed by two methods: high spatial-resolution laser probe IR step-heating, mostly on single grains but with a few multiple-grain analyses; and UV-laser spots and traverses on grains from a single sample.

The samples used in the IR step-heating experiments were crushed, allowing muscovite and biotite to be handpicked. Approximately 40–50 mica flakes (either white mica, or biotite, or both) were then selected from the sample. For the UV-laser analyses, one polished thick section (200 μm thickness, sample SAO_01_67) was removed from its glass slide.

All samples were cleaned in an ultrasonic bath with methanol, followed by de-ionized water. They were then dried, individually packed in aluminium foil, and loaded into an aluminium package. The data presented here were collected over two years in three different analytical batches. The biotite age standard Tinto B, with a K–Ar age of 409.25 ± 0.71 Ma (Rex and Guise, 1995) was used for each of the batches and was loaded at 5 mm intervals throughout the packages to monitor the neutron flux gradient. These packages were Cd-shielded and irradiated in the H5 position of the McMaster University Reactor (Hamilton, Canada) for 90 hours.

After irradiation, argon analyses were undertaken at the Western Australian Argon Isotope Facility. The samples were baked to 120°C overnight in an ultra-high-vacuum laser chamber, with a Kovar viewport, to remove adsorbed atmospheric argon from the samples and chamber walls. A 110 W Spectron Laser Systems continuous-wave neodymium–yttrium–aluminium–garnet laser (CW-Nd-YAG) (λ = 1064 nm), fitted with a TEM00 aperture, was used to either totally fuse grains, or step-heat grains. For step-heating experiments, the laser was rastered over individual grains. The laser was fired through a Merchantek computer-controlled X–Y–Z sample chamber stage and microscope system, fitted with a high-resolution CCD camera, 6× computer-controlled zoom, high-magnification objective lens, and two light sources for sample illumination. Before analysis, the dimensions of each grain were measured using the calibrated stage system. Mineral separate analyses involved multiple- and single-grain IR fusion and step-heating analyses. An alternative approach is to carry out multiple high spatial-resolution intragrain analyses using a laser. In these situations it is possible to identify age variations that can be directly related to microstructures within a grain or at grain boundaries. These variations indicate argon diffusion into or out of the grain. The use of the UV laser enabled heating of spots and traverses within a single grain, thus allowing the analyses of a smaller spot size and damage halo (30–90 μm spot size plus damage halo).

Gettering of the gases released by the laser heating was achieved using 3 SAES AP10 getter pumps to remove all active gases (CO_2, H_2O, H_2, N_2, O_2, and CH_4), and the remaining noble gases were equilibrated into a high-sensitivity mass spectrometer (MAP 215-50), fitted with a Balzers SEV 217 multiplier, and operated at a resolution of 600. The automated extraction and data acquisition system was computer controlled, using a LabView program. Data were corrected for mass spectrometer discrimination and nuclear interference reactions. Errors quoted on the $^{40}Ar/^{39}Ar$ ages are 1σ, and ages were calculated using the decay constant quoted by Steiger and Jäger (1977). J values are provided in the supplementary data tables (Appendix 3). Background Ar levels were monitored before and after each analysis and the mean of two blanks was used to correct each sample analysis. Sample analyses were corrected for mass spectrometer discrimination, ^{37}Ar decay, and ^{38}Ar decay.

References

OCCHIPINTI, S. A., and REDDY, S. M., 2004, Deformation in a complex crustal-scale shear zone: Errabiddy Shear Zone, Western Australia, *in* Flow Processes in Faults and Shear Zones *edited by* G. I. ALSOP, R. E. HOLDSWORTH, K. J. W. McCAFFREY, and M. HAND: Geological Society of London, Special Publications, London, p. 229–248.

OCCHIPINTI, S. A., SHEPPARD, S., PASSCHIER, C., TYLER, I. M., and NELSON, D. R., 2004. Palaeoproterozoic crustal accretion and collision in the southern Capricorn Orogen: The Glenburgh Orogeny: Precambrian Research, v. 128, p. 237–255.

REX, D. C., and GUISE, P. G., 1995, Evaluation of argon standards with special emphasis on time scale measurements, *in* Phanerozoic Time Scale *edited by* G. S. ODIN: Bulletin of Liaison and Information, IUGS Subcommission on Geochronology, p. 21–23.

STEIGER, R. H., and JÄGER, E., 1977, Subcommission on geochronology: Convention on the use of decay constants in geo- and cosmochronology: Earth and Planetary Science Letters, v. 36, p. 359–362.

Appendix 3

Supplementary data tables

J value	+/–	*Sample #*	*Type*	$^{40}Ar/^{39}Ar$	+/–	$^{38}Ar/^{39}Ar$	+/–	$^{37}Ar/^{39}Ar$	+/–	$^{36}Ar/^{39}Ar$	+/–	$^{39}Ar^{*}$ (cm^3)	+/–	*% atmospheric Ar*	*Age (Ma)*	+/–	$^{40}Ar^{*}/^{39}Ar$	+/–
Step-heating data																		
0.020541	0.000103	SO2_2a	biotite1.1	60.70	0.06	0.01646	0.00017	0.01649	0.00825	0.00170	0.00015	1.75E-11	1.36E-14	0.83	1 452	5	60.20	0.07
		SO2_2a	biotite1.2	60.06	0.07	0.01947	0.00054	0.00000	0.00000	0.00108	0.00000	5.01E-12	5.42E-15	0.53	1 445	5	59.74	0.07
		SO2_2a	biotite1.3	59.16	0.05	0.01671	0.00001	0.00000	0.00000	0.00058	0.00000	4.70E-12	2.71E-15	0.29	1 432	5	58.99	0.05
		SO2_2a	biotite1.4	59.72	0.08	0.01434	0.00057	0.04599	0.03428	0.00000	0.00000	2.36E-12	3.03E-15	0.00	1 444	8	59.72	0.35
		SO2_2a	biotite1.5	60.36	0.07	0.01567	0.00027	0.00000	0.00000	0.00159	0.00053	5.10E-12	5.59E-15	0.78	1 447	6	59.89	0.17
		SO2_2a	biotite1.6	65.38	0.54	0.02135	0.00017	0.09518	0.34318	0.00353	0.00356	3.81E-13	3.03E-15	1.60	1 519	20	64.33	1.18
		SO2_2a	biotite1.7	56.89	0.20	0.02112	0.00007	0.00000	0.00000	0.00151	0.00151	8.98E-13	3.03E-15	0.78	1 389	10	56.44	0.49
		SO2_2a	biotite1.8	57.39	0.12	0.01377	0.00106	0.00000	0.00000	0.00212	0.00000	1.28E-12	2.71E-15	1.09	1 394	5	56.76	0.12
			Weighted mean												**1 434**	**2**		
			Unweighted mean												**1 440**	**38**		
0.020541	0.000103	SO2_2a	biotite2.1	49.66	0.03	0.01705	0.00020	0.00000	0.00000	0.00175	0.00000	1.55E-11	8.13E-15	1.04	1 259	5	49.14	0.03
		SO2_2a	biotite2.2	49.36	0.08	0.01519	0.00028	0.00000	0.00000	0.00110	0.00000	4.91E-12	8.13E-15	0.66	1 257	5	49.03	0.08
		SO2_2a	biotite2.3	46.00	0.10	0.01712	0.00037	0.00000	0.00000	0.00073	0.00000	3.72E-12	8.13E-15	0.47	1 196	5	45.78	0.10
		SO2_2a	biotite2.4	47.48	0.11	0.01351	0.00059	0.00000	0.00000	0.00000		2.31E-12	5.42E-15	0.00	1 228	5	47.48	0.11
		SO2_2a	biotite2.5	48.68	0.08	0.01974	0.00163	0.17650	0.01961	0.00069	0.00073	1.85E-12	2.71E-15	0.42	1 247	6	48.48	0.23
		SO2_2a	biotite2.6	53.66	0.23	0.03261	0.00363	0.19454	0.00070	0.00000	0.00000	7.48E-13	2.71E-15	0.00	1 341	6	53.67	0.23
			Weighted mean												**1 249**	**2**		
			Unweighted mean												**1 255**	**44**		
0.02054	0.00010	SO2_07a	muscovite2.1	33.66	0.16	0.01201	0.00080	0.00000	0.00000	0.01121	0.00005	1.69E-12	8.24E-15	9.84	874	5	30.35	0.15
		SO2_07a	muscovite2.2	29.48	0.02	0.01366	0.00053	0.00000	0.00000	0.00158	0.00053	5.16E-12	2.71E-15	1.58	843	5	29.01	0.16
		SO2_07a	muscovite2.3	28.13	0.04	0.01322	0.00037	0.10204	0.01458	0.00144	0.00037	7.38E-12	8.13E-15	1.52	813	4	27.70	0.11
		SO2_07a	muscovite2.4	29.32	0.36	0.03878	0.00776	0.77008	0.15402	0.00368	0.00388	3.49E-13	0.00E+00	3.71	825	28	28.23	1.20
		SO2_07a	muscovite2.5	27.73	0.18	0.01533	0.00383	0.00000	0.00000	0.00575	0.00192	7.07E-13	0.00E+00	6.12	773	15	26.03	0.59
		SO2_07a	muscovite2.6	28.52	0.05	0.01266	0.00141	0.00000	0.00000	0.00141	0.00141	1.93E-12	2.71E-15	1.46	822	10	28.10	0.42
		SO2_07a	muscovite2.7	28.47	0.06	0.01948	0.00162	0.00000	0.06456	0.00325	0.00162	1.67E-12	2.71E-15	3.37	808	12	27.51	0.48
		SO2_07a	muscovite2.8	28.58	0.17	0.01385	0.00231	0.55098	0.00318	-0.00014	0.00000	1.17E-12	6.78E-15	-0.15	834	5	28.62	0.18
		SO2_07a	muscovite2.9	27.41	0.10	0.01357	0.00085	0.00000	0.00000	0.00170	0.00170	3.20E-12	1.16E-14	1.83	794	13	26.91	0.51
			Weighted mean												**834**	**2**		
			Unweighted mean												**834**	**21**		
0.020529	0.000103	SO2_08	biotite1.1	69.82	1.62	0.01667	0.00556	0.00000	0.00000	0.00000	0.00000	2.44E-13	3.83E-15	0.00	1 604	25	69.82	1.62
		SO2_08	biotite1.2	66.36	0.05	0.01309	0.00006	0.03030	0.02098	0.00051	0.00017	2.35E-11	1.65E-14	0.23	1 549	5	66.21	0.07
		SO2_08	biotite1.3	61.92	0.03	0.01264	0.00019	0.00000	0.00000	0.00000	0.00000	6.97E-12	2.71E-15	0.00	1 480	5	61.92	0.03
		SO2_08	biotite1.4	65.68	0.05	0.01215	0.00013	0.00517	0.01865	0.00025	0.00026	1.06E-11	8.13E-15	0.11	1 539	5	65.60	0.09
		SO2_08	biotite1.5	66.27	0.09	0.01146	0.00067	0.00000	0.00000	0.00000	0.00000	4.02E-12	5.59E-15	0.00	1 549	5	66.27	0.09
		SO2_08	biotite1.6	67.00	0.08	0.01214	0.00012	0.01475	0.00002	0.00066	0.00006	2.23E-11	2.71E-14	0.29	1 558	5	66.81	0.08
		SO2_08	biotite1.7	67.53	0.11	0.01316	0.00016	0.04497	0.00642	0.00078	0.00016	8.54E-12	1.36E-14	0.34	1 565	6	67.30	0.12
		SO2_08	biotite1.8	67.11	0.06	0.01318	0.00020	0.05580	0.00797	0.00058	0.00020	6.89E-12	5.59E-15	0.25	1 560	5	66.94	0.08
		SO2_08	biotite1.9	68.84	0.31	0.01326	0.00148	0.02988	0.02988	0.00220	0.00074	1.84E-12	8.24E-15	0.95	1 579	8	68.19	0.38
		SO2_08	biotite1.10	69.12	0.06	0.01223	0.00076	0.00000	0.00000	0.00115	0.00038	3.55E-12	3.03E-15	0.49	1 588	6	68.78	0.13
		SO2_08	biotite1.11	60.34	0.19	0.01061	0.00133	0.16146	0.05382	0.00000	0.00000	2.04E-12	6.06E-15	0.00	1 457	7	60.55	0.27
		SO2_08	biotite1.12	60.82	0.16	0.01387	0.00082	0.00000	0.00000	0.00204	0.00041	3.32E-12	8.57E-15	0.99	1 452	6	60.22	0.20
		SO2_08	biotite1.13	63.02	0.25	0.02632	0.00010	0.00000	0.00000	0.00376	0.00001	7.21E-13	2.71E-15	1.76	1 480	6	61.90	0.24
			Weighted mean												**1 532**	**2**		
			Unweighted mean												**1 535**	**49**		

Appendix 3 (continued)

J value	*+/–*	*Sample #*	*Type*	*$^{40}Ar/^{39}Ar$*	*+/–*	*$^{38}Ar/^{39}Ar$*	*+/–*	*$^{37}Ar/^{39}Ar$*	*+/–*	*$^{36}Ar/^{39}Ar$*	*+/–*	*$^{39}Ar^*$ (cm^3)*	*+/–*	*% atmospheric Ar*	*Age (Ma)*	*+/–*	*$^{40}Ar^*/^{39}Ar$*	*+/–*
0.02053	0.000103	SAO_01_08	muscovite1.1	31.01	0.03	0.01302	0.00019	0.01043	0.01043	0.00141	0.00025	1.63E-11	1.08E-14	1.34	879	4	30.60	0.08
		SAO_01_08	muscovite1.2	30.59	0.12	0.01211	0.00045	0.03384	0.05641	0.00223	0.00135	3.02E-12	8.13E-15	2.16	864	10	29.93	0.41
		SAO_01_08	muscovite1.3	30.54	0.02	0.01158	0.00017	0.01404	0.00001	0.00055	0.00009	2.91E-11	1.38E-14	0.54	874	4	30.37	0.03
		SAO_01_08	muscovite1.4	30.37	0.02	0.01213	0.00015	0.01979	0.00001	0.00019	0.00010	2.76E-11	8.57E-15	0.19	873	4	30.32	0.03
		SAO_01_08	muscovite1.5	30.25	0.02	0.01239	0.00011	0.02945	0.00393	0.00073	0.00004	3.48E-11	2.71E-14	0.72	867	4	30.04	0.03
		SAO_01_08	muscovite1.6	30.33	0.02	0.01262	0.00006	0.03797	0.00447	0.00002	0.00003	4.32E-11	2.17E-14	0.02	873	3	30.33	0.02
		SAO_01_08	muscovite1.7	30.02	0.04	0.01420	0.00014	0.00000	0.00000	-0.00014	-0.00014	1.00E-11	1.41E-14	0.00	867	4	30.06	0.06
		SAO_01_08	muscovite1.8	29.88	0.07	0.01278	0.00035	0.00000	0.00000	0.00037	0.00035	3.92E-12	9.09E-15	0.36	860	4	29.77	0.13
		SAO_01_08	muscovite1.9	31.00	0.07	0.01305	0.00037	0.02822	0.04704	0.00148	0.00000	3.64E-12	8.24E-15	1.41	879	4	30.56	0.07
		SAO_01_08	muscovite1.10	30.09	0.02	0.01354	0.00029	0.02182	0.03917	-0.00116	0.00000	4.70E-12	3.03E-15	0.00	876	4	30.44	0.02
		SAO_01_08	muscovite1.11	30.68	0.03	0.01155	0.00037	0.10351	0.00941	0.00146	0.00074	3.64E-12	3.03E-15	1.41	872	6	30.25	0.22
		SAO_01_08	muscovite1.12	30.51	0.06	0.01333	0.00023	0.05140	0.00571	-0.00047	-0.00045	6.00E-12	1.09E-14	0.00	881	5	30.65	0.15
			Weighted mean												**873**	**1**		
			Unweighted mean												**872**	**6**		
0.020531	0.000103	SO2_14	muscovite1.1	33.46	0.02	0.013117	0.000238	0.02941	0.00735	0.00024	0.00008	1.61E-11	8.24E-15	0.22	942	4	33.39	0.03
		SO2_14	muscovite1.2	30.69	0.11	0.013611	0.000336	0.08710	0.01452	0.00014	0.00017	8.16E-12	2.98E-14	0.14	881	4	30.65	0.12
		SO2_14	muscovite1.3	30.89	0.07	0.012756	0.000387	0.00000	0.00000	0.00000	0.00000	3.51E-12	5.59E-15	0.00	886	4	30.89	0.07
		SO2_14	muscovite1.4	31.37	0.05	0.01144	0.000294	0.01284	0.01284	0.00000	0.00000	4.62E-12	5.59E-15	0.00	897	4	31.37	0.05
		SO2_14	muscovite1.5	30.19	0.14	0.013334	0.001027	0.08988	0.17975	0.00305	0.00103	1.32E-12	5.59E-15	2.99	849	8	29.28	0.33
		SO2_14	muscovite1.6	31.52	0.19	0.01275	0.004073	0.00000	0.00000	0.00546	0.00407	7.44E-13	3.03E-15	5.12	864	28	29.90	1.22
		SO2_14	muscovite1.7	30.96	0.20	0.019499	0.002788	0.00000	0.00000	0.01114	0.00007	4.86E-13	3.03E-15	10.63	812	5	27.67	0.18
		SO2_14	muscovite1.8	31.48	0.27	0.018051	0.003613	0.00000	0.00000	0.01444	0.00012	3.75E-13	3.03E-15	13.56	801	7	27.21	0.24
			Weighted mean												**884**	**2**		
			Unweighted mean												**866**	**43**		
0.020531	0.000103	SO2_14	muscovite2.1	32.28	0.03	0.012826	8.03E-05	0.00000	0.00000	0.00040	0.00008	1.70E-11	1.36E-14	0.36	915	4	32.16	0.04
		SO2_14	muscovite2.2	31.11	0.04	0.010849	0.000265	0.00000	0.00000	0.00000	0.00000	5.12E-12	5.59E-15	0.00	891	4	31.11	0.04
		SO2_14	muscovite2.3	31.61	0.22	0.005911	0.000986	0.00000	0.00000	0.00000	0.00000	2.75E-12	1.92E-14	0.00	902	6	31.61	0.22
		SO2_14	muscovite2.4	32.33	0.20	0.010677	0.001188	0.18249	0.07822	0.00648	0.00178	2.28E-12	1.38E-14	5.92	875	13	30.42	0.56
			Weighted mean												**902**	**2**		
			Unweighted mean												**896**	**15**		
0.020537	0.000103	SAO_14	biotite1.1	23.31	0.04	0.01432	0.00002	0.00000	0.00000	0.00862	0.00036	1.12E-11	1.94E-14	10.92	641	4	20.77	0.11
		SAO_14	biotite1.2	23.75	0.01	0.01377	0.00003	0.02288	0.00237	0.00464	0.00009	7.97E-11	4.36E-14	5.77	682	3	22.38	0.03
		SAO_14	biotite1.3	23.96	0.04	0.01211	0.00017	0.00000	0.00000	0.00382	0.00017	8.17E-12	1.09E-14	4.71	694	3	22.84	0.06
		SAO_14	biotite1.4	24.03	0.02	0.01164	0.00012	0.00000	0.00000	0.00380	0.00012	1.11E-11	5.59E-15	4.67	696	3	22.91	0.04
		SAO_14	biotite1.5	23.69	0.02	0.01252	0.00015	0.02516	0.00002	0.00412	0.00007	2.00E-11	1.65E-14	5.14	685	3	22.47	0.03
		SAO_14	biotite1.6	22.85	0.02	0.01226	0.00012	0.00000	0.00000	0.00450	0.00012	2.62E-11	1.92E-14	5.82	660	3	21.53	0.04
		SAO_14	biotite1.7	21.50	0.02	0.01332	0.00014	0.00000	0.00000	0.00415	0.00014	9.46E-12	9.09E-15	5.71	628	3	20.27	0.05
		SAO_14	biotite1.8	21.52	0.03	0.01210	0.00017	0.00000	0.00000	0.00434	0.00008	1.78E-11	2.74E-14	5.96	627	3	20.24	0.04
		SAO_14	biotite1.9	23.65	0.15	0.00849	0.00170	0.00000	0.00000	0.00509	0.00170	7.98E-13	4.89E-15	6.36	676	14	22.14	0.52
		SAO_14	biotite1.10	22.23	0.05	0.01347	0.00035	0.00000	0.00000	0.00587	0.00035	3.92E-12	9.09E-15	7.80	634	4	20.50	0.11
			Weighted mean												**662**	**1**		
			Unweighted mean												**662**	**26**		
0.020536	0.000103	SO2_10	biotite1.1	40.01	0.03	0.02363	0.00033	0.00000	0.00000	0.05427	0.00033	1.16E-11	8.13E-15	40.08	722	4	23.97	0.10
		SO2_10	biotite1.2	32.57	0.03	0.01463	0.00031	0.10774	0.03591	0.00589	0.00031	8.71E-12	8.13E-15	5.34	885	4	30.83	0.10
		SO2_10	biotite1.3	30.51	0.02	0.01284	0.00037	0.04319	0.02036	0.00311	0.00012	1.09E-11	8.24E-15	3.01	857	4	29.59	0.04
		SO2_10	biotite1.4	30.95	0.11	0.01703	0.00243	0.00000	0.00000	0.00081	0.00081	1.67E-12	5.59E-15	0.77	882	7	30.71	0.26
		SO2_10	biotite1.5	30.20	0.46	0.01875	0.00313	0.00000	0.00000	0.00000	0.00000	8.67E-13	1.12E-14	0.00	871	11	30.20	0.46
			Weighted mean												**828**	**2**		
			Unweighted mean												**843**	**61**		

Appendix 3 (continued)

J value	+/–	Sample #	Type	$^{40}Ar/^{39}Ar$	+/–	$^{38}Ar/^{39}Ar$	+/–	$^{37}Ar/^{39}Ar$	+/–	$^{36}Ar/^{39}Ar$	+/–	$^{39}Ar^*$ (cm^3)	+/–	% atmospheric Ar	Age (Ma)	+/–	$^{40}Ar^*/^{39}Ar$	+/–
0.020536	0.000103	SO2_10	biotite2.1	30.39	0.02	0.01775	0.00009	0.03489	0.01779	0.02459	0.00019	4.49E-11	2.67E-14	23.91	701	3	23.12	0.06
		SO2_10	biotite2.2	26.95	0.02	0.01410	0.00013	0.03301	0.00934	0.00570	0.00011	2.37E-11	1.71E-14	6.25	754	3	25.26	0.04
		SO2_10	biotite2.3	29.26	0.02	0.01323	0.00007	0.01900	0.00380	0.00407	0.00007	4.13E-11	2.76E-14	4.11	821	3	28.06	0.03
		SO2_10	biotite2.4	28.97	0.03	0.01265	0.00001	0.00000	0.00000	0.00285	0.00011	2.57E-11	2.21E-14	2.90	822	3	28.12	0.04
		SO2_10	biotite2.5	28.16	0.04	0.01357	0.00031	0.00000	0.00000	0.00308	0.00031	8.79E-12	9.09E-15	3.23	802	4	27.25	0.10
		SO2_10	biotite2.6	28.54	0.03	0.01201	0.00013	0.00000	0.00000	0.00310	0.00026	1.05E-11	1.09E-14	3.21	811	4	27.62	0.08
		SO2_10	biotite2.7	30.01	0.02	0.01329	0.00033	0.11850	0.05354	0.00318	0.00029	9.28E-12	5.59E-15	3.13	844	4	29.07	0.09
			Weighted mean												**789**	**1**		
			Unweighted mean												**794**	**46**		
0.020539	0.000103	SO2_16A	muscovite1.1	57.33	0.95	0.00693	0.00693	7.62928	0.85590	0.02578	0.00040	1.96E-13	3.03E-15	13.29	1 269	16	49.71	0.84
		SO2_16A	muscovite1.2	29.66	0.04	0.01085	0.00047	0.00000	0.00000	0.00378	0.00000	2.87E-12	3.03E-15	3.76	832	3	28.54	0.04
		SO2_16A	muscovite1.3	31.79	0.01	0.01267	0.00008	0.04446	0.00699	0.00031	0.00000	1.23E-10	4.96E-14	0.29	905	4	31.70	0.01
		SO2_16A	muscovite1.4	31.17	0.02	0.01297	0.00017	0.00000	0.00000	0.00054	0.00008	1.74E-11	8.24E-15	0.52	889	4	31.01	0.03
		SO2_16A	muscovite1.5	32.60	0.23	0.01454	0.00162	0.00000	0.00000	0.00485	0.00162	8.39E-13	5.59E-15	4.39	893	12	31.17	0.53
		SO2_16A	muscovite1.6	31.12	0.04	0.01322	0.00001	0.00000	0.00000	0.00055	0.00000	4.92E-12	5.42E-15	0.52	888	4	30.96	0.04
		SO2_16A	muscovite1.7	31.61	0.01	0.01238	0.00001	0.03125	0.00313	0.00014	0.00000	5.32E-11	2.17E-14	0.14	902	4	31.57	0.01
			Weighted mean												**886**	**2**		
			Unweighted mean												**940**	**136**		
0.020539	0.000103	SO2_16A	muscovite2.1	31.96	0.05	0.01189	0.00002	0.00000	0.00000	0.00066	0.00000	4.10E-12	5.42E-15	0.61	906	4	31.76	0.04
		SO2_16A	muscovite2.2	32.56	0.02	0.01073	0.00001	0.06273	0.00003	-0.00002	0.00000	5.31E-12	2.71E-15	0.00	924	4	32.57	0.02
		SO2_16A	muscovite2.3	33.00	0.02	0.01216	0.00012	0.10458	0.00747	0.00009	0.00000	2.23E-11	1.36E-14	0.08	933	4	32.97	0.02
		SO2_16A	muscovite2.4	32.72	0.01	0.01268	0.00000	0.02751	0.00917	0.00029	0.00000	1.82E-11	5.42E-15	0.26	925	4	32.63	0.01
		SO2_16A	muscovite2.5	33.18	0.02	0.01245	0.00016	0.09571	0.00957	0.00029	0.00000	1.74E-11	8.13E-15	0.26	936	4	33.10	0.02
		SO2_16A	muscovite2.6	45.12	0.12	0.01373	0.00004	0.52787	0.07466	0.00158	0.00000	3.16E-12	8.13E-15	1.04	1 174	5	44.66	0.12
			Weighted mean												**950**	**2**		
			Unweighted mean												**966**	**93**		
0.020538	0.000103	SO2_16C	muscovite1.1	49.53	0.38	0.01273	0.00010	0.42142	0.08435	0.01516	0.00255	1.06E-12	8.13E-15	9.05	1 182	17	45.05	0.83
		SO2_16C	muscovite1.2	45.46	0.07	0.01354	0.00035	0.03093	0.07218	0.01042	0.00016	8.71E-12	1.36E-14	6.77	1 130	5	42.38	0.08
		SO2_16C	muscovite1.3	41.20	0.05	0.01266	0.00020	0.00000	0.00000	0.00171	0.00009	1.51E-11	1.90E-14	1.22	1 096	4	40.70	0.06
		SO2_16C	muscovite1.4	45.02	0.04	0.01375	0.00021	0.01837	0.01837	0.00120	0.00009	1.47E-11	1.09E-14	0.78	1 174	4	44.67	0.04
		SO2_16C	muscovite1.5	36.97	0.01	0.01262	0.00010	0.03186	0.00869	0.00152	0.00010	3.10E-11	1.09E-14	1.21	1 010	4	36.52	0.03
		SO2_16C	muscovite1.6	36.76	0.01	0.01261	0.00016	0.04523	0.00754	0.00061	0.00017	2.39E-11	8.13E-15	0.49	1 011	4	36.58	0.05
		SO2_16C	muscovite1.7	32.15	0.03	0.01187	0.00019	0.07630	0.01272	0.00008	0.00029	1.42E-11	1.36E-14	0.07	914	4	32.12	0.09
		SO2_16C	muscovite1.8	38.55	0.04	0.01188	0.00070	0.00000	0.00000	0.00000	0.00000	3.88E-12	3.03E-15	0.00	1 052	4	38.55	0.04
		SO2_16C	muscovite1.9	39.90	0.04	0.01195	0.00048	0.00000	0.00000	0.00072	0.00072	5.67E-12	5.59E-15	0.53	1 075	6	39.68	0.22
		SO2_16C	muscovite1.10	37.55	0.04	0.01174	0.00015	0.00000	0.00000	0.00085	0.00008	1.75E-11	1.65E-14	0.67	1 026	4	37.30	0.04
		SO2_16C	muscovite1.11	35.22	0.04	0.01128	0.00001	0.01975	0.00658	0.00089	0.00010	1.37E-11	1.38E-14	0.74	976	4	34.96	0.05
		SO2_16C	muscovite1.12	40.40	0.03	0.01247	0.00013	0.03890	0.00432	0.00031	0.00006	2.09E-11	1.65E-14	0.23	1 088	4	40.31	0.04
			Weighted mean												**1045**	**1**		
			Unweighted mean												**1061**	**76**		
0.020529	0.000103	CV_065	biotite1.1	21.60	0.07	0.01895	0.00200	0.21094	0.14967	0.01971	0.00141	1.92E-12	4.89E-15	26.97	506	12	15.77211	0.42
		CV_065	biotite1.2	29.37	0.01	0.01287	0.00014	0.02866	0.01209	0.00657	0.00014	1.98E-11	9.09E-15	6.61	806	3	27.43007	0.04
		CV_065	biotite1.3	30.14	0.01	0.01202	0.00006	0.01733	0.00341	0.00162	0.00012	2.34E-11	9.09E-15	1.59	858	4	29.66152	0.04
		CV_065	biotite1.4	29.78	0.09	0.01359	0.00046	0.19019	0.02674	0.00086	0.00091	2.99E-12	9.09E-15	0.85	855	7	29.5246	0.28
		CV_065	biotite1.5	30.66	0.03	0.01241	0.00034	0.00000	0.00000	0.00000	0.00000	8.90E-12	9.09E-15	0.00	881	4	30.66377	0.10
			Weighted mean												**836**	**2**		
			Unweighted mean												**781**	**140**		

Appendix 3 (continued)

J value	+/–	*Sample #*	*Type*	$^{40}Ar/^{39}Ar$	+/–	$^{38}Ar/^{39}Ar$	+/–	$^{37}Ar/^{39}Ar$	+/–	$^{36}Ar/^{39}Ar$	+/–	$^{39}Ar^*$ (cm^3)	+/–	*% atmospheric Ar*	*Age (Ma)*	+/–	$^{40}Ar^*/^{39}Ar$	+/–
0.020529	0.000103	CV_065	biotite2.1	25.84	0.03	0.01661	0.00030	0.00000	0.00000	0.01690	0.00041	1.00E-11	1.16E-14	19.32	643	4	20.84415	0.12
		CV_065	biotite2.2	30.15	0.03	0.01419	0.00007	0.05732	0.01047	0.00562	0.00012	4.11E-11	3.82E-14	5.51	831	3	28.49296	0.04
		CV_065	biotite2.3	31.13	0.01	0.01284	0.00015	0.00000	0.00000	0.00026	0.00000	2.06E-11	6.78E-15	0.25	890	4	31.05528	0.01
		CV_065	biotite2.4	31.74	0.03	0.01227	0.00004	0.05313	0.00227	0.00037	0.00000	3.52E-11	2.74E-14	0.35	903	4	31.62955	0.03
		CV_065	biotite2.5	31.21	0.08	0.01257	0.00021	0.00000	0.00000	0.00083	0.00041	6.57E-12	1.63E-14	0.78	888	5	30.97081	0.14
		CV_065	biotite2.6	31.45	0.06	0.01223	0.00025	0.00000	0.00000	0.00000	0.00000	1.22E-11	2.17E-14	0.00	899	4	31.45229	0.11
		CV_065	biotite2.7	31.47	0.03	0.01274	0.00001	0.00000	0.00000	0.00071	0.00024	5.71E-12	6.06E-15	0.67	894	4	31.25988	0.08
			Weighted mean												**852**	**2**		
			Unweighted mean												**850**	**87**		
0.020528	0.000103	CV_065	muscovite1.1	39.50	0.86	0.00000	0.00000	0.00000	0.00000	0.00000	0.00000	1.44E-13	3.03E-15	0.00	1 071	60	39.50445	2.92
		CV_065	muscovite1.2	30.29	0.06	0.01389	0.00016	0.06874	0.03382	0.00079	0.00016	8.36E-12	1.63E-14	0.77	867	4	30.05435	0.08
		CV_065	muscovite1.3	28.58	0.03	0.01259	0.00009	0.00000	0.00000	0.00009	0.00009	1.57E-11	1.63E-14	0.09	832	3	28.55888	0.04
		CV_065	muscovite1.4	27.78	0.08	0.01175	0.00127	0.53690	0.00136	0.00000	0.00000	1.07E-12	2.71E-15	0.00	815	10	27.82411	0.38
		CV_065	muscovite1.5	28.37	0.03	0.01165	0.00071	0.03746	0.03686	0.00034	0.00106	3.84E-12	3.03E-15	0.36	826	8	28.26897	0.31
		CV_065	muscovite1.6	27.99	0.14	0.00992	0.00005	0.08505	0.08368	0.00000	0.00000	1.69E-12	8.24E-15	-0.02	819	17	27.99764	0.72
		CV_065	muscovite1.7	28.80	0.06	0.01238	0.00080	0.16994	0.33443	0.00076	0.00080	1.70E-12	3.03E-15	0.78	833	7	28.57554	0.24
		CV_065	muscovite1.8	28.02	0.09	0.01383	0.00122	0.00000	0.00000	0.00365	0.00122	1.11E-12	3.03E-15	3.85	794	9	26.93564	0.37
		CV_065	muscovite1.9	29.90	0.35	0.03337	0.00038	0.00000	0.00000	0.01616	0.00018	3.35E-13	3.83E-15	15.97	750	8	25.1222	0.30
			Weighted mean												**834**	**2**		
			Unweighted mean												**845**	**85**		

J value	+/–	*Sample #*	*Type*	$^{40}Ar/^{39}Ar$	+/–	$^{38}Ar/^{39}Ar$	+/–	$^{37}Ar/^{39}Ar$	+/–	$^{36}Ar/^{39}Ar$	+/–	$^{39}Ar^*$ (cm^3)	+/–	*% atmospheric Ar*	*Age (Ma)*	+/–	$^{40}Ar^*/^{39}Ar$	+/–
Total-fusion data																		
0.02031	0.000102	142900	muscovite1	76.56368404	0.05	0.01	0.00010	0.00761	0.00898	0.00068	0.00005	0.00000	2.19E-12	2.62E-01	1 690.01	6	76	0.05
		142900	muscovite2	53.07598869	0.13	0.01	0.00003	0.03674	0.02164	0.00014	0.00015	0.00000	2.61E-13	7.92E-02	1 319.22	5	53	0.14
		142900	muscovite3	52.56518243	0.11	0.01	0.00002	0.00000	0.00000	0.00106	0.00000	0.00000	2.23E-14	5.97E-01	1 305.37	5	52	0.11
		142900	muscovite4	37.08587674	0.02	0.01	0.00010	0.00188	0.00666	0.00003	0.00010	0.00000	5.02E-12	2.72E-02	1 013.08	4	37	0.04
		142900	muscovite4	40.02277086	0.03	0.01	0.00023	0.01698	0.00556	0.00052	0.00010	0.00000	5.56E-13	3.80E-01	1 070.59	4	40	0.04
		142900	muscovite6	76.85554026	1.07	0.01	0.00014	0.09764	0.00737	0.00066	0.00014	0.00000	3.16E-13	2.55E-01	1 694.26	16	77	1.07
		142900	muscovite7	56.21354498	0.03	0.01	0.00001	0.00000	0.04065	0.00076	0.00000	0.00000	4.17E-14	3.99E-01	1 370.63	5	56	0.03
		142900	muscovite8	31.38645589	0.02	0.01	0.00001	0.00000	0.02009	0.00133	0.00000	0.00000	3.41E-13	1.25E+00	881.24	4	31	0.02
		142900	muscovite9	61.34481932	0.32	0.02	0.00009	0.23546	0.04625	0.01356	0.00007	0.00000	3.61E-14	6.53E+00	1 393.63	7	57	0.30
0.02034	0.000102	142905	biotite1	70.09983791	0.06	0.01	0.00040	0.04476	0.03107	0.00362	0.00000	0.00000	1.47E-13	1.53E+00	1 582.47	5	69	0.06
		142905	biotite2	72.09693946	0.11	0.01	0.00050	0.22260	0.02732	0.00446	0.00001	0.00000	9.54E-14	1.83E+00	1 608.98	6	71	0.11
		142905	biotite3	72.35452429	0.19	0.02	0.00004	0.57878	0.14205	0.00000	0.00000	0.00000	4.26E-15	0.00E+00	1 633.18	6	72	0.19
		142905	biotite4	72.54813279	0.08	0.02	0.00022	0.07372	0.01706	0.00397	0.00000	0.00000	4.89E-13	1.62E+00	1 617.94	5	71	0.08
		142905	biotite5	74.9319682	0.15	0.01	0.00003	0.00000	0.00000	0.00534	0.00001	0.00000	5.52E-14	2.11E+00	1 647.29	6	73	0.15
		142905	biotite6	72.43675729	1.47	0.01	0.00023	0.00000	0.00000	0.00523	0.00010	0.00000	8.97E-14	2.14E+00	1 610.66	22	71	1.44
		142905	biotite7	74.75799188	0.03	0.01	0.00001	0.00000	0.00000	0.00479	0.00066	0.00000	6.80E-13	1.89E+00	1 647.13	6	73	0.20
		142905	biotite8	80.28987835	0.15	0.02	0.00078	0.12997	0.09510	0.01361	0.00273	0.00000	3.99E-14	5.01E+00	1 689.73	13	76	0.82
		142905	biotite9	73.58278899	0.09	0.02	0.00107	0.29857	0.05862	0.01119	0.00161	0.00000	2.10E-14	4.50E+00	1 601.39	9	70	0.48
		142905	biotite10	74.71350702	0.05	0.02	0.00038	0.00000	0.00000	0.00705	0.00040	0.00000	3.41E-13	2.79E+00	1 636.64	6	73	0.13
		142905	biotite11	70.84476609	0.05	0.01	0.00140	0.07785	0.07643	0.00068	0.00210	0.00000	1.23E-14	2.83E-01	1 606.96	11	71	0.62
			Weighted mean												**1 622.95**	**2**		
			Unweighted mean												**1 625.67**	**28**		

Appendix 3 (continued)

J value	+/–	Sample #	Type	$^{40}Ar/^{39}Ar$	+/–	$^{38}Ar/^{39}Ar$	+/–	$^{37}Ar/^{39}Ar$	+/–	$^{36}Ar/^{39}Ar$	+/–	$^{39}Ar^*$ (cm^3)	+/–	% atmospheric Ar	Age (Ma)	+/–	$^{40}Ar^*/^{39}Ar$	+/–
0.02045	0.000102	142907	biotite2	38.06157187	0.07	0.02	0.00047	0.00000	–	0.01805	0.00003	0.00000	9.90E-15	1.40E+01	924.40	4	33	0.06
		142907	biotite3	39.93320638	0.08	0.01	0.00066	0.00000	–	0.01353	0.00059	0.00000	7.59E-15	1.00E+01	993.96	6	36	0.19
		142907	biotite4	36.56037259	0.03	0.02	0.00023	0.00000	–	0.01352	0.00018	0.00000	1.22E-14	1.09E+01	920.84	4	33	0.06
		142907	biotite6	34.51839653	0.47	0.01	0.00025	0.02188	0.01862	0.01082	0.00026	0.00000	4.22E-13	9.27E+00	893.03	10	31	0.43
		142907	biotite7	34.13083513	0.16	0.01	0.00035	0.07745	0.08986	0.00606	0.00039	0.00000	8.65E-15	5.24E+00	915.85	6	32	0.20
		142907	biotite8	34.42609969	0.03	0.01	0.00025	0.00000	–	0.00674	0.00037	0.00000	7.20E-15	5.79E+00	917.91	4	32	0.11
		142907	biotite9	34.51526397	0.04	0.01	0.00001	0.00000	–	0.00578	0.00017	0.00000	2.40E-14	4.95E+00	926.14	4	33	0.06
		142907	biotite10	33.6090752	0.02	0.01	0.00013	0.01617	0.00001	0.00386	0.00020	0.00000	9.67E-15	3.39E+00	918.68	4	32	0.06
		142907	biotite11	33.63626002	0.03	0.01	0.00042	0.52312	0.00046	0.00220	0.00064	0.00000	4.95E-15	1.93E+00	930.14	6	33	0.19
		142907	biotite12	33.77422245	0.08	0.01	0.00003	0.00000	–	0.00168	0.00000	0.00000	7.20E-15	1.47E+00	936.52	4	33	0.08
		142907	biotite14	34.04856073	0.03	0.01	0.00017	0.00000	–	0.00447	0.00034	0.00000	4.95E-15	3.88E+00	924.41	4	33	0.10
		142907	biotite15	34.50466101	0.01	0.01	0.00011	0.00000	–	0.00641	0.00010	0.00000	9.67E-15	5.49E+00	921.80	4	33	0.03
			Weighted mean												**926.95**	**1**		
			Unweighted mean												**926.97**	**23**		
0.02046	0.000102	142907	muscovite1	34.55993565	0.02	0.01	0.00029	0.11285	0.02216	0.00061	0.00013	0.00000	4.80E-15	5.23E-01	960.91	4	34	0.04
		142907	muscovite2	30.81079684	0.01	0.01	0.00011	0.00000	–	0.00069	0.00000	0.00000	3.39E-15	6.61E-01	877.26	3	31	0.01
		142907	muscovite3	30.48447517	0.02	0.01	0.00011	0.00668	0.00656	0.00000	–	0.00000	7.59E-15	0.00E+00	876.01	4	31	0.02
		142907	muscovite4	29.70106906	0.04	0.01	0.00001	0.00000	–	0.00151	0.00049	0.00000	2.68E-15	1.50E+00	846.29	5	29	0.15
		142907	muscovite5	25.33116504	0.02	0.01	0.00005	0.00000	–	0.00030	0.00003	0.00000	3.36E-14	3.46E-01	751.22	3	25	0.02
		142907	muscovite6	31.18783455	0.01	0.01	0.00010	0.01058	0.03289	0.00081	0.00009	0.00000	4.95E-15	7.64E-01	885.02	4	31	0.03
		142907	muscovite7	24.70029812	0.03	0.01	0.00011	0.00000	–	0.00112	0.00011	0.00000	1.21E-14	1.34E+00	729.80	3	24	0.04
		142907	muscovite8	31.83264795	0.06	0.01	0.00017	0.00000	–	0.00062	0.00032	0.00000	1.46E-14	5.71E-01	900.80	4	32	0.11
		142907	muscovite9	28.69633077	0.03	0.01	0.00015	0.27058	0.03506	0.00108	0.00030	0.00000	7.59E-15	1.11E+00	825.93	4	28	0.09
		142907	muscovite10	24.28691277	0.01	0.01	0.00008	0.00830	0.00860	0.00049	0.00007	0.00000	8.05E-15	5.97E-01	724.20	3	24	0.03
		142907	muscovite11	27.43974511	0.02	0.01	0.00009	0.00945	0.00979	0.00000	–	0.00000	1.25E-14	0.00E+00	804.47	3	27	0.03
		142907	muscovite12	30.30799029	0.02	0.01	0.00016	0.01759	0.00001	0.00052	0.00008	0.00000	1.20E-14	5.04E-01	866.97	4	30	0.03
			Weighted mean												**826.01**	**1**		
			Unweighted mean												**837.41**	**70**		
0.0204	0.000102	142910	biotite1	36.56141573	0.29	0.01	0.00034	0.00000	0.00000	0.00594	0.00071	0.00000	1.68E-14	4.80E+00	967.94	9	35	0.36
		142910	biotite2	35.6331719	0.10	0.01	0.00011	0.00186	0.00409	0.00205	0.00024	0.00000	1.44E-14	1.70E+00	972.70	5	35	0.12
		142910	biotite3	36.05643455	0.04	0.01	0.00037	0.00000	0.00000	0.00614	0.00010	0.00000	9.60E-15	5.03E+00	955.79	4	34	0.05
		142910	biotite4	34.68703948	0.10	0.01	0.00070	0.00000	0.00000	0.00259	0.00052	0.00000	1.44E-14	2.21E+00	948.80	5	34	0.18
		142910	biotite5	35.1192656	0.03	0.01	0.00022	0.03710	0.01163	0.00268	0.00022	0.00000	8.05E-15	2.25E+00	957.62	4	34	0.07
		142910	biotite6	35.95823283	0.05	0.01	0.00002	0.00000	0.00000	0.00143	0.00069	0.00000	4.33E-15	1.18E+00	983.55	6	36	0.21
		142910	biotite7	35.33441267	0.01	0.01	0.00014	0.00000	0.00000	0.00196	0.00006	0.00000	3.39E-15	1.64E+00	966.87	4	35	0.02
		142910	biotite8	35.05461036	0.03	0.01	0.00006	0.00000	0.00000	0.00288	0.00006	0.00000	1.70E-14	2.43E+00	954.94	4	34	0.04
		142910	biotite9	37.0753716	0.03	0.01	0.00001	0.00000	0.00000	0.00945	0.00019	0.00000	7.59E-15	7.53E+00	956.65	4	34	0.06
		142910	biotite10	36.00770759	0.02	0.01	0.00013	0.00000	0.00000	0.00570	0.00018	0.00000	7.59E-15	4.68E+00	957.51	4	34	0.06
		142910	biotite11	37.28639649	0.07	0.02	0.00056	0.00000	0.00000	0.01149	0.00028	0.00000	4.95E-15	9.11E+00	948.14	4	34	0.11
		142910	biotite12	35.39374414	0.06	0.01	0.00002	0.00000	0.00000	0.00145	0.00028	0.00000	4.95E-15	1.21E+00	971.37	4	35	0.11
			Weighted mean												**960.52**	**1**		
			Unweighted mean												**961.82**	**10**		
0.02041	0.000102	142910	musc1	32.18478492	1.80	0.01	0.00111	0.03225	0.00265	0.00207	0.00057	0.00000	2.99E-12	1.90E+00	897.34	40	32	1.78
		142910	musc2	32.14949415	0.03	0.01	0.00054	0.07610	0.01856	0.00000	–	0.00000	7.20E-15	0.00E+00	911.89	4	32	0.08
		142910	musc3	32.05923474	0.02	0.01	0.00048	0.16760	0.03291	0.00139	0.00048	0.00000	2.40E-15	1.28E+00	899.03	5	32	0.14
		142910	musc4	32.03407635	0.04	0.01	0.00005	0.02583	0.01570	0.00114	0.00014	0.00000	6.24E-14	1.05E+00	900.12	4	32	0.06
		142910	musc5	33.64386474	0.31	0.01	0.00015	0.25123	0.18617	0.00348	0.00162	0.00000	7.22E-15	3.06E+00	920.52	13	33	0.57
		142910	musc6	34.65019597	0.02	0.01	0.00019	0.00000	0.00000	0.00093	0.00025	0.00000	9.67E-15	7.97E-01	958.98	4	34	0.08
		142910	musc7	32.26234743	0.02	0.01	0.00005	0.00000	0.00000	0.00127	0.00015	0.00000	1.44E-14	1.16E+00	904.37	4	32	0.05

Appendix 3 (continued)

J value	*+/–*	*Sample #*	*Type*	$^{40}Ar/^{39}Ar$	*+/–*	$^{38}Ar/^{39}Ar$	*+/–*	$^{37}Ar/^{39}Ar$	*+/–*	$^{36}Ar/^{39}Ar$	*+/–*	$^{39}Ar^{*}$ *(cm³)*	*+/–*	*% atmospheric Ar*	*Age (Ma)*	*+/–*	$^{40}Ar^{*}/^{39}Ar$	*+/–*
		142910	musc8	31.99187663	0.05	0.01	0.00002	0.00704	0.02072	0.00279	0.00040	0.00000	9.67E-15	2.58E+00	888.20	5	31	0.13
		142910	musc9	32.16659573	0.01	0.01	0.00008	0.00000	0.00000	0.00076	0.00008	0.00000	9.67E-15	7.00E-01	905.55	4	32	0.03
		142910	musc10	31.99196128	0.01	0.01	0.00008	0.01228	0.00300	0.00096	0.00012	0.00000	7.59E-15	8.90E-01	900.32	4	32	0.04
		142910	musc11	35.75450535	0.05	0.02	0.00054	0.01940	0.01904	0.00703	0.00054	0.00000	2.40E-15	5.81E+00	943.83	5	34	0.17
		142910	musc12	33.34017084	0.04	0.01	0.00020	0.01447	0.00001	0.00201	0.00020	0.00000	9.60E-15	1.78E+00	923.38	4	33	0.07
			Weighted mean												**912.46**	**1**		
			Unweighted mean												**912.79**	**20**		
0.0203	0.000102	142911	biotite1	36.15731644	0.05	0.02	0.00076	0.00464	0.00455	0.00987	0.00076	0.00000	7.30E-15	8.06E+00	930.37	6	33	0.23
		142911	biotite2	33.75491254	0.03	0.01	0.00040	0.00000	0.00000	0.00344	0.00033	0.00000	4.95E-15	3.01E+00	919.33	4	33	0.10
		142911	biotite3	33.92783648	0.05	0.01	0.00024	0.08360	0.07181	0.00423	0.00001	0.00000	7.20E-15	3.69E+00	917.98	4	33	0.05
		142911	biotite4	35.99975196	0.10	0.01	0.00027	0.00000	0.00000	0.01489	0.00053	0.00000	1.20E-14	1.22E+01	894.09	5	32	0.18
		142911	biotite6	33.32310685	0.05	0.01	0.00023	0.03653	0.01793	0.00321	0.00025	0.00000	2.16E-14	2.84E+00	911.33	4	32	0.09
		142911	biotite7	35.47355938	0.07	0.01	0.00066	0.00000	0.00000	0.00689	0.00033	0.00000	7.20E-15	5.74E+00	934.62	4	33	0.12
		142911	biotite8	34.38069865	0.06	0.01	0.00002	0.18923	0.02389	0.00577	0.00039	0.00000	4.80E-15	4.96E+00	917.95	5	33	0.13
		142911	biotite9	33.28100033	0.31	0.03	0.00229	1.93175	0.14143	0.00000	–	0.00000	2.40E-15	0.00E+00	963.70	8	35	0.31
		142911	biotite10	34.26385319	0.04	0.01	0.00040	0.00000	0.00000	0.00321	0.00000	0.00000	7.20E-15	2.77E+00	931.98	4	33	0.04
		142911	biotite11	33.64385063	0.28	0.02	0.00040	0.15853	0.00948	0.00786	0.00020	0.00000	4.56E-14	6.91E+00	887.85	7	31	0.27
			Weighted mean												**920.50**	**1**		
			Unweighted mean												**920.92**	**20**		
0.02047	0.000102	142924	muscovite1	32.6754304	0.02	0.01	0.00008	0.00034	0.00075	0.00051	0.00003	0.00000	4.08E-14	4.62E-01	920.62	4	33	0.02
		142924	muscovite2	34.59145261	0.01	0.01	0.00007	0.01445	0.00046	0.00082	0.00004	0.00000	1.68E-14	6.96E-01	960.65	4	34	0.02
		142924	muscovite3	29.94792194	0.02	0.01	0.00012	0.03800	0.00352	0.00066	0.00000	0.00000	1.21E-14	6.49E-01	858.12	3	30	0.02
		142924	muscovite4	36.77928352	0.03	0.01	0.00026	0.00534	0.00524	0.00211	0.00000	0.00000	7.30E-15	1.69E+00	999.38	4	36	0.03
		142924	muscovite5	31.00979253	0.04	0.01	0.00019	0.00000	0.00000	0.00010	0.00010	0.00000	1.44E-14	9.18E-02	886.08	4	31	0.05
		142924	muscovite6	31.70780207	0.02	0.01	0.00009	0.00000	0.00000	0.00077	0.00005	0.00000	9.60E-15	7.19E-01	897.31	4	31	0.02
		142924	muscovite7	34.23228332	0.02	0.01	0.00012	0.00000	0.00000	0.00092	0.00005	0.00000	1.21E-14	7.93E-01	952.18	4	34	0.03
		142924	muscovite8	33.9470131	0.02	0.01	0.00004	0.00081	0.00000	0.00079	0.00002	0.00000	4.08E-14	6.91E-01	946.76	4	34	0.03
		142924	muscovite9	30.1693731	0.02	0.01	0.00009	0.00000	0.00000	0.00029	0.00004	0.00000	1.44E-14	2.82E-01	865.69	3	30	0.02
		142924	muscovite10	29.68608903	0.02	0.01	0.00008	0.00743	0.00000	0.00024	0.00008	0.00000	9.60E-15	2.41E-01	854.92	3	30	0.03
		142924	muscovite11	32.66705953	0.03	0.01	0.00008	0.00000	0.00000	0.00059	0.00003	0.00000	3.12E-14	5.33E-01	919.92	4	32	0.03
		142924	muscovite12	31.91857051	0.04	0.01	0.00019	0.01746	0.00002	0.00095	0.00019	0.00000	7.30E-15	8.79E-01	900.85	4	32	0.07
			Weighted mean												**910.87**	**1**		
			Unweighted mean												**913.54**	**43**		
0.02044	0.000102	142926	biotite1	40.3028209	0.03	0.02	0.00013	0.00000	0.00000	0.01226	0.00015	0.00000	1.22E-14	8.99E+00	1 009.33	4	37	0.05
		142926	biotite2	39.15985151	0.03	0.01	0.00007	0.06675	0.00523	0.01000	0.00007	0.00000	2.88E-14	7.54E+00	999.31	4	36	0.03
		142926	biotite3	38.26252833	0.04	0.02	0.00013	0.00000	0.00000	0.00576	0.00006	0.00000	2.16E-14	4.45E+00	1 006.81	4	37	0.04
		142926	biotite4	39.29513147	0.06	0.02	0.00017	0.00000	0.00000	0.01601	0.00017	0.00000	9.90E-15	1.20E+01	964.16	4	35	0.07
		142926	biotite5	39.55763942	0.03	0.02	0.00016	0.08310	0.00544	0.01038	0.00007	0.00000	9.90E-15	7.75E+00	1 005.33	4	36	0.04
		142926	biotite6	40.81606789	0.02	0.01	0.00009	0.01003	0.00656	0.01031	0.00009	0.00000	1.46E-14	7.46E+00	1 032.14	4	38	0.03
		142926	biotite7	37.34611999	0.06	0.01	0.00031	0.03264	0.02388	0.00533	0.00031	0.00000	1.22E-14	4.22E+00	990.06	4	36	0.11
		142926	biotite8	40.285582	0.07	0.01	0.00070	0.05594	0.03883	0.01124	0.00002	0.00000	5.37E-15	8.25E+00	1 015.29	4	37	0.07
		142926	biotite9	38.30187535	0.02	0.01	0.00008	0.01152	0.00141	0.00800	0.00000	0.00000	1.93E-14	6.17E+00	993.63	4	36	0.01
		142926	biotite10	38.36375446	0.02	0.01	0.00001	0.02439	0.00001	0.00691	0.00009	0.00000	1.44E-14	5.32E+00	1 001.77	4	36	0.03
		142926	biotite11	37.17742928	0.07	0.01	0.00017	0.00000	0.00000	0.00633	0.00015	0.00000	2.66E-14	5.03E+00	980.18	4	35	0.08
		142926	biotite13	37.28099807	0.03	0.01	0.00018	0.00325	0.00319	0.00448	0.00024	0.00000	7.30E-15	3.55E+00	994.01	4	36	0.08
		142926	biotite14	38.34247628	0.05	0.01	0.00009	0.00000	0.00000	0.00579	0.00025	0.00000	1.68E-14	4.46E+00	1 008.30	4	37	0.09
		142926	biotite15	39.62581297	0.03	0.01	0.00012	0.03445	0.00483	0.00951	0.00001	0.00000	1.44E-14	7.10E+00	1 012.16	4	37	0.03
			Weighted mean												**1 001.10**	**1**		
			Unweighted mean												**1 000.89**	**16**		

Appendix 3 (continued)

J value	+/–	Sample #	Type	$^{40}Ar/^{39}Ar$	+/–	$^{38}Ar/^{39}Ar$	+/–	$^{37}Ar/^{39}Ar$	+/–	$^{36}Ar/^{39}Ar$	+/–	$^{39}Ar^*$ (cm^3)	+/–	% atmospheric Ar	Age (Ma)	+/–	$^{40}Ar^*/^{39}Ar$	+/–
0.02037	0.000102	142932	biotite1	34.69961193	0.03	0.01	0.00018	0.00673	0.00476	0.00613	0.00013	0.00000	1.25E-14	5.22E+00	925.08	4	33	0.05
		142932	biotite2	36.35491879	0.05	0.01	0.00018	0.07412	0.00532	0.01068	0.00018	0.00000	1.72E-14	8.68E+00	931.96	4	33	0.07
		142932	biotite3	34.123759	0.21	0.01	0.00028	0.33905	0.10943	0.00617	0.00111	0.00000	5.31E-15	5.35E+00	912.11	9	32	0.39
		142932	biotite4	34.74666206	1.73	0.01	0.00015	0.00000	0.00000	0.00000	–	0.00000	1.68E-14	0.00E+00	965.55	37	35	1.73
		142932	biotite5	33.39391676	0.85	0.01	0.00024	0.00000	0.01093	0.00553	0.00069	0.00000	1.03E-13	4.89E+00	900.12	19	32	0.85
		142932	biotite6	33.27662773	0.98	0.01	0.00053	0.04070	0.00676	0.00688	0.00038	0.00000	2.09E-13	6.11E+00	888.55	21	31	0.93
		142932	biotite7	36.21064486	0.72	0.01	0.00023	0.27414	0.00525	0.00582	0.00148	0.00000	3.12E-14	4.75E+00	960.02	18	34	0.81
		142932	biotite8	33.99198096	0.37	0.01	0.00038	0.00000	0.00000	0.00342	0.00017	0.00000	6.96E-14	2.97E+00	927.19	9	33	0.36
		142932	biotite9	36.36092096	0.20	0.01	0.00063	1.55417	0.00784	0.00524	0.00140	0.00000	9.67E-15	4.25E+00	967.00	10	35	0.46
		142932	biotite10	37.00059488	0.20	0.01	0.00007	0.12092	0.02866	0.00238	0.00040	0.00000	3.12E-14	1.90E+00	998.59	6	36	0.23
		142932	biotite11	33.18199581	0.83	0.01	0.00034	0.01325	0.09105	0.00639	0.00129	0.00000	4.32E-14	5.69E+00	889.67	20	31	0.87
		142932	biotite12	33.77458568	0.06	0.01	0.00002	0.05557	0.03472	0.00242	0.00049	0.00000	7.30E-15	2.12E+00	928.86	5	33	0.15
			Weighted mean												**936.01**	**2**		
			Unweighted mean												**932.89**	**33**		
0.02038	0.000102	142932	muscovite1	31.73334245	0.91	0.01	0.00101	0.00036	0.00026	0.00050	0.00025	0.00000	7.54E-13	4.67E-01	896.55	21	32	0.91
		142932	muscovite2	31.09719283	0.04	0.01	0.00030	0.00000	0.00000	0.00017	0.00030	0.00000	2.16E-14	1.59E-01	884.49	4	31	0.10
		142932	muscovite4	34.91574005	0.25	0.01	0.00024	0.00108	0.00022	0.00096	0.00011	0.00000	2.74E-13	8.10E-01	963.47	7	35	0.25
		142932	muscovite5	31.78110384	0.08	0.01	0.00062	0.00031	0.00218	0.00281	0.00031	0.00000	4.95E-15	2.61E+00	882.33	4	31	0.12
		142932	muscovite6	31.26024388	0.04	0.01	0.00022	0.00099	0.00077	0.00077	0.00011	0.00000	1.21E-14	7.27E-01	884.16	4	31	0.05
		142932	muscovite7	33.48739428	0.05	0.01	0.00016	0.00354	0.00016	0.00040	0.00008	0.00000	2.16E-14	3.55E-01	936.01	4	33	0.06
		142932	muscovite8	30.7757085	0.32	0.01	0.00055	0.00000	0.00000	0.00081	0.00027	0.00000	4.32E-14	7.77E-01	872.94	8	31	0.33
		142932	muscovite9	31.5142836	0.21	0.01	0.00008	0.00067	0.00007	0.00037	0.00007	0.00000	1.01E-13	3.47E-01	892.51	6	31	0.21
		142932	muscovite10	32.86064964	0.89	0.01	0.00004	0.00000	0.00000	0.00000		0.00000	1.68E-14	0.00E+00	924.86	20	33	0.89
		142932	muscovite11	34.48327306	0.11	0.01	0.00004	0.01221	0.00136	0.00136	0.00136	0.00000	7.59E-15	1.16E+00	951.57	10	34	0.42
		142932	muscovite12	30.86907159	0.02	0.01	0.00007	0.00000	0.00000	0.00003	0.00010	0.00000	2.65E-14	3.32E-02	880.23	4	31	0.04
			Weighted mean												**898.38**	**2**		
			Unweighted mean												**906.28**	**30**		
0.02043	0.000102	142933	biotite1	43.013795	0.06	0.02	0.00011	0.00023	0.00000	0.00178	0.00011	0.00000	2.88E-14	1.22E+00	1 127.36	4	42	0.07
		142933	biotite2	41.07088767	0.07	0.01	0.00010	0.00018	0.00026	0.00163	0.00034	0.00000	1.20E-14	1.17E+00	1 089.48	5	41	0.12
		142933	biotite3	36.62165942	0.04	0.01	0.00005	0.00005	0.00015	0.00259	0.00018	0.00000	2.64E-14	2.09E+00	991.54	4	36	0.07
		142933	biotite4	40.88091473	0.29	0.01	0.00030	0.00000	0.00000	0.00314	0.00167	0.00000	2.40E-14	2.27E+00	1 076.65	12	40	0.57
		142933	biotite5	35.72403548	0.11	0.01	0.00025	0.00000	0.00000	0.00340	0.00068	0.00000	1.68E-14	2.81E+00	967.18	6	35	0.23
		142933	biotite6	55.12180667	0.02	0.01	0.00006	0.00000	0.00000	0.00281	0.00006	0.00000	1.46E-14	1.50E+00	1 346.41	5	54	0.03
		142933	biotite7	51.59649898	0.03	0.02	0.00034	0.00000	0.00000	0.00741	0.00034	0.00000	3.39E-15	4.24E+00	1 258.95	5	49	0.10
		142933	biotite8	37.65881575	0.04	0.01	0.00019	0.00000	0.00000	0.00312	0.00007	0.00000	1.44E-14	2.45E+00	1 010.14	4	37	0.04
		142933	biotite9	40.30767572	0.02	0.01	0.00010	0.00000	0.00000	0.00307	0.00010	0.00000	4.80E-15	2.25E+00	1 065.37	4	39	0.04
		142933	biotite10	45.31173025	0.09	0.01	0.00030	0.00000	0.00000	0.00106	0.00030	0.00000	1.21E-14	6.93E-01	1 176.20	5	45	0.13
		142933	biotite11	39.30880476	0.05	0.01	0.00020	0.00014	0.00014	0.00014	0.00014	0.00000	4.95E-15	1.04E-01	1 062.67	4	39	0.07
		142933	biotite12	41.55722587	0.03	0.02	0.00016	0.00006	0.00006	0.00189	0.00000	0.00000	1.44E-14	1.34E+00	1 097.74	4	41	0.03
			Weighted mean												**1 105.81**	**105**		
			Unweighted mean												**1 102.45**	**1**		
0.02042	0.000102	168944	biotite1	48.63470435	0.03	0.01	0.00011	0.02520	0.00318	0.00334	0.00010	0.00000	1.44E-14	2.03E+00	1 225.97	5	48	0.04
		168944	biotite2	49.47646426	0.14	0.01	0.00004	0.18341	0.01638	0.00639	0.00072	0.00000	4.80E-15	3.82E+00	1 224.83	6	48	0.25
		168944	biotite3	50.84387096	0.07	0.01	0.00002	0.03613	0.00273	0.00488	0.00012	0.00000	1.44E-14	2.84E+00	1 258.42	5	49	0.08
		168944	biotite4	47.53756485	0.03	0.01	0.00014	0.00473	0.00346	0.00277	0.00007	0.00000	1.20E-14	1.72E+00	1 208.55	4	47	0.04
		168944	biotite5	48.01060018	0.04	0.01	0.00001	0.00336	0.00330	0.00476	0.00014	0.00000	7.20E-15	2.93E+00	1 206.38	5	47	0.06
		168944	biotite6	47.36208097	0.06	0.01	0.00059	0.00000	0.00000	0.00507	0.00089	0.00000	1.44E-14	3.17E+00	1 192.32	7	46	0.27
		168944	biotite7	53.41442118	1.58	0.01	0.00042	0.00000	0.00000	0.01281	0.00116	0.00000	9.12E-14	7.09E+00	1 262.57	30	50	1.60
		168944	biotite8	50.28993409	0.36	0.01	0.00107	0.00626	0.02215	0.00455	0.00187	0.00000	1.21E-14	2.67E+00	1 250.05	13	49	0.66

Appendix 3 (continued)

J value	*+/–*	*Sample #*	*Type*	$^{40}Ar/^{39}Ar$	*+/–*	$^{38}Ar/^{39}Ar$	*+/–*	$^{37}Ar/^{39}Ar$	*+/–*	$^{36}Ar/^{39}Ar$	*+/–*	$^{39}Ar^{*}$ *(cm³)*	*+/–*	*% atmospheric Ar*	*Age (Ma)*	*+/–*	$^{40}Ar^{*}/^{39}Ar$	*+/–*
		168944	biotite11	49.4447242	0.06	0.01	0.00013	0.05735	0.00504	0.00395	0.00019	0.00000	2.17E-14	2.36E+00	1 237.69	5	48	0.08
		168944	biotite12	47.83508831	0.13	0.01	0.00027	0.00947	0.01314	0.00924	0.00040	0.00000	7.59E-15	5.71E+00	1 177.85	5	45	0.17
		168944	biotite13	49.55172812	0.10	0.01	0.00043	0.00680	0.01493	0.00740	0.00019	0.00000	1.20E-14	4.41E+00	1 220.67	5	47	0.11
			Weighted mean												**1 219.69**	**2**		
			Unweighted mean												**1 224.12**	**26**		
0.02039	0.000102	168944	muscovite1	32.46310545	0.02	0.01	0.00012	0.00000	0.00000	0.00069	0.00000	0.00000	1.92E-14	6.29E-01	911.91	4	32	0.02
		168944	muscovite2	37.71080537	0.03	0.01	0.00016	0.00089	0.00029	0.00131	0.00015	0.00000	1.21E-14	1.02E+00	1 020.96	4	37	0.05
		168944	muscovite3	37.80701425	0.03	0.01	0.00025	0.00136	0.00044	0.00311	0.00000	0.00000	9.67E-15	2.43E+00	1 011.80	4	37	0.03
		168944	muscovite4	31.70773094	0.20	0.01	0.00039	0.00000	0.00000	0.00052	0.00104	0.00000	1.78E-14	4.83E-01	896.22	9	32	0.37
		168944	muscovite5	32.08107011	0.10	0.01	0.00018	0.00000	0.00000	0.00000	0.00000	0.00000	1.78E-14	0.00E+00	907.96	5	32	0.18
		168944	muscovite6	31.70634484	0.22	0.01	0.00080	0.00000	0.00000	0.00000	0.00000	0.00000	7.68E-15	0.00E+00	899.61	6	32	0.22
		168944	muscovite7	32.38358835	0.10	0.01	0.00024	0.00000	0.00000	0.00109	0.00027	0.00000	1.13E-14	9.93E-01	907.54	5	32	0.13
		168944	muscovite8	32.96558289	0.38	0.01	0.00085	0.00000	0.00000	0.00169	0.00084	0.00000	1.07E-14	1.51E+00	916.51	11	32	0.45
		168944	muscovite10	33.70864209	0.03	0.01	0.00018	0.00000	0.00000	0.00095	0.00016	0.00000	1.22E-14	8.34E-01	937.66	4	33	0.06
		168944	muscovite11	32.23731787	0.07	0.01	0.00002	0.00000	0.00000	0.00124	0.00018	0.00000	1.22E-14	1.14E+00	903.28	4	32	0.08
			Weighted mean												**941.07**	**1**		
			Unweighted mean												**931.34**	**44**		
0.029	0.000101	168946	biotite1	35.40781191	0.09	0.01	0.00027	0.00000	0.00000	0.01013	0.00029	0.00000	2.17E-14	8.45E+00	911.84	4	32	0.12
		168946	biotite2	33.27989134	0.05	0.02	0.00002	0.00000	0.00000	0.00821	0.00012	0.00000	1.22E-14	7.29E+00	877.05	4	31	0.06
		168946	biotite3	33.70811799	0.05	0.02	0.00037	0.07077	0.06948	0.00915	0.00037	0.00000	4.80E-15	8.02E+00	880.46	4	31	0.12
		168946	biotite4	37.54421011	0.05	0.02	0.00020	0.05806	0.03800	0.01381	0.00020	0.00000	7.20E-15	1.09E+01	934.83	4	33	0.07
		168946	biotite5	32.19580686	0.04	0.01	0.00022	0.02623	0.00515	0.00379	0.00033	0.00000	1.22E-14	3.48E+00	882.01	4	31	0.10
		168946	biotite6	32.64224804	0.04	0.01	0.00044	0.01064	0.02335	0.00330	0.00066	0.00000	5.37E-15	2.99E+00	895.27	6	32	0.20
		168946	biotite7	34.16872457	0.05	0.01	0.00002	0.03073	0.03017	0.00296	0.00042	0.00000	7.59E-15	2.56E+00	931.17	5	33	0.13
		168946	biotite8	33.9146324	0.16	0.01	0.00007	0.00000	0.00000	0.00305	0.00107	0.00000	1.46E-14	2.66E+00	925.01	9	33	0.35
			Weighted mean												**901.84**	**2**		
			Unweighted mean												**904.71**	**22**		

OCCHIPINTI

Neoproterozoic reworking in the Paleoproterozoic Capricorn Orogen: evidence from $^{40}Ar/^{39}Ar$ ages

RECORD 2007/10

This Record is published in digital format (PDF) and is available online at: www.doir.wa.gov.au/GSWA/publications. Laser-printed copies can be ordered from the Information Centre for the cost of printing and binding.

Further details of geological publications and maps produced by the Geological Survey of Western Australia can be obtained by contacting:

Information Centre
Department of Industry and Resources
100 Plain Street
East Perth WA 6004
Phone: (08) 9222 3459 Fax: (08) 9222 3444

www.doir.wa.gov.au/GSWA/publications